Assimilation of High Frequency Radar Data into a Shelf Sea Circulation Model

Dissertation

Zur Erlangung des Doktorgrades
der Naturwissenschaften
im Department Geowissenschaften
der Universität Hamburg

vorgelegt von

Jiangling Xu

aus

Yantai, China

Hamburg

2010

Als Dissertation angenommen vom Department Geowissenschaften der Universität Hamburg

Auf Grund der Gutachten von Dr. Thomas Pohlmann
und Prof. Dr. Jürgen Sündermann

Hamburg, den 31.05.2010

Prof. Dr. Jürgen Oßenbrügge
Leiter des Departments für Geowissenschaften

Abstract

With the development of High-Frequency (HF) radar application in mapping coastal currents, more and more oceanic data assimilation efforts have been focused on coastal regions. The assimilation methods have been developed in different ways, including inverse method, optimal interpolation, variational method and Kalman filter technique. Meanwhile, the assimilation objects also have been taken into account from univariable to multivariable. Hence, it is getting increasingly important to find a feasible assimilation method to combine radar current data and sophisticate ocean models.

In this thesis, the main work has been restricted to develop a feasible and operational assimilation method that can be implemented in a shelf ocean model with realistic topography and boundary conditions. The assimilation method used here is a combination of the Ensemble Kalman Filter (EnKF) and the Canadian Quick Covariance (CQC) method.

As we know, the main objective of all the assimilation methods is to combine the model results and observations with a reasonable treatment of model errors. The EnKF method uses an ensemble of shortrange forecast model runs to describe the model errors. However, as we proved in the thesis, such a method can not realize real-time assimilations using high frequency observations. On the other hand, the generation of this ensemble is arduous, since this ensemble members should represent all the possibilities of model results using the assumption that the estimation of background errors is correct. A quick and easy way to get the background error covariances is the CQC method, which involves obtaining the model states from one single forecast at a fixed interval, calculating the covariances by using differences between successive output fields thereafter. Such covariances are assumed as a proxy for the model errors. Thus, we use the CQC method to substitute the background error covariances calculated from the ensemble of forecast model runs. The assumption behind this implementation is that forecast errors can be resembled by forecast tendencies.

The time interval in this study is chosen according to the character of observed data, which typically is 20 minutes. As the tidal forcing is included in the model, this time interval is reasonable for resolving the tidal phase error. Our numerical experiments show that this newly developed method is appropriate for real-time assimilation of HF observations for shelf ocean model. With implementation of this assimilation scheme the model also provides more realistic results for shelf

currents, as well as for temperature and salinity distributions.

With the traditional EnKF method, the posterior variance keeps decreasing with time, consequently a divergence will happen and the analysis will ignore the observations at the end. Compared to the traditional EnKF method, the newly developed method proves that the ensemble is really flow-dependent. No matter whether with a linear model or a complex nonlinear model, the newly developed method is consistent in its performance. To summarize, we developed a real-time and effective assimilating scheme, which is suitable for operational ocean modeling using HAMSOM for instance, as a fully non-linear model system including tide and baroclinic effect as well as the dynamics at shelf slope.

Acknowledgements

I would like to thank Dr. Thomas Pohlmann for his invitation and supervision, criticisms and suggestions. And his concerns make me have a feeling of home in Germany.

I would like to thank Prof. Xueen Chen for his generous help and guidance, encouragement and helpful comments. He also carefully corrects the text of the dissertation.

I would like to thank Dr. Klaus-Werner Gurgel for supplying the data.

Thanks should be given to all the colleagues of the Institute of Oceanography Hamburg for support, especially to Dr. Bernhard Mayer. He helped me a lot in the model modifications and in daily life.

Last but not least, I would like to thank Dr. Jan Su and Huaming Yu for passing on me at several times and the support during stressful times.

Thanks should be given to the project which was funded by Germany BMBF 0360359*A* 'WERAWARN'.

Finally, I am very grateful for my family and friends who have given me constant support.

Jiangling Xu

Hamburg, 03.2010

Contents

Chapter 1

Introduction

1.1 Assimilation with Radar Data

Since the HF radar was developed and its technique of mapping coastal currents (Barrick, 1978; Barrick et al., 1977) has matured to a reliable degree, the coastal surface current can be observed more reliably with a high temporal and spatial resolution, compared to in-situ data even satellite altimetry data. Due to this reason more and more assimilation efforts were recently made in coastal regions as follows.

Lewis et al. (1998) treated the Doppler radar surface current data as an additional layer of water overlying the ocean surface, and used the differences between the observed values and the model velocity to correct the wind forcing data for the model. By this approach the main pattern of the Doppler radar current was introduced into the model surface current.

Scott et al. (2000) used an idealized, linear model with a variational inverse assimilation scheme to assess the feasibility of assimilation of surface current measurements. Kurapov et al. (2002) compared the Generalized Inverse Method (GIM), Kalman Filter (KF) and Optimal Interpolation (OI) with an idealized three-dimensional time-dependent coastal baroclinic model. They found that the GIM yielded a smaller posterior error variance than the KF or OI method because the information of the past flow is introduced into the data.

With respect to realistic simulations, Breivik and Saetra (2001) performed the

assimilation of HF radar current data into a realistic coastal model. A " quasi-ensemble " assimilation method was used, the ensemble of model states are sampled from a reference run to calculate the background covariances and these covariances remain constant throughout the assimilation period. They showed that a significant improvement on the model forecast by assimilation of HF radar current data decreased quickly in six hours.

Oke et al. (2002) used a sequential optimal interpolation scheme to assimilate HF radar data into a primitive equation coastal ocean model. An ensemble of model states sampled from 18 different summers was used to compute the forecast error covariances, and a time-averaging procedure was used to introduce the corrections gradually to the model state. They found that the assimilation system can be most effective when the factors of the estimated forecast and observation error covariances were 80% and 20%, respectively.

Paduan and Shulman (2004) assimilated HF radar data in the Monterey Bay area. By considering an Ekman-layer projection of the corrections introduced by assimilation, the spatial and temporal differences between modeled and observed data decreased significantly. However, additional Ekman pumping was generated in such projection.

Recently, Barth et al. (2007) carried out an ensemble simulation of a nested model under different wind forcing conditions to estimate the error covariance of the model states vector and the covariance between ocean currents and winds. In this study tides were removed from the observed surface currents, by averaging the data over two days. The results show an improvement when an additional filter was used to reduce the surface-gravity waves.

All these studies indicate that the analysis in the assimilation system is based on estimates of the error statistics for both, the model forecast and the measurements (Talagrand, 1997). One of the most advanced data assimilation techniques is Ensemble Kalman Filter (EnKF), which uses an ensemble of short-term forecast model states to estimate the forecast errors. In addition, the way to get these ensembles is varying, like taking an ensemble of models representing different summers (Oke et al., 2002) , or an ensemble of models under different wind forcing conditions (Keppenne, 2000; Barth et al., 2007), or adding a random perturbations to the initial state to generate an ensemble (Evensen, 2003, 2004; Kurapov et al., 2002; Houtekamer and Mitchell, 1998; Anderson, 2001; Lermusiaux, 1999; Hamill et al., 2001; Mitchell et al., 2002; Mitchell and Houtekamer, 2000; Heemink et al., 2001; Hansen and Smith, 2001), etc.

1.2 Motivation

In order to introduce the HF radar current data into a hydrodynamical shelf model to improve the model results and then give a better forecast, an assimilation method needs be developed and evaluated. According to former studies, three main difficulties have to be overcome to achieve this ultimate target.

- First, proper and realistic estimates of model errors should be provided, which also should be flow-dependent.
- Second, a sequential assimilation method used in a nonlinear model has to be developed and evaluated.
- Last, the assimilation method should be suitable for high frequency assimilation and can give real-time forecast.

In our study, we also used an ensemble of model states to represent the model errors, however, the way to build up the ensemble is referred to the CQC method (Polavarapu et al., 2005; D.R.Jackson, 2008), which involves the collection of model states from one single forecast at fixed interval, followed by the calculation of differences between successive output fields as proxies for model error. This operation, to a great extent, makes the implementation of the traditional EnKF method much more quick and saves CPU time. The assumption behind this implementation is as the same as in the CQC method, which is that forecast errors can be resembled by forecast tendencies.
Since the radar data we used is sampled with high frequency, the expectation is to develop a real-time assimilation method with the lowest computing cost of application. Moreover, the velocity has a strong correlation with the temperature and salinity in a baroclinic model. Multivariable analysis therefore should be taken into account in the assimilation system.
Hence, the main objective of the current study is to use this, as we call it, Quick Ensemble Kalman Filter (QEnKF) method to assimilate HF-radar current data into a shelf ocean model.

1.3 Outline

This thesis contains 7 chapters. After this short introduction, the second chapter depicts the development of assimilation methods, especially the Ensemble Kalman Filter (EnKF) method and Canadian Quick Covariance (CQC) method, the introduction of our real-time and high-frequency assimilation method (QEnKF).
In the third chapter, a linear model is used to illustrate the implementation and factors of new assimilation method. The comparison of the new method and other assimilation methods is also given here. In order to evaluate the application of this method into a realistic ocean model, the Hamburg Shelf Ocean Model (HAMSOM) is adopted, which is briefly described in the fourth chapter. A hydrodynamic simulation is performed with HAMSOM in the Norwegian Coast. Chapter five introduces the high-frequency radar data, and shows the comparison between the observed currents by radar and simulated currents by HAMSOM.
In the sixth chapter, the real-time high frequency assimilation with new method is implemented into a nonlinear shelf model. A few assimilation experiments are performed to diagnose the assimilation parameters and to overcome difficulties of assimilation, including, how to avoid filter divergence, how to maintain prior estimation of error covariance, etc. The last chapter summarizes the findings of this thesis and deals with unanswered questions.

Chapter 2

Methodology

2.1 Development of Assimilation Method

Recently, since the amount of observational data increases rapidly and the ability of computer model simulation improves, assimilation becomes more and more important in oceanography. Briefly, the definition and purpose of assimilation are importing the information content of observations into a numerical model and providing a correct initial condition for model prediction. The process of data assimilation is usually called "analysis". Considering the concept of assimilation, it has a long history, and can be retrospected to subjective analysis and objective analysis. The objective analysis has been developed through the following steps.
First, the polynomial interpolation, which is referred by Panofsky (1949) in 1949, used a polynomial function to fit all the observations to analytical points in a small piece of area. The coefficients of this function were determined by minimizing the mean squared differences between the polynomial values and observations, which are also referred as the weights in an analysis equation, and control the effect of the objective analysis.
Second, successive correction, which does not aim to analyze observations directly, but subtracts background values from every corresponding observation to get the observation increments, then converts those to analyzed increments, eventually, adds the latter back to the background values. Based on this method, Cressman (1959) used the iteration solution to get the successive corrections. The successive correction introduces the knowledge of so called "background", by which the "inconsistency" problem in polynomial interpolation is solved. The inconsistency

problem usually happens in the area with sparse observations.
Third, optimal interpolation (OI) (Eliassen, 1954; Gandin and Hardin, 1965; Schlatter, 1975; Lorenc, 1981), is a linear interpolation method using the least-squares technique. This method presents a larger improvement compared to the former method by reconsidering the weights, or the ratio and the correlation of the background error and observation error.
Then, with the event of irregular observations, like as satellites, people started to introduce this kind of data into objective analysis and the word "assimilation " was widely used to describe this process. However, with the development of the theory and technology, assimilation has already been developed far beyond the objective analysis. Daley (1993) pointed out that one whole assimilation system should include quality control, objective analysis, initialization and short-range forecast of the background field for the next assimilation.
As Talagrand (1997) said, the existing assimilation algorithms can be described as either sequential or variational.
In the sequential assimilation methods, the model is integrated in time until the observations are available, the state predicted by the model is used as a background which is updated or corrected by the observations. The output of the analysis process is called analyzed state, which is also the initial state for the next assimilation cycle. Then the model restarts to be integrated again from the analyzed state, and the process is repeated until all the available observations have been used. The feature of the sequential assimilation is that each individual observation is only used once and the state can be updated successively along time. But its drawback is, each individual observation only influences the estimated state of the flow at later times, not at previous times.
On the other hand, variational methods aim at globally adjusting a model state to all the observations available in the assimilation period, that means all of the estimated states over the whole assimilation period are influenced by all the observations. In usage of variational assimilation methods (Andersson et al., 1994; Lorenc, 1986; Parrish and Derber, 1992; Thompson, 1969; Thépaut et al., 1993; Courtier et al., 1994; Fisher and Courtier, 1995; Stammer et al., 2002, 2004; Schröter et al., 1993; KOHL and WILLEBRAND, 2002; Köhl and Stammer, 2004), a scalar function is firstly defined, for any model solution over the assimilation interval, to measure the distance or misfit between the solution and the available observations. This objective function (or cost function) will typically be a sum of differences between the observations and the corresponding model values. Then by minimizing

this function, the best estimation of model state can be achieved. However, the cost function of a completed forecast model is difficult to define, or even not exists sometimes.

To summarize, the application of data assimilation that we concerned with is a state estimation. In this case, one considers the problem of estimating the model state over a time period by simultaneously extracting a maximum amount of information from both observations and the dynamical model. Indeed, data assimilation methods have been developed previously for state estimation, both in physical oceanography and meteorology. For use in operational forecasting and monitoring systems, the most common methods are OI, three-dimensional variational analysis (3D-Var), four-dimensional analysis (4D-Var) and Kalman filter (KF) method. The number of publications and applications of data assimilation in physical oceanography is huge. Here we only focus on the KF method (Kalman (1960); Kalman and Bucy (1961) for the original works).

2.2 Development of Kalman Filter

From the earlier of $80s$, state estimation theory was used in the application of data assimilation, the method of which is Kalman Filter (Kalman, 1960). KF is employed to give an optimal estimation of the state of a process, which is a typical sequential assimilation method. Different from the variational method which seeks the optimal solution over the whole assimilation period, the sequential method gives the optimal solution at each observation time step. Moreover, the KF method also gives the distribution of the error covariance of model states after each analysis, which is referred to as the posterior error covariance, but that can not be reformed with variational methods. Hence, according to the description of sequential assimilation methods, the implementation of the KF algorithm can be divided into two parts, one of it is a forecast system, the other is an analysis system.

In the first part, a time-discrete controlled process that is governed by the linear

stochastic difference equation, is included,

$$\varphi_n^f = M\varphi_{n-1}^a, \tag{2.1}$$
$$\varphi_n^t = M\varphi_{n-1}^t + w_n, \tag{2.2}$$
$$P_n^f = MP_{n-1}^a M^T + Q_n. \tag{2.3}$$

Here, φ is the model state vector and P is its error covariance. The superscripts, f, a, t, represent forecast, analyzed, and true state, respectively. The subscript n represents time step. M is a linear model operator to integrate the model state from the previous time step $n-1$ to the current time step n. While in this operation, due to the deficiency of numerical discretization, differential solutions and boundary conditions, numerical errors will be generated, and w is the process error or model error. The covariance of w is written as Q. T denotes the transpose. When a measurement d is available, it can be related to the true state as

$$d_n = H_n\varphi_n^t + \varepsilon_n, \tag{2.4}$$

by a measurement operator H, and with the measurement error ε.
Now, the second part of KF algorithm is implemented through following equations:

$$\varphi_n^a = \varphi_n^f + K_n(d_n - H_n\varphi^f), \tag{2.5}$$
$$K_n = P_n^f H_n^T (H_n P_n^f H_n^T + R_n)^{-1}, \tag{2.6}$$
$$P_n^a = (I - K_n H_n)P_n^f. \tag{2.7}$$

The difference $(d_n - H_n\varphi^f)$ in equation (2.5) is called the measurement innovation, or the residual (Evensen, 2003; Dee, 2005). The residual reflects the discrepancy between the predicted measurement $H_n\varphi^f$ and the actual measurement d_n.
Obviously, the forecast state is corrected by extrapolating this residual to all state variables. The extrapolation from the data to the full state space is accomplished by means of a gain matrix, which guarantees the analysis state has minimum error variance conditioned on all past data. K is such a Kalman gain matrix. It is a function of the model state error covariance matrix P^f and the measurement error covariance matrix R. P^a, the posterior error covariance of the analyzed model state is reduced with respect to the error covariance of the forecasted state as equation (2.7) .
As described above, the KF technique addresses the general problems of estimating the state of a time-discrete controlled process that is governed by a linear stochastic

differential equation, that means both M and H are linear. In this case, the analyzed state estimation is optimal. When the process to be estimated and (or) the measurement operator to the process is nonlinear, the model operator (m) is a function of model state, as well as the observation operator (h).

$$m = m(\varphi), \tag{2.8}$$

$$h = h(\varphi, d). \tag{2.9}$$

We may extend the usage of Kalman filtering through a linearization procedure for the above nonlinear operators. The resulting filter is referred to as the extended Kalman filter (EKF,Welch and Bishop (1995)).
To set the stage for a development of the EKF, we rewrite equation (2.1) and (2.4) as

$$\varphi_n^f = m(\varphi_{n-1}^a) + w_n, \tag{2.10}$$

$$d_n = h(\varphi_n^t) + \varepsilon_n, \tag{2.11}$$

where, as before, w_n and ε_n are independent zero-mean white Gaussian noise processes with covariance matrices Q and R, respectively. Here, however, the functional m denotes a nonlinear transition matrix function that is possibly time-variant. Likewise, the functional h denotes a nonlinear measurement matrix that may be time-variant, too.
By linearizing equation (2.10) around φ_{n-1}^a,

$$\varphi_n^f \approx m(\varphi_{n-1}^a) + M[\varphi_{n-1}^f - \varphi_{n-1}^a] + w_n, \tag{2.12}$$

where M denotes the gradient, or tangent linear operator (Jacobian) of m evaluated at φ_{n-1}^a, the forecast error covariance matrix P_n^f can be seen to be approximately the same as in equation (2.3). Meanwhile, the equations in the analysis part of KF algorithm can also be used, if the gradient of h is given as H.
The basic idea of the EKF is to linearize the state-space model state and its covariance matrix at each time instant around the most recent state estimate. The easiest thing to do the linearization is expanding $M(\varphi)$ in a Taylor series,

$$M(\varphi) = M(\varphi^f) + (\varphi - \varphi^f)M'(\varphi^f) + (1/2)(\varphi - \varphi^f)^2 M''(\varphi^f) + ... \tag{2.13}$$

here, φ is an expected value of φ^f.

Usually, only the first-order moment is kept. Hence, in the sense of this point, the estimate given by EKF is not optimal any more, but suboptimal. For a weakly nonlinear system, the EKF can give reasonable results, however, for strongly nonlinear systems, the second-order or more higher-order moments should not be ignored, consequently, a "closure" problem has to be addressed. The problem consequently affects the estimation given by the EKF. A similar problem arises with the adjoint method used in variational methods, in which a tangent linear approximation constrains the length of the assimilation time interval which is used (Miller et al., 1994).

Simply, the process of the development of the KF method can be distinguished between the methods traditionally implemented for linear model dynamics and nonlinear model dynamics. Since Talagrand and Courtier (1987) first properly introduced the KF method to oceanography and meteorology, the application of the KF technique to work with nonlinear model dynamics has met with some problems. To address those problems, the Extended Kalman Filter (EKF) was introduced by applying a linearization for the error covariance evolution, which may introduce unstabilities in some cases (Evensen, 1992).

More recently, there has been the development of significant assimilation formulations and techniques which have been specifically tailored towards nonlinear dynamical models. The Ensemble Kalman Filter is one such method by using the idea of "ensemble forecasts" (Toth and Kalnay, 1993, 1997; Molteni et al., 1996) and used in our study. It has been chosen usually based on its ability to predict error statistics for strongly nonlinear systems (Evensen, 1994, 1997b), and for its simplicity and numerical efficiency.

The EnKF method was formulated with nonlinear dynamics in mind and the emphasis was focused on deriving a method which could handle the error covariance evolution in nonlinear models (Evensen, 1994). This method has been used successfully with a number of different dynamical models, from the simple but highly nonlinear and chaotic Lorenz equations (Evensen, 1997a), to ocean circulation models (Evensen and van Leeuwen, 1995; Evensen, 1997b). In additional, the EnKF method has been used in both meteorology and oceanography, like as Anderson and Anderson (1999); Miller et al. (1999), etc.

2.3 Ensemble Kalman Filter

As discussed above, a linearized and approximate equation is used for the prediction of error statistics in the EKF method. Hence, for strongly nonlinear dynamics, the linearization in the EKF method will lead to serious problems due to the lack of a higher order closure scheme. In addition, the model is only an approximation of the real physical process, the model error Q is hard to determine. From those equations, the storage and computation of the error covariance matrix is also a major problem. For example, if the size of the model state vector is n, the size of the error covariance matrix is n^2 and $2n$ model integrations are requires to step it forward in time. Due to the upper problems, alternative methodologies have been sought to address the Q and P^f in Kalman Filter, one of which is the Ensemble Kalman Filter (EnKF).

The EnKF was proposed by Evensen (1994) based on stochastic forecast theory, in which, the forecast model error covariance P^f is calculated according to the theory of Monte Carlo approximation (Leith, 1974). Then the theoretical formulation and practical implementation were summarized in Evensen (2004). The forecast model state is treated as one of the stochastic forecasts, hence, an ensemble of such forecasts (assumed number of N) can represent the probability density function of the so-called state space, like:

$$\phi(\psi) = \frac{dN}{N}. \tag{2.14}$$

The mean of the ensemble model representations can be considered as the true state. Then the error covariance matrices for the forecasted (φ^f) and the analyzed (φ^a) estimate, P^f and P^a, are in the Kalman filter defined in terms of the true state (φ^t) as

$$P^f = \overline{(\varphi^f - \varphi^t)(\varphi^f - \varphi^t)^T}, \tag{2.15}$$

$$P^a = \overline{(\varphi^a - \varphi^t)(\varphi^a - \varphi^t)^T}, \tag{2.16}$$

where the overbar denotes an expectation value. With this approximation in the EnKF, it is more convenient to write equation (2.17,2.18) as:

$$P^f \cong P_e^f = \overline{(\varphi^f - \overline{\varphi^f})(\varphi^f - \overline{\varphi^f})^T}, \tag{2.17}$$

$$P^a \cong P_e^a = \overline{(\varphi^a - \overline{\varphi^a})(\varphi^a - \overline{\varphi^a})^T}, \tag{2.18}$$

where the overbar denotes an average over an ensemble. For simplicity, the time subscript is omitted.

Here, an interpretation is used where the ensemble mean is the best estimate and the spreading of the ensemble around the mean is a natural definition of the error of the ensemble mean. Thus, instead of storing a full covariance matrix, the same error statistics can be represented using an approximate ensemble of model states. The equation (2.3,2.7) are not necessary anymore. No "closure" is required neither, which makes the EnKF feasible.

Till now, with the new definitions of ensemble covariances (P^f,P^a) and the equation (2.5) in KF analysis scheme, the algorithm of EnKF can be built up. However, in the practice, Burgers et al. (1998) pointed out that the observations must be treated as random variables to make the continuous analysis consistent. Hence, an ensemble of observations is defined as

$$d_j = d + \varepsilon_j, \tag{2.19}$$

where j counts from 1 to the number of model state ensemble size N. Now, the gain matrix and analysis equation (2.5) in KF algorithm can be rewritten as

$$K = P_e^f H^T (H P_e^f H^T + R)^{-1}, \tag{2.20}$$

$$\varphi_j^a = \varphi_j^f + P_e^f H^T (H P_e^f H^T + R)^{-1} (d_j - H\varphi_j^f). \tag{2.21}$$

Note, j in this equation is not the index of time anymore, it is the index of ensemble members.

In the end, equations (2.17-2.21) describe the traditional EnKF algorithm.

2.3.1 Benefit of Ensemble Kalman Filter

Comparing to other assimilation methods, the EnKF has some advantages as follows.

- Using the ideal of "ensemble" to evaluate the error covariance and propagate of the background.

  In Kalman Filter, since the error covariance matrix should be propagated after every analytic cycle, and that is usually as big as $10^7 \times 10^7$, which means the propagation of the error covariance costs a lot of CPU time, and

till now it is hard to implement in practice. One method to solve that is assuming that the error covariance of background is homogeneous, and constant in time. But with such an assumption, on one hand, the weight in assimilation scheme is not updated. On the other hand, when the observation is discontinuous, especially in some meso-scale or small-scale areas, the nonhomogeneous and anisotrophy of the error will be strong, hence, the assumption of homogenous and isotrophy behind of the KF method is not adequate.

On the contrary, the EnKF method employs an ensemble of forecast model runs to propagate the model errors. By calculating the differences between these members, the error covariance can be achieved. Moreover, the error covariance is flow-dependent along the model propagation and can be anisotropic.

- The problems of applying the KF method in a strongly nonlinear dynamic system are solved.

  Since statistical noise is assumed to dominate the errors in the EnKF, a closure problem or unbounded growth of error variance, as has been found with assimilation methods relying on the use of a tangent linear model, is avoided. In another word, the EnKF method uses an ensemble of model runs to integrate the model equations forward in time. It can be shown that such ensemble integration is identical to a Markov Chain Monte Carlo (MCMC) method for solving the Fokker Planck equation for the evolution in time of the probability density of the model state (Keppenne, 2000).

- Previously, it has been shown that the EnKF method captures the nonlinear error evolution in time and is capable of both importing in the observations and providing realistic error estimates for the estimated state.

- The ensemble is integrated forward in time until measurements are available. At these points, an analysis scheme is used to update or correct the model state in a statistically consistent way. The updated state can be considered as the model forecast plus a number of influence functions, one for each of the measurements. These are multivariate statistical functions computed from the ensemble statistics, i.e. the cross correlations between the different variables in the model are included. Thus, the change in one of the model variable will influence the other variables.

- Compared to variational methods, no adjoint-matrix is need in the EnKF. In fact, not only variational methods need an adjoint-matrix to solve the target function in the analysis system, but also the KF method needs an adjoint-matrix to solve the forecast of error covariance in a nonlinear system. However, with the EnKF method, the propagation of forecast error covariances is not necessary any more, the adjoint-matrix is hence avoided.

- Fundamentally statistical and physical computationally parallel. Since ensemble members are independent from each other, they can be propagated into different computer nodes.

2.3.2 Disadvantage of Ensemble Kalman Filter

The EnKF method inherits the advantage of the KF method, and overcomes some flaws and limitation of the latter. However, every method has its own disadvantage, the limited ensemble size in the EnKF method is its utmost problem: the sample size N is inevitably several orders of magnitude smaller than the size of the covariance matrix. This will generate two problems: one is the "rank problem" of the background error covariance matrix (Houtekamer and Mitchell, 1998), which is caused by ill-conditioning, and another is divergence in continuous updated cycles.

- Rank problem
  This problem happens in the calculation of the inverse of $(R_n + H_n P_n^f H_n^T)$. If the measurement dimension is m, then the size of $(R_n + H_n P_n^f H_n^T)$ is $m \times m$. Usually, the ensemble size N is far smaller than m, that means $(R_n + H_n P_n^f H_n^T)$ is not a full rank matrix, or singular matrix. Singular matrices do not have an inverse. When N is comparable with m, the inverse of a singular matrix is approximately calculated by eigendecomposition. But when N and m are far from each other, there is no reasonable inverse.
  Evensen and van Leeuwen (1995) employed an eigenvalue decomposition of the sum of the represented matrix and the observation error covariance matrix, and set small eigenvalues to zero to avoid the rank problem. The consequence of this approach is that the analysis increments are restricted to the state space spanned by the ensemble members. This solution is acceptable only if the ensemble members can represent the full state space.

- Divergence of filter
  Divergence happens when the analyzed state gets closer and closer to the forecast state, then the analyzed error covariance gets smaller and smaller, and eventually, the effect of measurement will be ignored. Besides, due to the finite ensemble size, the correlation of the forecast state and measurement is underestimated or overestimated, that makes measurements sometimes far from analyzed state and give unrealistic large influence. Eventually, a divergence will also be generated.

- Imbalance problem
  In practical implementation of EnKF, in order to reduce the size of matrix $(R_n + H_n P_n^f H_n^T)$, only observations near the analytical points are used, that generates spurious dynamical effects. Even the "Schur product" (Mitchell and Houtekamer, 2000) still causes slight imbalance.

- Inbreeding problem
  This problem was pointed out by Houtekamer and Mitchell (1998). They claim that the error variance is underestimated due to the effect that the ensemble of forecast model states is updated with a gain matrix calculated from that same ensemble members.

In summary, van Leeuwen (1999) gave a theoretical justification of the EnKF and pointed out that small ensemble sizes lead to systematically underestimated error variances. That is not only because of the reason claimed by Houtekamer and Mitchell (1998), but also due to effects of limited ensembles in the gain itself, since the gain is nonlinear in the prior covariance. Hence, enough ensemble members are the precondition to obtain reliable convergent error variances.

2.3.3 Propagation of Ensemble Kalman Filter

As we described above, the primary problem of the traditional EnKF method is that the limited sample sizes of practical ensembles are far too small to give meaningful statistics about the complete distribution of the model state conditional on the available observations (van Leeuwen, 1999). This has led to a variety of clever heuristic methods that try to overcome this problem.
Evensen and van Leeuwen (1995) used an eigenvalue decomposition to solve the system and only the significant eigenvalues are used, that can resolve the problem

with poor conditioning caused by correlated measurements, as well as the singular matrix introduced when a larger number of measurements than ensemble member is used.

Houtekamer and Mitchell (1998) pointed out that the approach of using the forecast-error covariances computed from an ensemble of short-range forecasts to calculate weights for the assimilation of data using this same ensemble as background fields, gave rise to an inbreeding problem, and used a "double" EnKF (DEnKF) to address this problem, whereby ensemble members are kept in two separate batches, and the covariances from one batch are updated used the gain matrix calculated from another batch. However, van Leeuwen (1999) pointed out that the DEnKF has the similar, but smaller, "inbreeding" problem which is caused by using the gain calculated from the ensemble to update the same ensemble.

Another method for dealing with this problem is multiplying the prior covariance matrix by a constant factor (Anderson, 2001; Hamill et al., 2001). The expectation of this application of covariance inflation is to maintain the balances in phase space, as well as to increase uncertainty in the state estimate.

Anderson (2001) gave an ensemble adjustment Kalman filter for data assimilation. This method is similar to the traditional EnKF method, but it uses a joint state-observation space filter for updating the ensemble when observations become available. In his work, the ensemble adjustment Kalman filter performs significantly better than the traditional EnKF method, apparently because noise introduced into the assimilated ensemble through perturbed observations in the traditional filter limits its relative performance, since the EnKF method introduces noise by forming a random sample of the observational error distribution and this noise has an adverse impact on the quality of assimilation.

In the traditional EnKF method, the state members are updated independently from all others. If two members that are closely related in the prior distribution are impacted by very different subsets of observations, they may end up being too weakly related. One solution is used by letting every state member be impacted by all subsets of observations. However, since some of these observations will be highly correlated with the state variable by chance, an erroneous impact will be generated on the updated ensemble (Hamill et al., 2001). Houtekamer and Mitchell (2001) and Hamill et al. (2001) have filtered the covariance estimates by using a "Schur product" (Paulsen et al., 1989), whereby the ensemble-based covariances are multiplied with a distance-dependent correlation function that decreases

monotonically from 1.0 at the observation location to 0.0 at some prespecified radial distance. But this operation will introduce some slight spurious imbalance.
Hamill and Snyder (2000) used a hybrid of EnKF and 3DVAR, whereby covariances are modeled as a combination of covariances from the ensemble and from a stationary model. The method was used in a quasi-geostrophic model under perfect-model assumptions, and shows that analysis performs better when ensemble size is larger.
All these efforts were done for realistic implementation of the Ensemble Kalman filter with limited ensemble members. However, applications doing a real time high-frequency assimilation are rare. The problem for realistic applications is that the preparation of ensemble model states costs too much computer time.
As we mentioned before, to make a real time assimilation, Breivik and Saetra (2001) developed the "quasi-ensemble" assimilation method, which is referred as QuasiE by us. In that method, the model states were collected from a representative forecast run, and were used to determine a constant error covariance. However, in order to improve the QuasiE method and keep the covariance of the model states flow-dependent, we collect the model states from the actual assimilation run, and use the differences between the model states of the same run to describe the model errors, not the relationship of model states of different runs. This collection is a close analogy to Canadian Quick Covariance (CQC) method (Polavarapu et al., 2005; D.R.Jackson, 2008).

2.4 Canadian Quick Covariance method

The Canadian Quick Covariance (CQC) method was proposed by Polavarapu et al. (2005) as a pragmatic approach for estimating the background model errors. It was also used by D.R.Jackson (2008) in the Met Office data assimilation, and shown a better performance than National Meteorological Center method. The CQC method involves performing a single forecast for a month, and obtaining output fields from the run at 6-hour intervals. Covariances are subsequently calculated by using the 6-hour difference between successive output fields as proxy for model errors. The major advantage of this technique is that it is relatively simple and fast, since only one forecast is run. This is also the reason that the method is referred to as Canadian Quick Covariance method. The assumption behind it is the same as National Meteorological Center method, which is that forecast errors

can be resembled by forecast tendencies. A problem with this approach is that diurnal and semidiurnal signals are present in the CQC statistics, when the tides are involved in the model. Hence, the forecast lag should be specified.

2.5 Hybrid EnKF system and CQC method

By utilizing the CQC method to estimate the background errors in the EnKF system, a Quick Ensemble Kalman Filter (QEnKF) method is proposed in this work.

To make it clear, we start from the procedure of the EnKF system, the flow-chart of which is shown in Fig.2.1. The figure shows that the first part of the EnKF system consists of an initialization step, which creates the first guess of model state consisting of an ensemble by adding pseudo-random noise with prescribed statistics to the background state. This ensemble model states are then integrated forward in time with the same model conditions until the time when the first observation set becomes available. After analysis, the updated ensemble is then integrated forward to the next date when data are available without adding pseudo-random noise this time and the process is repeated continually.

It is obvious that the ensemble is inherited from the background estimate at the beginning. In another word, the state space described by such ensemble is decided at the very beginning. In the analysis step the ensemble is updated with a gain calculated from that same ensemble, that is the "inbreeding" problem mentioned by Houtekamer and Mitchell (1998). Besides, the EnKF technique seeks an analysis to minimizes the posterior variance (Kalnay, 2003). Hence, after a long time assimilation, the posterior variance (P^a) keeps decreasing (see equation 2.7), a divergence will happen that means the analysis will ignore the observations. Moreover, when the measurements are available with a high frequency interval (like 20 minutes), it is not possible to run an ensemble models and then perform an analysis every time step when measurements are available.

An extension method of the EnKF method is the Gaussian ensemble filter (Anderson, 2001), which tends to address the inbreeding problem. Fig.2.2 gives a schematic illustration of this algorithm. In the Gaussian ensemble filter, only one forecast is integrated forward in time. When the observations are available, the updated ensemble is then computed using a random number generator to produce a random sample from a Gaussian distribution with the covariance previously

given and the mean equal to the forecast state. Hence, at each analysis time step the ensemble is randomly resembled and has a Gaussian distribution. But, the background error covariance is inevitable to be known.

The way we used to estimate the background error covariance refers to the CQC method, by introducing it into an EnKF system, the Quick Ensemble Kalman Filter (QEnKF) method is proposed. The flow chart of this method is shown in Fig.2.3. As we mentioned before, to make a real time assimilation, Breivik and Saetra (2001) developed the QuasiE method. In that method, the ensemble of model states is collected from a representative forecast run at 5.5-hour intervals, which is used to determine a constant error covariance. However, in order to improve the QuasiE method and keep the covariance of the model states flow-dependent, we collect the model states from the actual assimilation run. We use the differences between the model states of the same run to describe the model error, not the relationship of model states of different runs. Meanwhile, the model states in the QuasiE method only involve the velocity, but in the QEnKF method, we include surface elevation, temperature and salinity as well. The assumption behind this method is the same as for the CQC method, i.e., forecast errors are resembled by forecast tendencies (personal communication with Peter Jan Vanleeuwen). This procedure makes the real time assimilation more feasible compared to the traditional EnKF method.

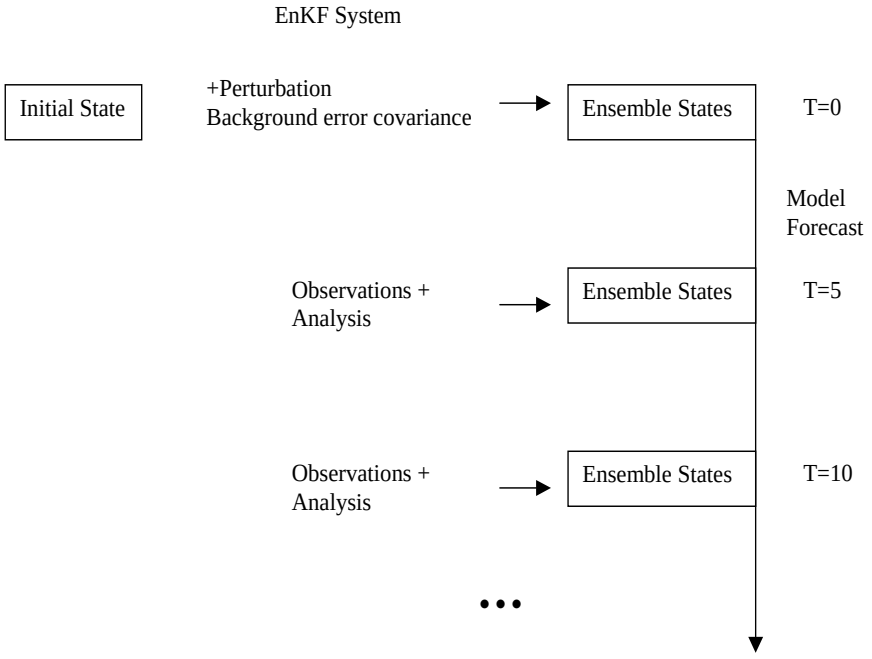

FIGURE 2.1: The procedure used to perform data assimilation cycles with the Ensemble Kalman Filter.

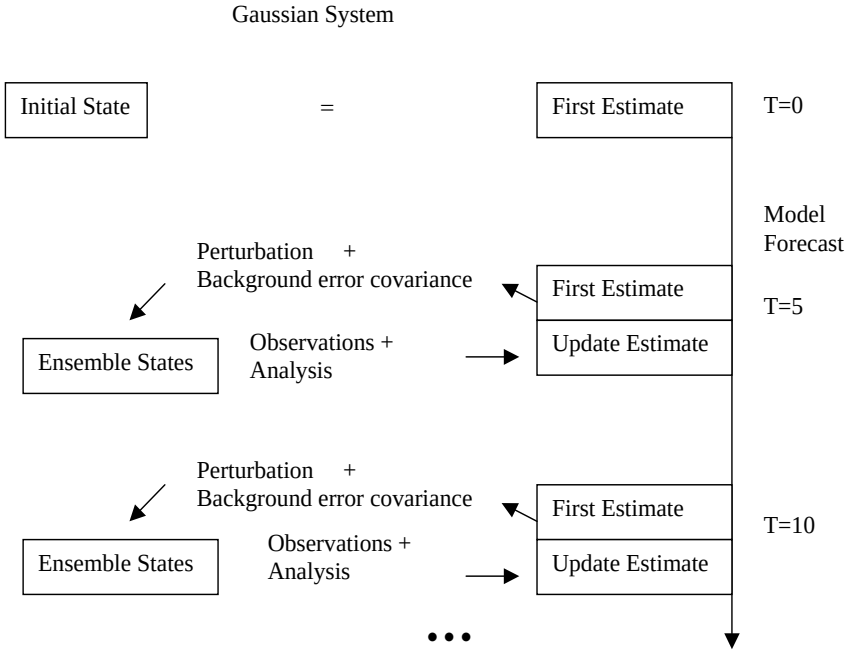

FIGURE 2.2: The procedure used to perform data assimilation cycles with the Gaussian Ensemble Kalman Filter.

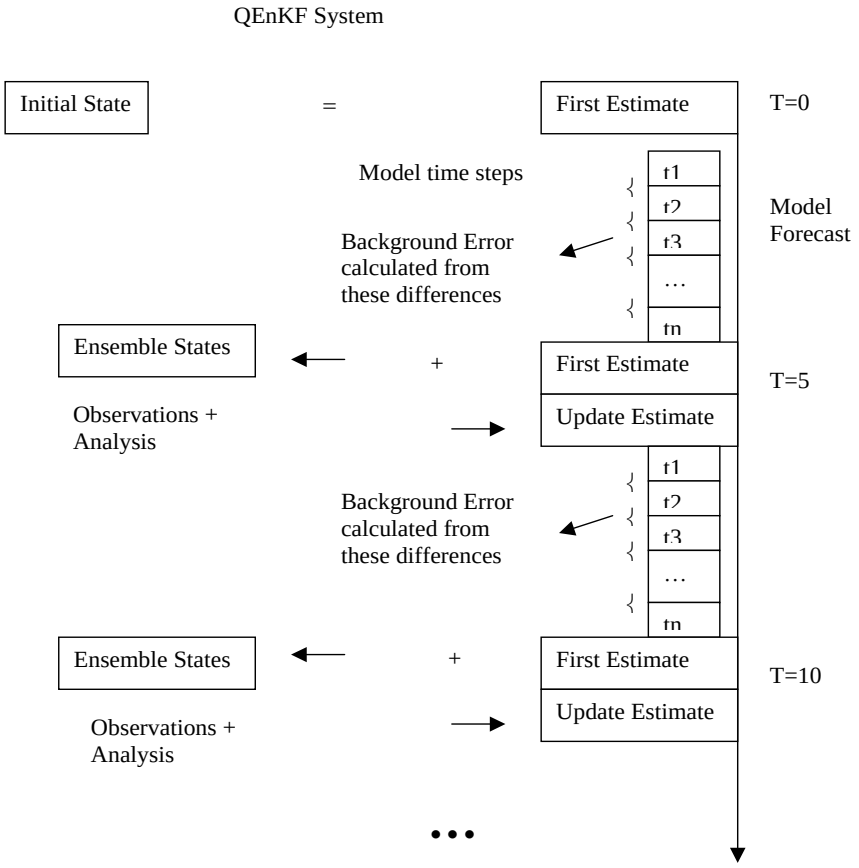

FIGURE 2.3: The procedure used to perform data assimilation cycles with the Quick Ensemble Kalman Filter (QEnKF) method.

Chapter 3

Assimilation with Linear Model

To evaluate the performance and parameters of the Quick Ensemble Kalman filter (QEnKF) method, a linear model is presented here. The reason we use this linear forecast model in this assimilation system is two folds. On one hand, it is simple and quick to be executed; on the other hand, it has a true solution, hence, the validation of assimilation methods is feasible and objective. Besides, the comparison of QEnKF with other methods, like EnKF and Gaussian ensemble filter (GaussEF), is also given in this chapter. The reason we selected these three assimilation methods to do the comparison is because there is common ground among them, since all of them apply an ensemble of model states to represent the model forecast errors. As we described in the end of last chapter, in the EnKF system, an ensemble of perturbed error covariance is used to generate an ensemble of model members at the beginning of the assimilation procedure, after that, such an ensemble of model members is used to calculate the model forecast errors. In the GaussEF method, an ensemble of perturbed error covariances is used at every analysis step. In the QEnKF method, no perturbed error covariance is used, instead, the forecast tendencies are used to reproduce the forecast errors.

3.1 Linear Forecast Model

In the present study, the forecast model used in an assimilation system is a one-dimension, linear, shallow-water model. The formulations of this linear model are

given as follows, with the assumption that no variables change in the y direction.

$$\frac{\partial u}{\partial t} - fv + \frac{\partial \Phi}{\partial x} = 0, \tag{3.1}$$

$$\frac{\partial v}{\partial t} + fu = 0, \tag{3.2}$$

$$\frac{\partial \Phi}{\partial t} + \overline{\Phi}\frac{\partial u}{\partial x} = 0, \tag{3.3}$$

for simplicity, f is set to 1, and $\overline{\Phi}$ equal to 1, too. Then one of the analytic solutions is,

$$\Phi = -\frac{1}{\sqrt{2}}\sin(x + \sqrt{2}t), \tag{3.4}$$

$$u = \sin(x + \sqrt{2}t), \tag{3.5}$$

$$v = \frac{1}{\sqrt{2}}\cos(x + \sqrt{2}t). \tag{3.6}$$

Besides, this analytic solution is treated as the true value of this linear model equations. Ensembles of observations are generated by adding perturbations with covariance equal to 0.002 and mean equal to 0, to the truth. Hence, the error covariance of observations is 0.002. The number of the perturbations is equal to the number of the ensemble. The model is executed for 100, and the observations are available at every fifth model time step.

3.2 Assimilation Experiments

With this setup of the linear model, there are six experiments designed for the comparison of the three assimilation methods, QEnKF, the traditional EnKF and GaussEF. Each method is performed twice, with ensemble number equals to 20 and 100, respectively. The details are described in Table 3.1.

In the experiments with the EnKF method, the flow chart of which is shown in the last chapter (Fig.2.1), an ensemble of model states should be generated at the beginning, and the way we used to generate it is the same as the generation of observation ensemble, that means adding perturbations to the analytic solution with covariance equal to 0.02 and mean equal to 0. Hence, the background error covariance is 0.02 i.e ten times larger than observation error covariance.

In the experiments with the GaussEF method (described in the last chapter with Fig.2.2), an ensemble of model states are reproduced at every analytic time step,

Table 3.1: Assimilation Experiments

Experiment	Method	Ensemble Number	Model Time Steps
$Test1$	EnKF	20	100
$Test2$	EnKF	100	100
$Test3$	QEnKF	20	100
$Test4$	QEnKF	100	500
$Test5$	Gauss	20	100
$Test6$	Gauss	100	100

not only at the beginning. The way to generate these ensembles is the same as in experiments with the EnKF method. Besides, the background error covariance is also set to 0.02, too.

However, in the experiments with the QEnKF method (described in the last chapter with Fig.2.3), the background error is not artificially set to 0.02, but is substituted with the forecast tendencies, which is calculated from the differences of successive outputs of different model time steps.

From the Table 3.1, we can see that the model temporal resolution in $Test3$ and $Test4$, which represent the QEnKF method with 20 members and 100 members, is different. This is because we want to generate the ensembles in the same timescale, one way to address this target is to increase the model time steps.

Fig.3.1 shows the truth (red solid line) and assimilated value (black dotted line) of the solutions ϕ of equations (3.1-3.3) of six tests at the end of the assimilation procedure. The upper panels represent results of tests with 20 ensemble members, while the lower panels represent results of tests with 100 ensemble members. Obviously, with the number of ensemble increases, the shape of ϕ leans to the truth with the EnKF method. However, there is no obvious difference between 20-member runs and 100-member runs with both GaussEF method and QEnKF method, and both of them can give good results. To diagnose the differences between these three methods, we calculate the spatial averaged root-mean-square (RMS) errors, which are assimilated values minus true values.

The RMS error of ϕ-variable is shown in Fig.3.2, where the black line, green line and red line represent the error of the EnKF, GaussEF and QEnKF, respectively. It can be seen from this figure, that with the EnKF method, the RMS error of ϕ is the largest, which is much more decreased by the QEnKF method, and is smallest with the GaussEF method. This can be explained. Since in the EnKF system, the background error covariance is given once and only used at the beginning, which is

represented by the ensemble itself in the assimilation procedure. Unless the number of ensemble is infinite, the ensemble cannot represent the real distribution of the variables. Hence, sampling errors can not be avoided. While the background error covariance is given in every analysis cycle in the Gaussian system, hence the error of this method is the smallest. With the QEnKF method, the background error covariance needs not to be specified, usually it is not possible to known it in a nonlinear complex model, these forecast errors are assumed to be similar to the forecast tendencies. The RMS error with this method is quite similar to that with GaussEF method, and is much smaller compared to the EnKF method. Moreover, the same conclusion can be drawn from the case, when the number of ensemble is changed to 20 (see Fig.3.3). However, when the number of ensemble decreases, the RMS error is found to increase, by comparing Fig.3.2 and 3.3.

The disadvantage of the EnKF and GaussEF methods is that the background error covariance should be known exactly, since it decides the update of the model states. To show the effects of this parameter, two extra tests are implemented by magnifying the background error covariance in the assimilation runs with EnKF and GaussEF, respectively. Fig.3.4 shows the RMS errors of $Test2$ and $Test6$, as well as the assimilation runs with the background error covariance magnified by the factor of 2. The comparison of the black lines indicates that the RMS errors of assimilation runs with the EnKF method increase at least twice after the magnification of background errors. However, the comparison of the green lines indicates that the RMS errors of assimilation runs with the GaussEF method are almost not changed after the same magnification. This can also be explained: according to the analysis equation of the EnKF system, the corrections by assimilation decrease when the error covariance of the model increases, then, the RMS errors increase. However, since the GaussEF method is developed to address the divergence problem of EnKF method, the error covariance after each analysis step does not decrease and is always forced to have Gaussian distribution. Hence, the results of this method which are the mean of ensemble members do not change, naturally the RMS errors are the same after the magnification of background errors.

Nevertheless, when the QEnKF method is applied, the assumption of the background error covariance can be avoided, and the RMS errors are smaller than that in tests with the EnKF method, and are a little bigger than that in tests of the GaussEF method.

3.3 Covariance Modeling

In this section, we focus on covariance modeling, because it is the crucial element in assimilation studies and appliance, which can been detected from the last subsection.

As known, when we use the EnKF method, we assume that the error covariance of the background field is correct at the first moment, that can make sure the developmental error-covariance is also correct. In another word, if we want to get the optimal results, the error covariance of the background field must be correct. However, the error covariance of the background is flow-dependent and complex. Therefore, how to get an error covariance as correct as possible, which is the key point of assimilation schemes, since that directly affects the optimal solutions. In fact, the error covariance is usually the statistical result of the samples. But, where are the samples from? Only from history. But, the movement of the ocean is not exactly periodic, and samples are not from statistics, even we get the correct error covariance from historical data, this only guarantees that the analysis solutions are optimal for that period, not for the present. In addition, to make sure that the variances will be convergent in the iteration, the covariances directly calculated from statistical samples should not be put into model directly. Hence, the statistic dependent on historical samples and uncorrect model solutions are the main sources of error in design of error covariance. Since the probability density at analyzed periods is not the same as in the past, the ensemble forecast has the benefit of creating probability density functions of samples with "real time" relevance. Due to the upper statements, the GaussEF method can not be used in a realistic circulation model, since the prior background error covariance is not possible to specify.

The biggest difference between the traditional EnKF and our QEnKF is the sample of background errors. In the former method, a lot of independent, but sibling, random model runs are developed by the same model conditions to represent the forecast errors. However, in the QEnKF method, the forecast errors are assumed to be similar to the forecast tendencies. The forecast error covariances of both method are flow-dependent, however, the RMS errors in the QEnKF method are much smaller than that in the EnKF method.

In the QEnKF method, two parameters should be evaluated, one of which is model time interval, the other is ensemble size.

For the test of these two parameters, we apply an extra test ($Test7$), which is

almost the same as $Test4$, but with an ensemble number equal to 20. Hence, the difference between $Test7$ and $Test3$ is the model time interval, the latter is 5 times larger than the former. While, the difference between $Test7$ and $Test4$ is the ensemble number, the latter is 5 times larger than the former.

Fig.3.5 gives the comparison of RMS errors of ϕ in these three tests. The black dotted line, the green dashed line, and the red solid line in Fig.3.5 represent the RMS errors of $Test3$, $Test4$ and $Test7$, respectively. From the picture, we can see that there is no obvious difference of RMS errors between $Test4$ and $Test7$, that means when the model time interval is fixed, the forecast tendencies are almost fixed, and the effect of ensemble size has no significance anymore. However, the RMS error in $Test3$ is little bit larger than that in $Test7$, that means when the size of the ensemble is fixed, the RMS error decreases with the model time interval. Since the forecast error will decrease, when the model time interval decreases. But in all these tests, the linear model is assumed to be perfect, without errors from discretization, forcing, or boundaries, etc. In a realistic, complex, and nonlinear ocean model, the situation will be definitely different. Nevertheless, the results of this linear model are inspiring, especially, the limitation of ensemble size is reduced by the usage of the newly developed assimilation method (QEnKF).

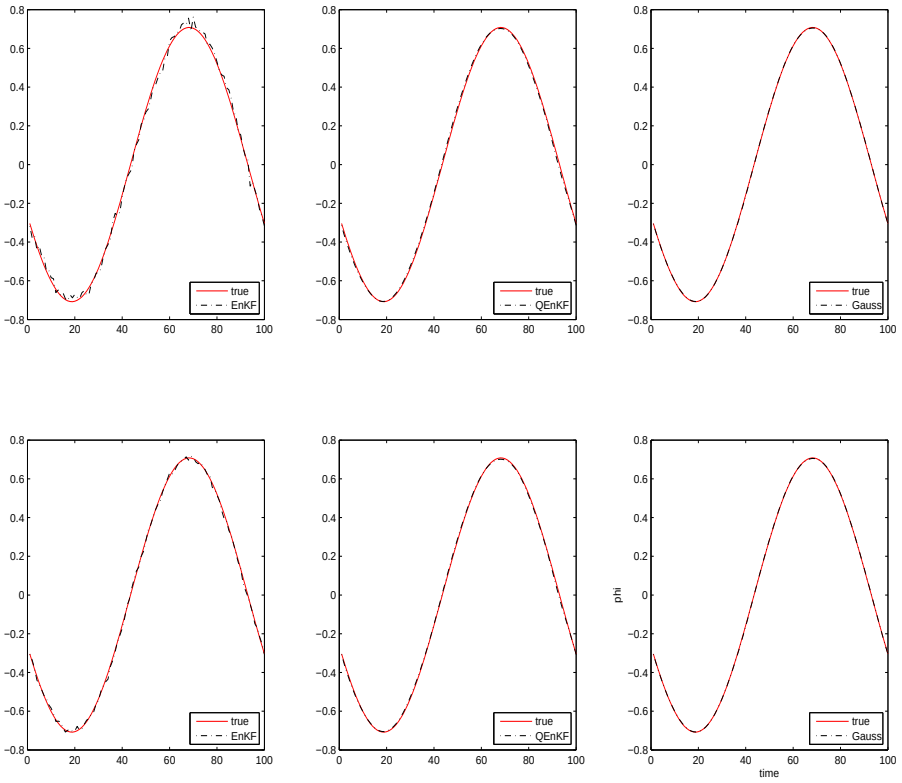

FIGURE 3.1: The true (red solid line) and assimilated value (black dotted line) of ϕ at the end of simulation with different methods and ensemble numbers. The ensemble numbers equal to 20 in the upper panels, while 100 in the lower panels.

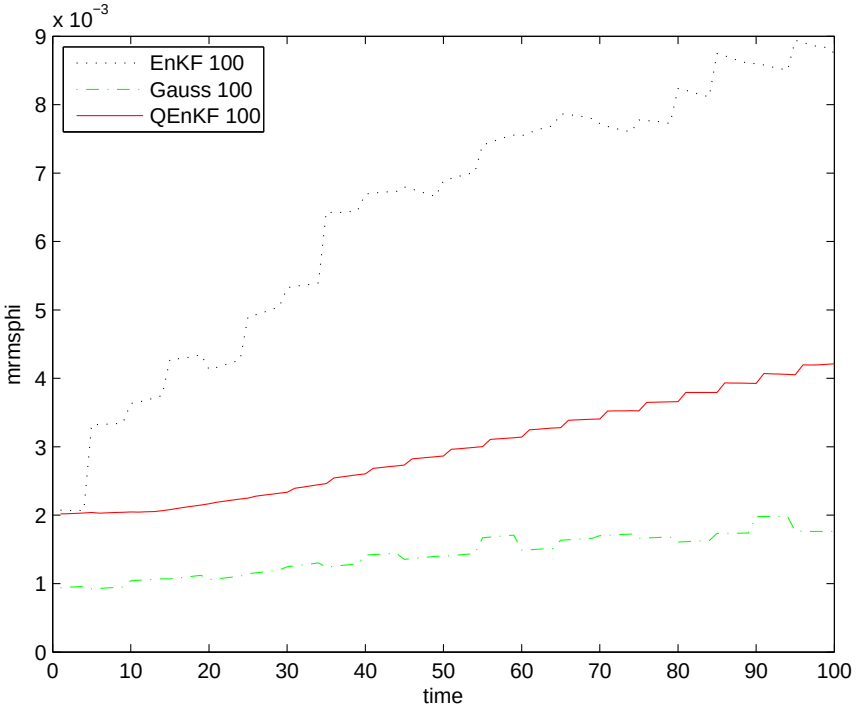

FIGURE 3.2: The spatial averaged root-mean-square errors of the tests using EnKF method (dotted line), GaussEF method (dashed line) and the QEnKF method (solid line). The ensemble numbers of all the tests equal to 100.

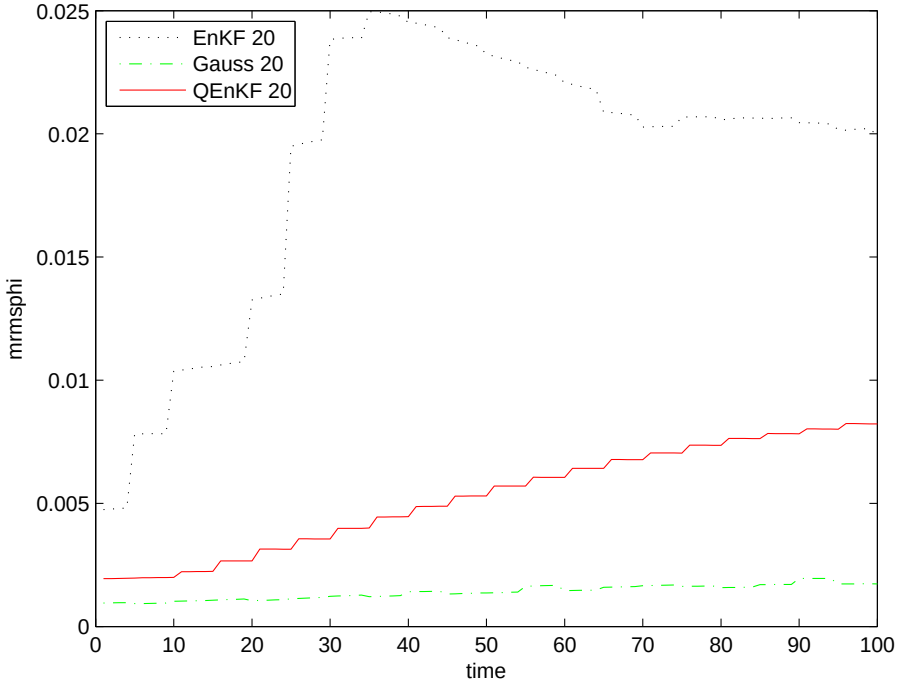

FIGURE 3.3: The spatial averaged root-mean-square errors of the tests using EnKF method (dotted line), GaussEF method (dashed line) and the QEnKF method (solid line). The ensemble numbers of all the tests equal to 20.

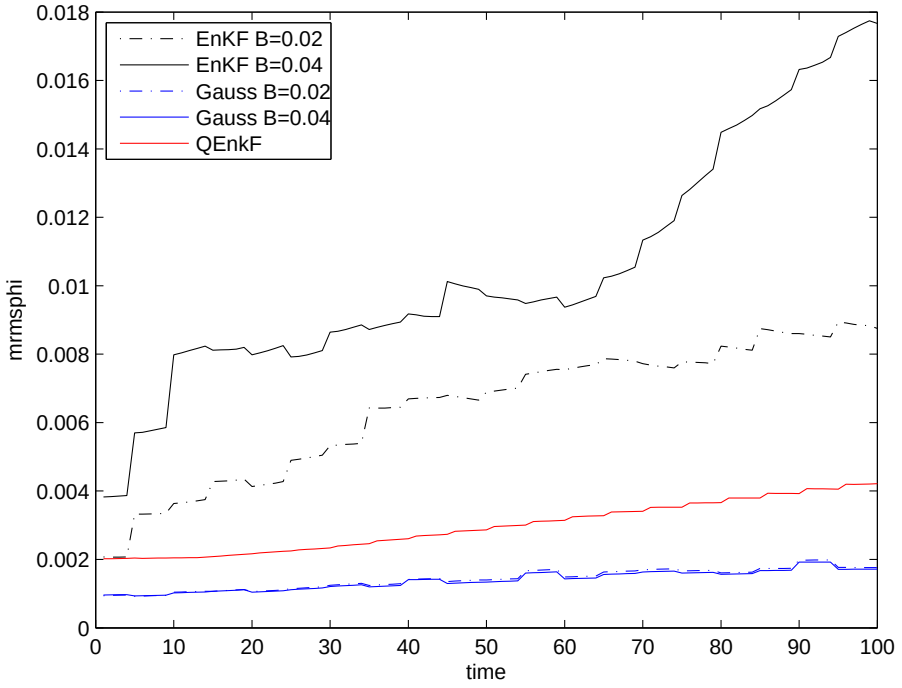

FIGURE 3.4: The spatial averaged root-mean-square errors of the tests using different methods and assumed backgroud errors, which are shown in the label. The ensemble numbers of all the tests equal to 100.

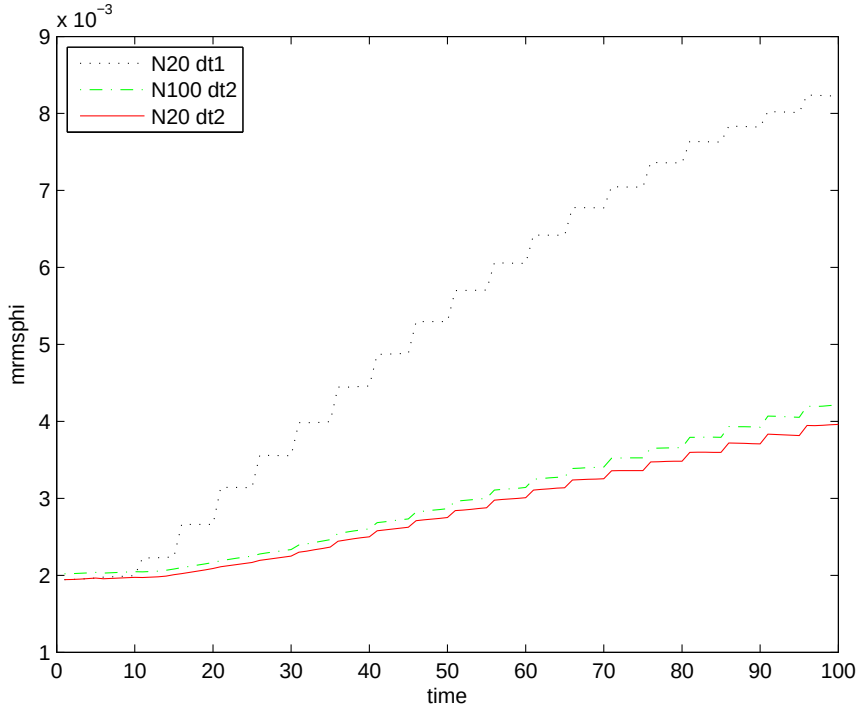

FIGURE 3.5: The spatial averaged root-mean-square errors of the tests using QEnKF method with different ensemble numbers and model time steps. The $dt1$ and $dt2$ represent model time steps that equal to 100 and 500, respectively.

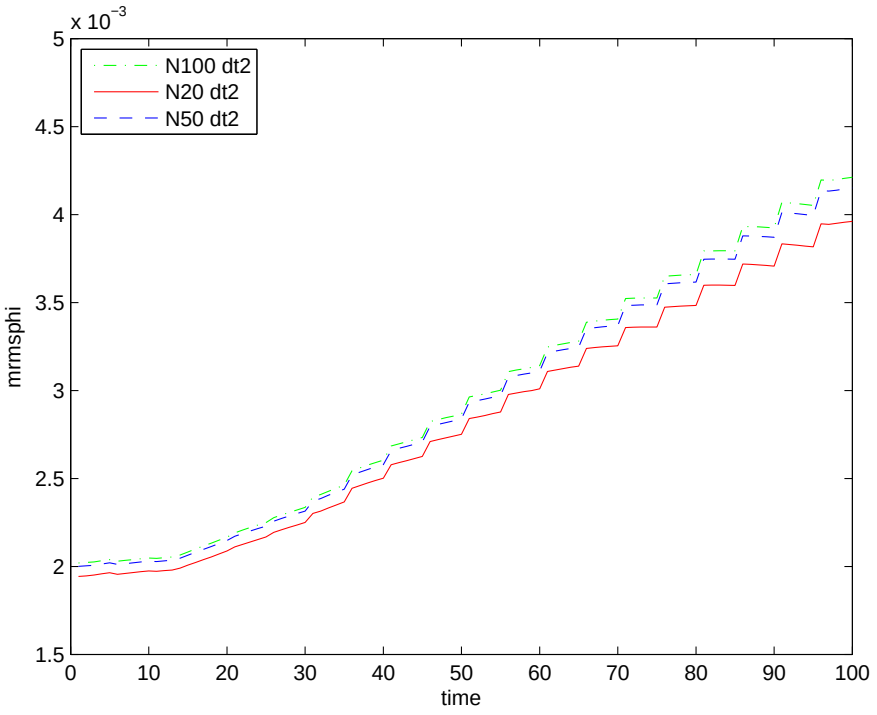

FIGURE 3.6: The spatial averaged root-mean-square errors of the tests using QEnKF method with the same model time steps , but different ensemble numbers.

Chapter 4

Assimilation with Nonlinear Model

In the last chapter, the QEnKF assimilation method is validated in a perfect linear model. However, the benefit of the traditional EnKF is its usage in strongly nonlinear systems. Hence, our final target is also to apply the QEnKF method into a complex, realistic, nonlinear model. The model we used is HAMburg Shelf Ocean Model (HAMSOM). In this chapter, we will give a brief introduction of this model, as well as a description of the model domain, and the model validation.

4.1 Hamburg Shelf Ocean Model

HAMburg Shelf Ocean Model (HAMSOM) is a high resolution, three-dimension, baroclinic, free surface, shallow water equation model. Its numerical scheme is described by Backhaus (1985), and the further modification in the turbulent closure scheme by Pohlmann (1996a,b). HAMSOM has been used in a lot of projects, simulating several shelf seas worldwide (Backhaus and Hainbucher, 1987; Backhaus et al., 1991; Pohlmann, 1991; Becker et al., 1999; Harms, 1992; Carbajal, 1993; Pohlmann, 1996a; Hainbucher and Backhaus, 1999; Kauker and Langenberg, 2000), etc. Besides, it has been also coupled with other models, like ecosystem models (ECOHAM,ERSEM), atmospheric model (REMO), and both Lagrangian and Eulerian models for sediment transport. Hence, HAMSOM is well suitable for simulation of shelf current.

The numerical scheme of HAMSOM is defined in z-coordinates on an Arakawa

C-grid. The governing primitive equations (Pohlmann, 1991) for shallow waters combined with the hydrostatic assumptions are implemented. In order to calculate the Coriolis term with a second order accuracy in time, a rotational matrix is used. To solve the free surface problem, the vertical transfer of momentum and water mass properties are calculated. To reach stability even for greater time steps, several terms are solved implicitly. These are equations for the vertically integrated continuity and the barotropic pressure, the combination of which describes the surface gravity waves. The vertical shear stress and the diffusion terms are calculated implicitly as well. A non-linear implicit friction law as well as the full kinematic boundary condition are applied at the bottom. In order to minimize problems arising from longer time-steps, a rotational matrix is applied for the Coriolis term, guaranteeing a second-order accuracy in time.

An explicit formulation is used for the advective terms of the momentum equation and for the transport of temperature and salinity. To conserve eddies and frontal structures, an Arakawa J7 algorithm is implemented.

To parameterize horizontal sub-scale processes, a Smagorinsky scheme (Smagorinsky, 1963) is used to calculate the horizontal turbulence exchange. This allows for non-constant coefficients, dependent on the horizontal sheer stress. To calculate the vertical turbulent viscosity coefficient, the approach of Kochergin (1987) was implemented by Pohlmann (1996a). The vertical viscosity influences the depths of the surface and bottom mixed. The horizontal diffusion is determined by the Smagorinsky scheme . Besides, a method used to calculate the vertical and horizontal advection of temperature and salinity is related to the difference scheme of second order accuracy from Lax and Wendroff (1960).

It is known that the EnKF assimilation process will need a high amount of CPU time. One of the reasons we chose this model is because of the parallelization of its code by means of the domain splitting method (Pohlmann, 2006), which makes the implementation much simpler and quicker.

The presented calculations have been performed at the German Climate Computing Center (DKRZ). In order to optimize the model code for this computer architecture, the code was parallelized to run simultaneously on several CPUs.

4.2 Norwegian Coastal Current

Our model domain is shown in Fig.4.1, which is a part of Norwegian western coast, by considering of the HF radar coverage (rectangular shape in this figure). The current system in our model domain is dominated by the Norwegian Coast Current (NCC). The Norwegian coastal region is the spawning ground for a number of important oceanic fish stocks, and the physical environment has an impact on the recruitment, growth and geographical distribution of these stocks. Hence, a lot of studies about its phenomena and character have been done, like Mork (1981); Haugan et al. (1991); Saetre and Mork (1971); James (1987); Ikeda et al. (1989), etc. Here, a brief description about the NCC is given.

The NCC flows northward along the west coast of Norway in the upper $50 - 100$ meter of the water column (Helland-Hansen and Nansen, 1909), which originates primarily from the freshwater outflow from the Baltic and the freshwater runoff from Norway. The Baltic Sea provides the bulk of brackish water to the current system, but the North Sea and the Norwegian rivers also contribute significant amounts of water. A west boundary of NCC is formed by a southward inflow of Atlantic Water from the North Atlantic current, which results in a warm core.

In addition, a well-defined front is found at this west boundary, which is between the cold, low-salinity Norwegian current and the warmer, high-salinity Atlantic water. This front was observed in detail by Mork (1981), as well as Johannessen et al. (1989), which are shown in Fig.4.2 and Fig.4.3, respectively. The latter picture is a satellite IR image, which shows the temperature front between the coastal and Atlantic water in an area comparable to our model domain.

On average, the temperature of the Norwegian Coastal Current in winter time ranges from 2 to 5 ℃, and the salinity is less than 34.8 psu. The Atlantic Water, on the other hand, has a temperature exceeding 6 ℃ and a salinity greater than 35 psu.

Besides of the front at the west boundary of the NCC, another important feature of NCC is the existence of meanders and eddies, which are important in a variety of marine applications, like offshore drilling operations and fisheries.

Mesoscale eddies and meanders in the Norwegian Coastal Current have been studied by using remote sensing and in situ observations. The observations also include combined Acoustic Coppler Current Profiler, towed, undulating CTD, which were used by Johannessen et al. (1989). Most observations indicate that current meanders and eddies exist along the NCC from the Skagerrak into the Norwegian

west and northwest coasts, they have wavelengths of $50-100km$ and northward velocities of $10-20cm/s$, and periods of $5-7$ days. Moorings deployed during the Norwegian Continental Shelf Experiment (NORCSEX '88) detected current velocities of $7cm/s$ to $20cm/s$ with a mean northeastward direction. The direction of velocity was almost parallel to the isobaths, indicating significant topographic steering.

Meanwhile, Oey and Chen (1992b) simulated the meanders and eddies in the NCC with a nested-grid model. The authors pointed out that due to the local and nonlocal wind forcing, the NCC has large variations in its transport and its water properties. One result of flow instability processes is the generation of the meanders or eddies.

Based on the observations and simulations mentioned above, they concluded that instabilities play a major role in the development of these waves and eddies (Mysak and Schott, 1977; Vinger et al., 1981; Ikeda et al., 1989), and the barotropic instability explained the generation of eddies between 60°N and 61°N. Meanders and eddies generated upstream by baroclinic instabilities grow and also enter this region. The resulting interactions complicate the eddy fields.

They also pointed out that the cyclonic eddies were highly asymmetric and extended to the bottom, which indicates a significant barotropic components. Besides, topography is also important, and eddies may be produced over a seamount or bank (Eide, 1979). Oey and Chen (1992a) also found that the transport variations can be expected to be important in the development of the NCC meanders and eddies further north.

In the end, the meanders and eddies are the combined effects of topographic steering, vortex stretching, and barotropic instabilities. These mesoscale features may represent a significant source of energy in the coastal region, as well as influence of the exchange of salt and heat between the deep and shallow seas, and may also affect the larger-scale circulation in the Norwegian Sea.

4.3 Model Configuration

In our study, the model grid extends over 3.5 degree offshore and 3 degree in the alongshore direction. The 1 minute resolution topography (Fig. 4.1) is derived from the General Bathymetric Chart of the Oceans (GEBCO) data. The picture

shows an obvious trench from northwest to southeast, and the largest depth is around 400 meters.

The z-coordinate system is applied in the vertical direction using a maximum of 30 layers. The resolution in the upper 30m is 3m, the layers between 30m to 60m have 5m thickness, and the layers between 60m to 150m have 10m thickness, the $26th$ and $27th$ layers are 25m, and the last two layers are 50m. The model surface forcing parameter, such as heat flux, air temperature, relative humidity, cloud cover, precipitation, as well as wind are supplied by NCEP (Kalnay et al., 1996). All these variables are given every 6 hours, and the initial temperature and salinity fields are obtained from the climatological LEVITUS data set (Levitus et al., 1994).

However, the spatial resolution of the meteorological forcing data is relatively coarse for our domain, this is also the reason why an employment of the HF-radar data to correct the simulation of the shelf circulation is expected to give a significant improvement. As known, tides are an important element for the high-frequent shelf circulation, so the tidal influence is included in our model simulation by adding the tidal elevation to the sea level height at the open boundaries. The tidal elevation is calculated according to amplitude and phase of $M2, S2, N2, K2, K1, O1, P1, Q1$, which are extracted from OSU Tidal Prediction Software (OTPS).

4.4 Model Validation

Since the tidal elevation calculated from OTIS data is only added to the open boundaries, by the model integration for 45 days, the tidal parameters, amplitude and phase, over the whole model domain can be extracted from the sea surface elevation provided by the HAMSOM model. Hence, by comparing them with the parameters directly derived from OTPS data, we can evaluate the performance of the simulation with respect to tides by our model.

Fig. 4.4 shows the horizontal distribution of the amplitude and phase of the M2-tidal constituent extracted from model results (left panel) and OTPS (right panel), respectively. These pictures indicate that model can reproduce tidal elevations with an acceptable accuracy. The difference of amplitude (maximum phase error) is around $5cm$.

To validate the simulation of temperature, the Modular Ocean Data Assimilation System (MODAS, (Fox et al., 2002)) is used, which has a horizontal resolution of 0.125 degree. Fig.6.15 shows the surface temperature distribution of MODAS data (left panel) and our model results (right panel) at the same day. The patterns of temperature distribution in two data sets are similar, and the same conclusion can be arrived at from Fig.4.6, which is the same issue at another arbitrary day.
In addition, as we mentioned previously the front in our model area is a crucial feature, here we present a comparison of it between our model results and other studies, which is shown in Fig.4.7. The lower panel of it is the output from the HSMSOM model, and the upper one is cited from Johannessen et al. (1989), which is a satellite IR image. Even though, these two figures represent two different years, the existence of front in both is almost the same. Hence, the ability of simulation of reasonable temperature by HAMSOM is acceptable.

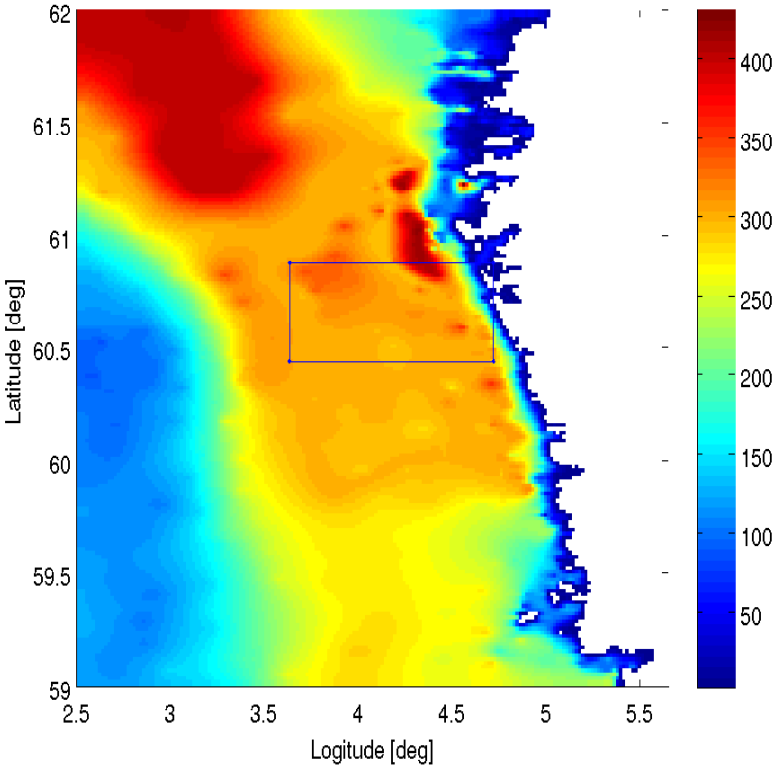

FIGURE 4.1: Model domain topography (m), with the rectangular area representing the radar data domain.

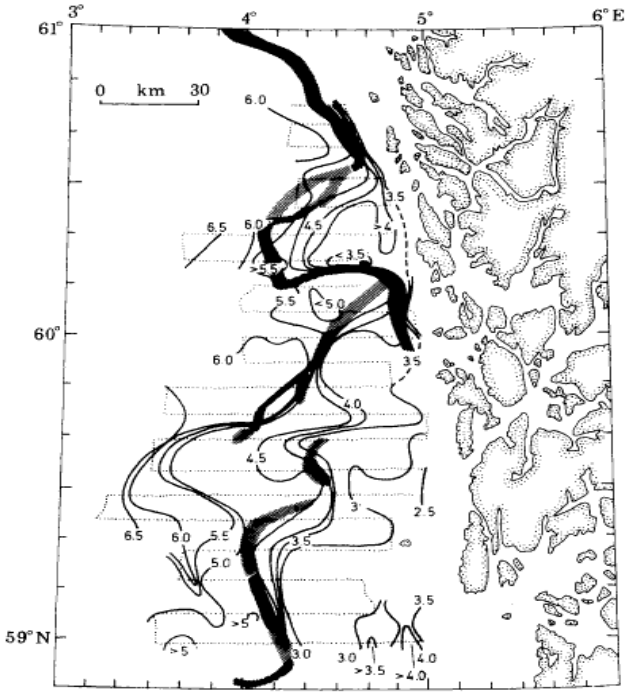

FIGURE 10. *In situ* surface isotherms (°C), and front positions (thick lines) as determined by satellite images, during 15–18 March 1979 (NORSEX-79).

FIGURE 4.2: From Mork (1981) with the description shown in the caption of the original picture.

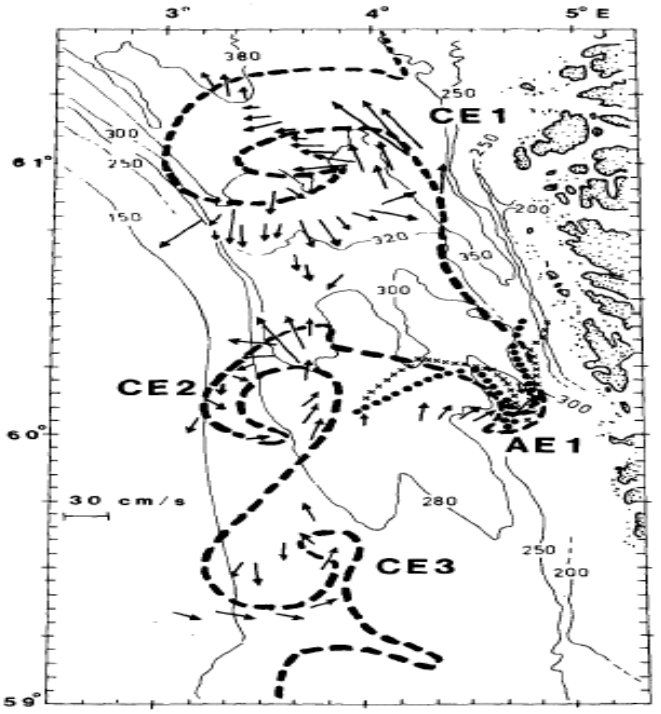

FIG. 3. Bathymetric map (units in meters) with temperature front between coastal and Atlantic water (dashed line), obtained from the IR images on 25 and 27 February, and SeaSoar temperature measurements at 25 m. In addition, a selection of ADCP current data at 25 m is presented as arrows. The scale of the current is indicated in the western part of the map. The combination of temperature and current data shows the existence of three cyclonic eddies (CE1, CE2 and CE3), and one anticyclonic eddy (AE1). Trajectories of two Argos drifters from 1–3 March, deployed to the southwest, are indicated by dots and crosses.

FIGURE 4.3: From Johannessen et al. (1989) with the description shown in the caption of the original picture.

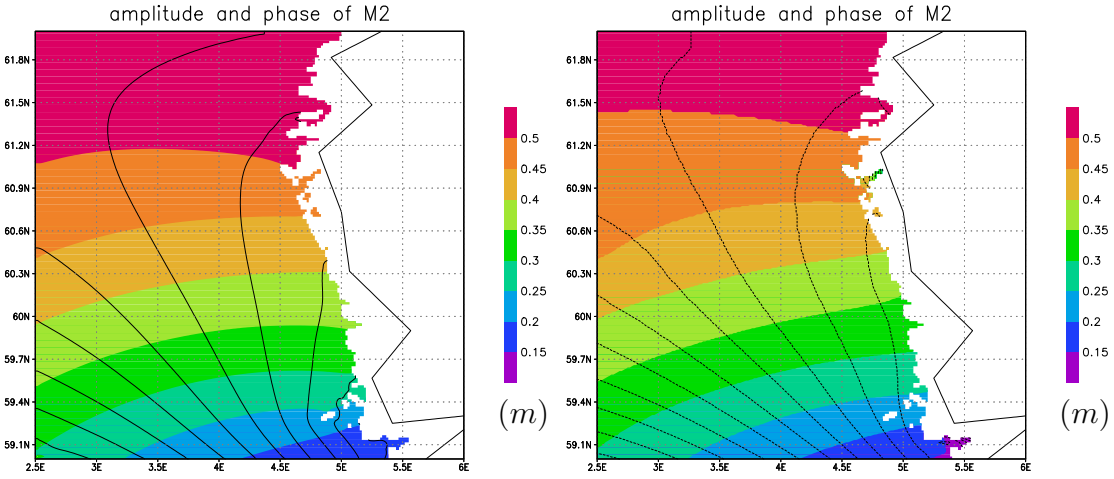

FIGURE 4.4: The amplitude (shading) and phase (contour) of M2 tide are extracted from model results (left panel) and OTPS data (right panel)

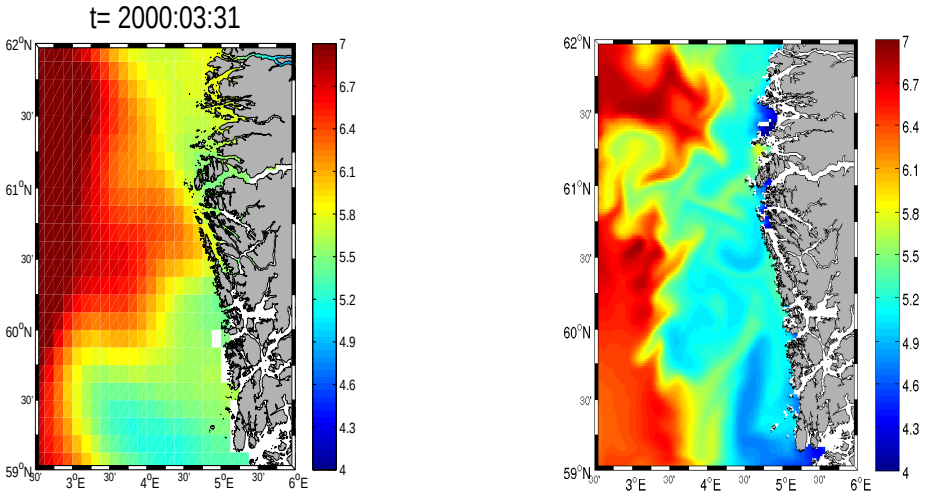

FIGURE 4.5: Surface temperature fields of MODAS (left panel) and HAMSOM simulation (right panel) on March 31, 2000.

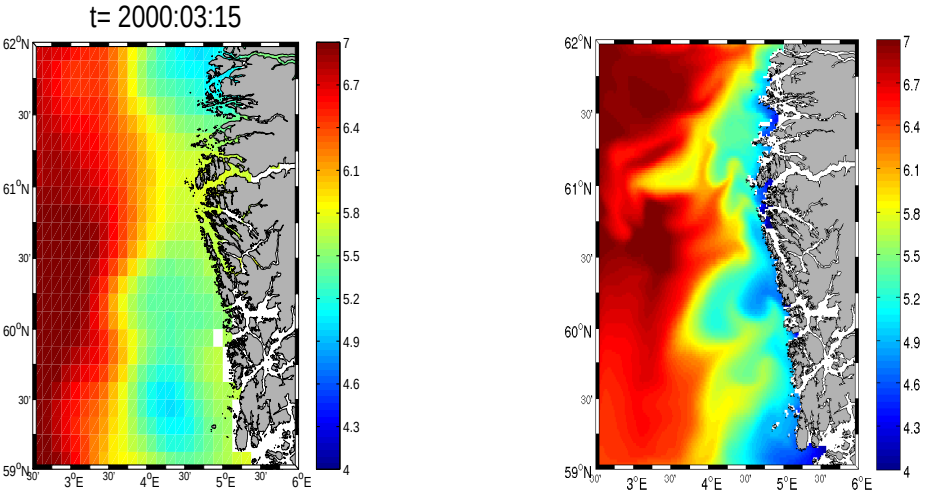

FIGURE 4.6: Surface temperature fields of MODAS (left panel) and HAMSOM simulation (right panel) on March 15, 2000.

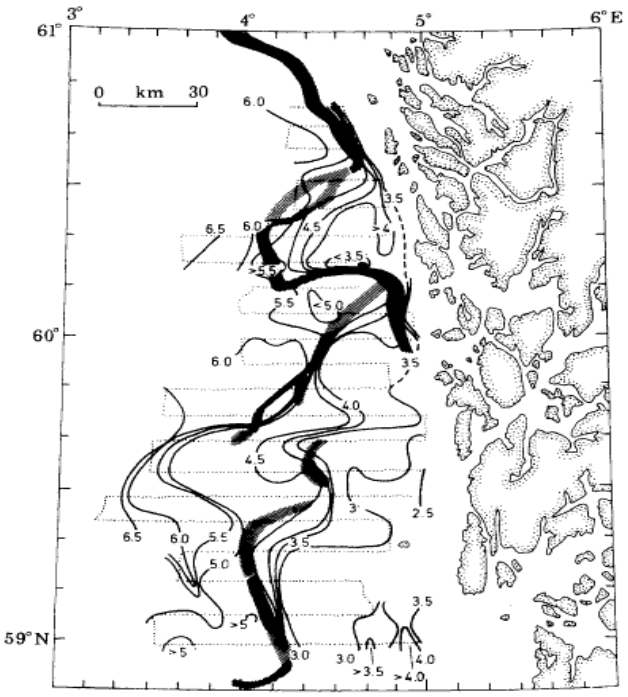

FIGURE 10. *In situ* surface isotherms (°C), and front positions (thick lines) as determined by satellite images, during 15–18 March 1979 (NORSEX-79).

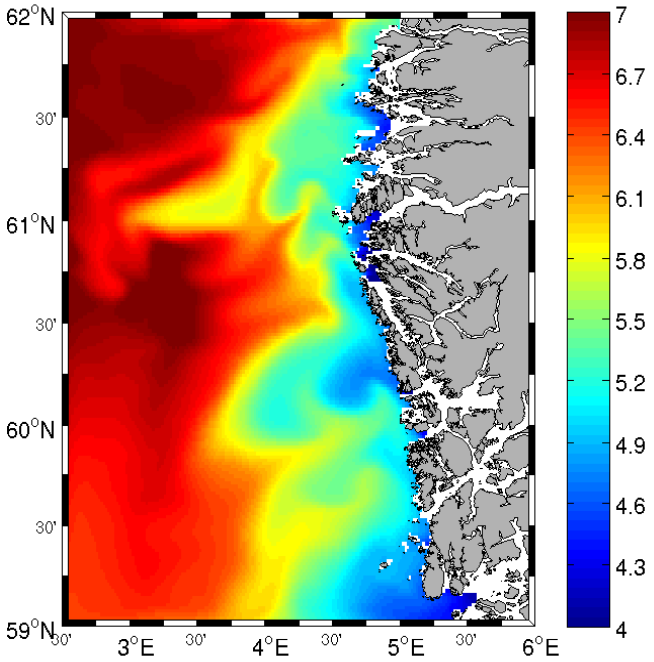

FIGURE 4.7: Surface fronts of the satellite data from Mork (1981) (upper panel) and HAMSOM simulation (lower panel).

Chapter 5

Radar Data

The HF radar called "Wellen Radar" (WERA) are mounted on the islands of Lyngøy and Fedje off the west coast of Norway. The area selected covers the approach to two large oil terminals and is characterized by strong eddy activity. WERA measures surface currents within an area of about 40 km by 40 km with a spatial resolution of 1km and with temporal sampling of 20 minutes. The radar systems are deployed along the coast and measure radial current speeds. Hence, two sites are necessary for composing a two-dimensional current vector. The surface current measured is horizontally averaged over several km^2 (range and azimuthal resolution), vertically over about the upper 0.5m of the ocean, and temporally over some 10 minutes (measuring time). Each radial current velocity is a statistical result from samples of velocities derived from lines in the Doppler spectrum (Gurgel and Antonischki, 1997; Gurgel et al., 1999).

5.1 Velocity and Accuracy of HF Radar Data

The way to calculate the velocity and its accuracy of HF radar data is as follows: Assume there are K samples of a radial current velocity $V_{rad}(i)$ derived from lines in the Doppler spectrum, and each of velocity has a backscatter power $P(i)$ and a signal-to-noise value $StoN(i)$. The Doppler spectrum consists of N_{fft} spectral lines.

In the case of beam forming, the K samples are taken from the area around the

two first order Doppler peaks, hence, K equals to $\pm N_{fft}/16 + 2$.
From these K samples, the radial current velocity $\overline{V_{rad}}$ is calculated as

$$\overline{V_{rad}} = \frac{\sum_{i=1}^{K} V_{rad}(i) StoN(i)}{\sum_{i=1}^{K} StoN(i)} \tag{5.1}$$

The variance of the radial current velocity σ^2 is calculated as

$$\sigma^2 = \frac{\sum_{i=1}^{K} V_{rad}(i)^2 StoN(i)}{\sum_{i=1}^{K} StoN(i)} - \overline{V_{rad}}^2 \tag{5.2}$$

The accuracy of the radial current velocity $Acc(\overline{V_{rad}})$ is calculated as

$$Acc(\overline{V_{rad}}) = \frac{\sigma}{\sqrt{K}} \tag{5.3}$$

The data we used are already converted in east and north directions. Fig. 5.1 gives an overview on the area and typical radar coverage during the experiment. The light blue areas mark the ship entrances to the oil terminals. The radar coverage may change because of radio interference, sun spot activity, varying sea state, etc. Fig. 5.2 provides the geometric accuracy of velocity (GAOV), which is the geometric error made when combing two radial current components, and sequently has been translated to u- and v- components of the radar current vectors. Obviously, the GAOV for the u-component is much smaller than for the v-component, i.e., the observation errors in the former are much smaller than in the latter. Since the accuracy is calculated from the variance of the radial current velocity, it should be the diagonal part of error covariance matrix of the measurements.

5.2 Model vs Radar data

In the last chapter, we validate our model results with OTPS and MODAS data, however, since our ultimate target is to import the information of radar current data into our HAMSOM model, the comparison of radar currents and our modeled currents need to be implemented to assess whether the present model is capable of adequately representing the dominant physical processes of the shelf circulation off Norway.

5.2.1 Correlation

As we mentioned before, the QEnKF method uses the correlationship of model states between two difference runs to substitute the error covariance. According to the equation (2.17) in the second chapter, let indices i and j denote model state variables and k, l denote observations, respectively, the model state vector projected to the observation space can be rewritten

$$H\varphi^f = \{\varphi_k^f\}, k = 1, ..., m, \tag{5.4}$$

and the model error covariance matrix P^f can also be rewritten

$$P^f = \{Cov(\varphi_i^{f'}, \varphi_j^{f'})\}, i, j = 1, ..., n. \tag{5.5}$$

with the total number of model variables equal to n, and of observations equal to m. Besides, the primes indicate deviations from the mean of φ^f.
Similarly, by projecting the P^f to the observation space,

$$P^f H^T = \{Cov(\varphi_i^{f'}, \varphi_k^{f'})\}, i = 1, ..., n, k = 1, ..., m, \tag{5.6}$$

is the error covariance between model variable i and observation k. Hence, the purpose of the inverse weight matrix in equation (2.20) is to weight observations according to their importance. For example, in a cluster of observations, one more data point will normally not add much information as the internal correlation between the observations will be high. Conversely, a solitary observation in a critical location may be heavily weighted. The inverse weight matrix achieves this by balancing the error covariances between observation locations k and l as predicted by the numerical model,

$$HP^f H^T = \{Cov(\varphi_k^{f'}, \varphi_l^{f'})\}, k, l = 1, ..., m, \tag{5.7}$$

against the "instrumental" quality of the observations and internal covariance, which is contained in the observation error covariance matrix,

$$R = \{Cov(d_k^{'}, d_l^{'})\}, k, l = 1, ..., m. \tag{5.8}$$

The whole explanation above is originally cited from Breivik and Saetra (2001). This is also the reason why we study the correlationship of u and v components,

and the cross-correlation between them, from both radar velocity and modeled velocity.

Fig.5.3(a,b) shows the correlationship between the u- (or v-) velocity at a specific location (marked by star) and u or v at all other radar grid points. The same issue for model data is given in Fig.5.3(c,d). u is the across-shore current presented in left panels and v the alongshore current presented in right panels. The correlation of u velocity shows the behavior of decorrelation with radial distance, which is longer in model data than in radar data. The spatial correlation of both u and v is little higher in modeled data than in radar data. Fig.5.4 shows the cross-correlation between u velocity at the specific location and v velocity at all the other radar grid points (left panel) or model grid points (right panel), which is found quite strong, too. These comparisons demonstrates that the modeled and observed correlation or cross-correlation fields have similar characteristics, and with high values in the v direction. The structure of this spatial correlation pattern is surprisingly rich.

In order to assess the correlationship with other variables and elsewhere, the vertical correlation is given in Fig.5.5. The across-shore current (u) exhibits a slightly stronger correlation with the hydrography than the along-shore (v) current. However, both u and v velocities do not have strong correlation with the hydrography, especially with the depth increasing. Negative correlation indicates that across-shore currents advect fresh and cold coastal waters away from the coast. The along-shore surface current is completely detached from the hydrography and only at about 50-m depth does the correlation rise above an absolute value of 0.2. The model statistics reveal a strong surface current to deeper current correlation, but a significantly weaker cross correlation between current components. Note also the immediate drop in correlation at the surface to about 0.8 at 20-m depth. This illustrates how the wind energy is distributed in the upper water column.

5.2.2 Empirical Orthogonal Function

In order to see the dominant current pattern in this radar area, here, we present an Empirical Orthogonal Function (EOF) analysis of the radar surface currents, as well as the simulated currents by HAMSOM.

Fig. 5.6 shows the first mode EOF (left panels) as well as the second mode (right panels) for the radar data (upper panels) and modeled data (lower panels), respectively. The first modes for both data sets are quite similar, and the explained

variability of them is 52% and 69%, respectively. Obviously, the main direction of the current in this area is northward. However, the higher order EOFs show a big difference between radar data and model results, in which a more stronger jet-like structure exhibits in the modeled data than in observations, and the core of jet is a little further away from coast in the modeled data than in observations. The reason for the difference is unknown, may be caused by the baroclinic circulation, or the topography, as our model used a climatological temperature and salinity as initial conditions, and the resolution of topography is relatively coarse near the coast.

5.2.3 Current Differences between Simulation and Radar data

The differences in currents between model simulation and radar observation, are usually known as innovations in terminology (Evensen, 2003; Dee, 2005), which are the residuals by deducting the background (model simulation) from the observed value. And here we named these differences as errors, since we assume that the observation is more reliable. According to equation (2.21), the importance of these errors is apparent.

Fig.5.7 shows the spatial root-mean-squared (RMS) errors of the $u-$ component (right panel) and $v-$ component (left panel), which are averaged over time series (Feb.$8th$ to Mar.$31st$). The first impression of this picture is that the RMS errors of $u-$ component is smaller than of $v-$ component. The obvious reason for that is the velocity values in $v-$ direction are much bigger than in $u-$ direction, which is mentioned in the introduction of NCC and also was shown in the EOF analysis. In addition, the figures indicate that the errors are smooth, which means there are no obvious spatial structures over the radar area, especially in $u-$ direction.

The spatial averaged RMS errors are shown in Fig.5.8 as time series, which also demonstrate the same conclusion as could be drawn from Fig.5.7. In addition, the more important feature shown by this picture is that the errors or differences are obviously periodic. This is in agreement with the statement of Dee (2005), which is errors in models and data are often systematic rather than random in reality.

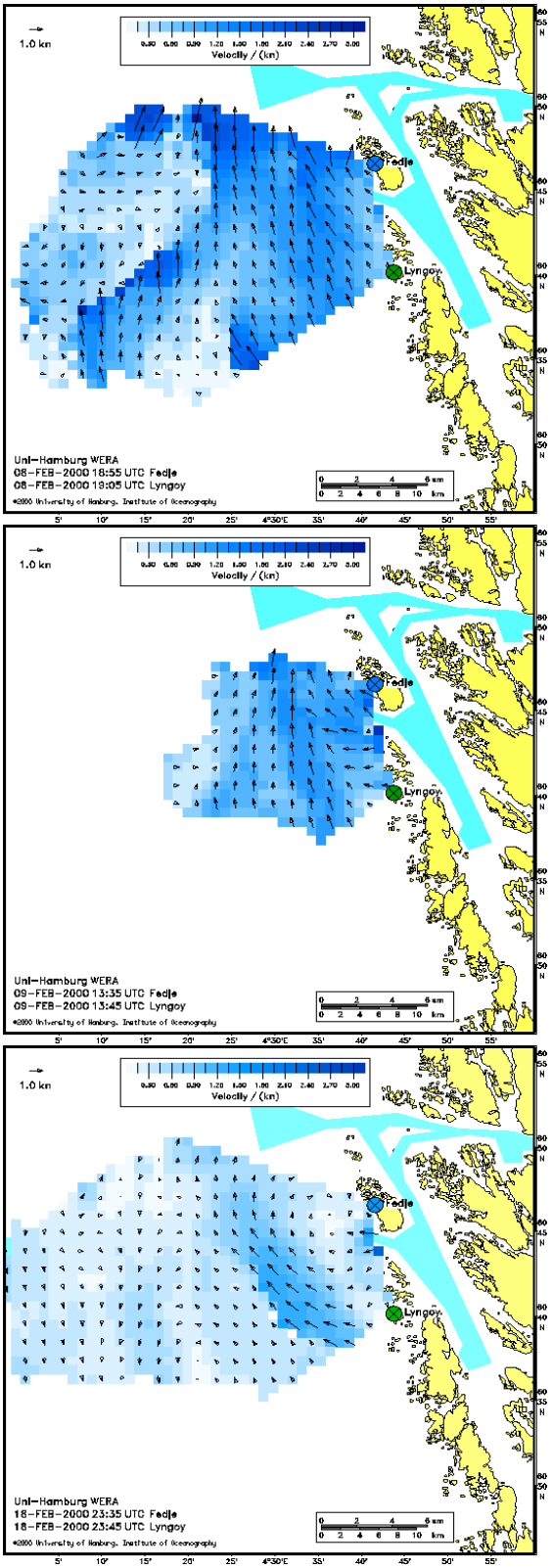

FIGURE 5.1: An overview of the typical radar coverage measured by the Wera radar.

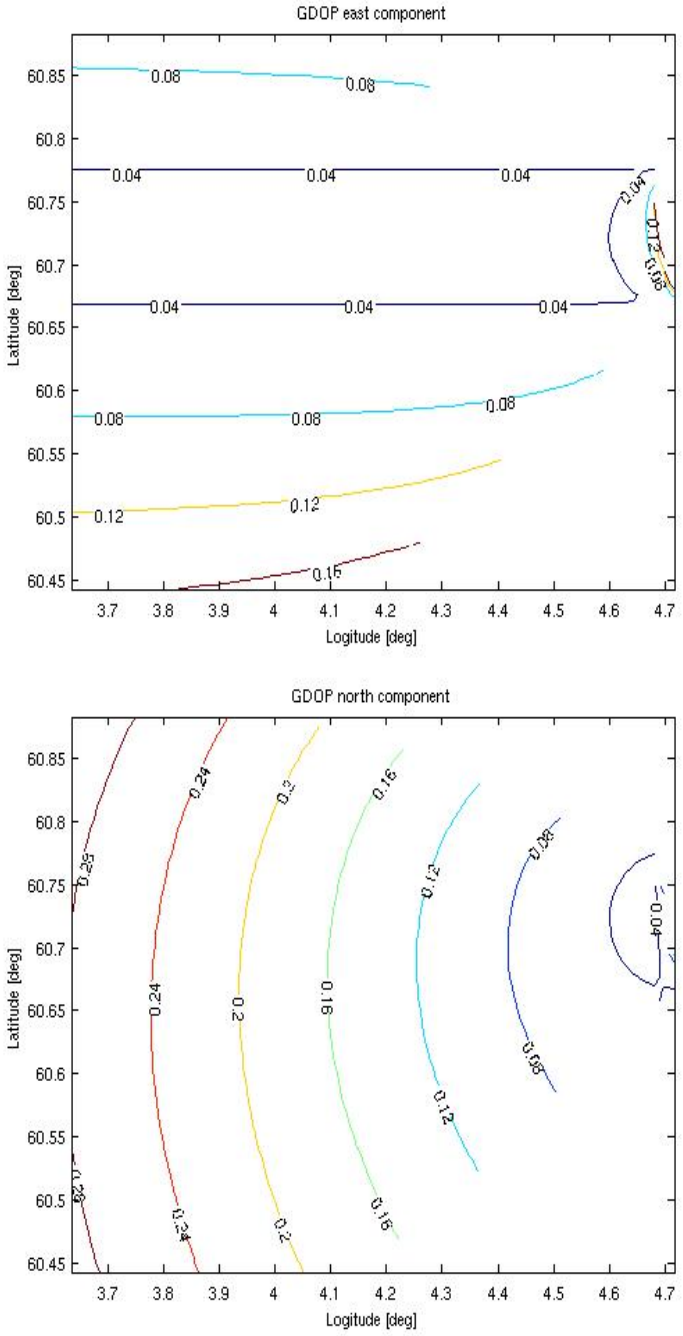

FIGURE 5.2: The geometric accuracy of the velocity (m/s) in the east component (upper panel) and the north component (lower panel)

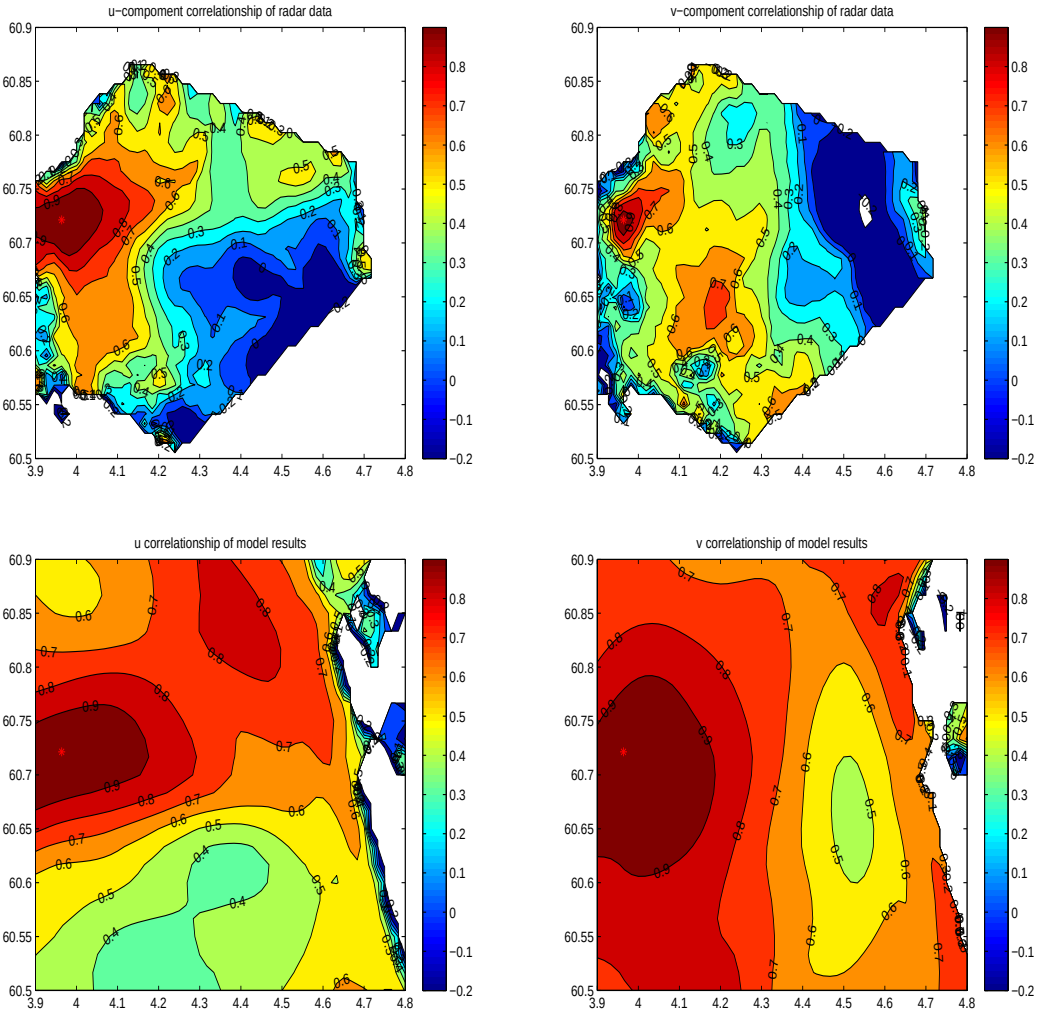

FIGURE 5.3: Averaged instantaneous correlation between the u-velocity (left panels) or v-velocity (right panels) at a specific location marked by the red-star and it at all other radar grid points (upper panels) or model grid points (lower panels).

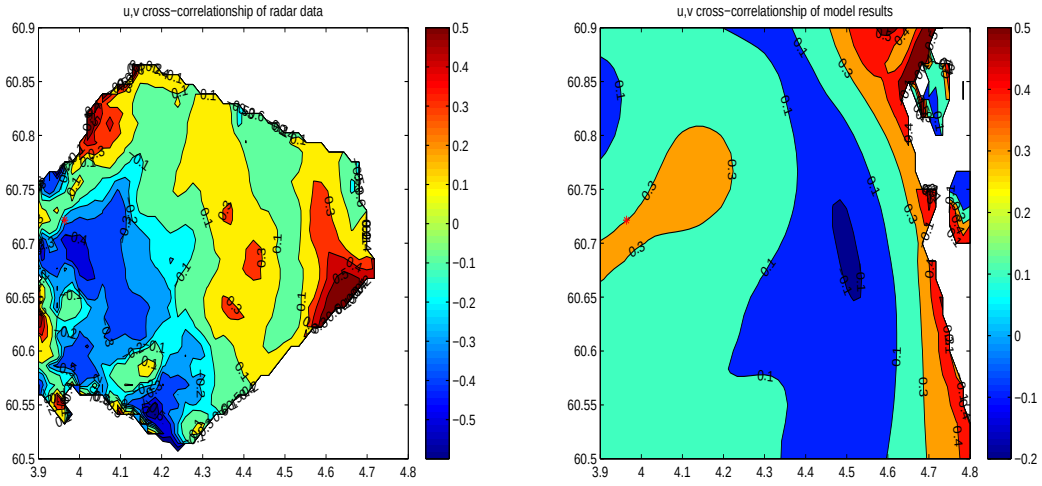

FIGURE 5.4: Cross-correlation between u-velocity at the fixed position marked by the red-star and v-velocity at all other radar grid points (left panel) or model grid points (right panel)

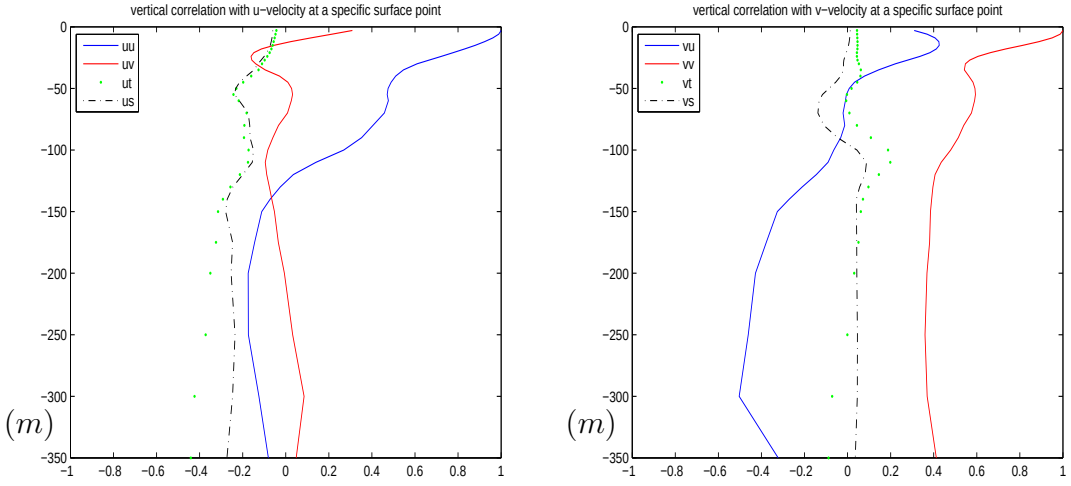

FIGURE 5.5: Vertical cross-correlation between u-velocity (left panel), v-velocity (right panel) at the fixed position of surface and variables u, v, t, s along depth.

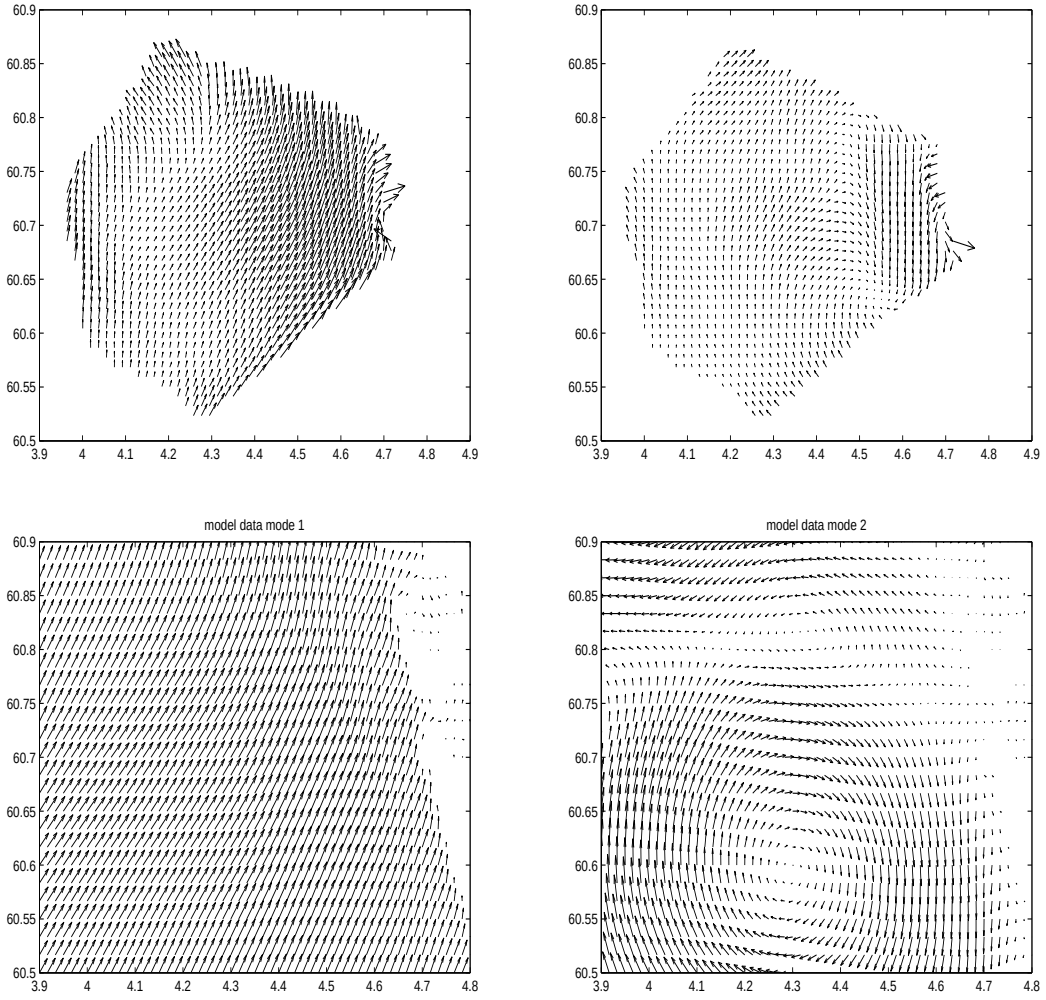

FIGURE 5.6: Mode 1 EOF (left panels) and mode 2 EOF (right panels) of the radar data (upper panels) and HAMSOM results (lower panels), respectively

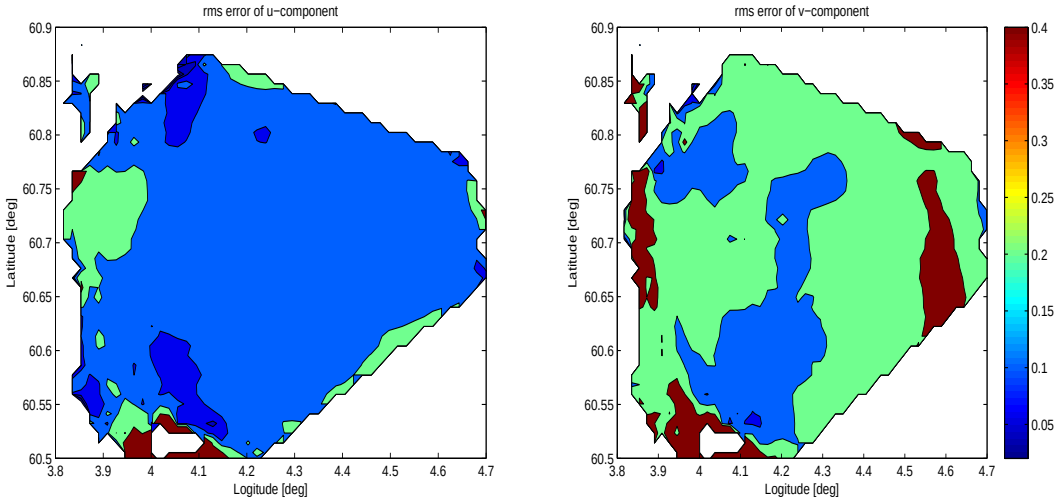

FIGURE 5.7: Spatial root-mean-square errors relative to HF radar data of u-component (left panel) and v-component (right panel)

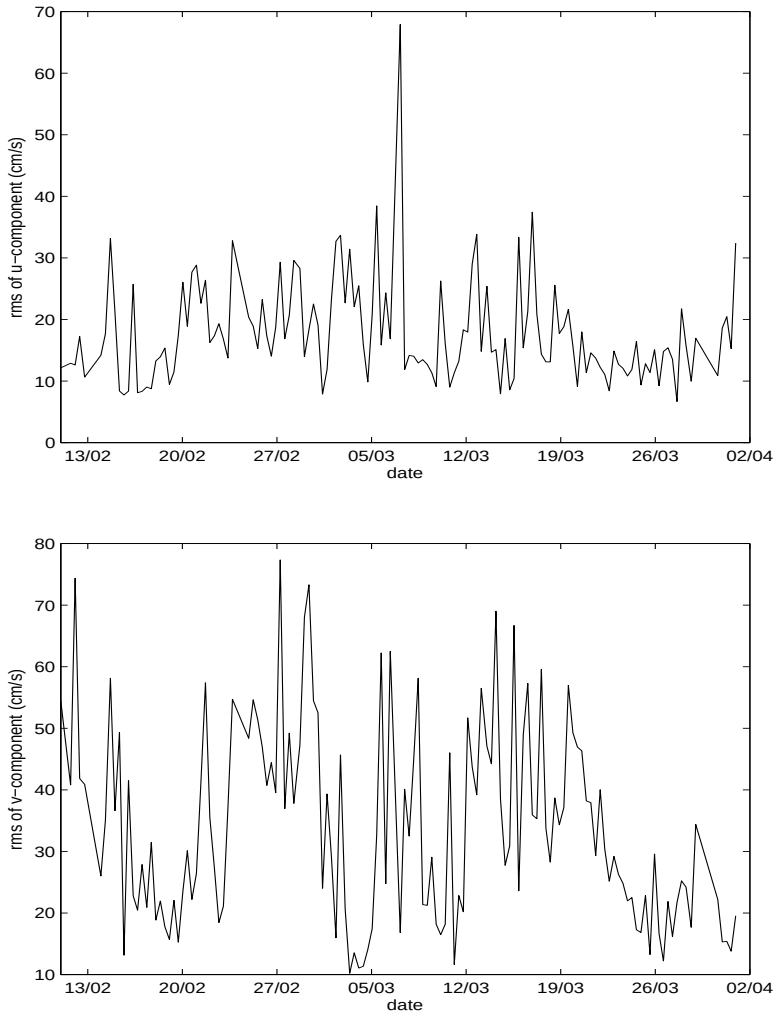

FIGURE 5.8: Spatial averaged root-mean-square errors relative to HF radar data of u-component (upper panel) and v-component (lower panel)

Chapter 6

Assimilation Implementations

In the preceding chapters, we described the complex, nonlinear, forecast shelf model and the observational data, which are two primary parts in an assimilation system. Now, we start to describe the high-frequency, real-time assimilation with our new assimilation method (QEnKF).

6.1 QEnKF vs EnKF

First of all, the comparison of assimilation with the QEnKF method and the traditional EnKF method is presented.
Three experiments are performed, one of them is without assimilation and called "Freerun", the others are performed with the traditional EnKF method and QEnKF method, called "EnKFrun" and "QEnKFrun", respectively. In both assimilation runs, the model state vectors of the analysis are composed of the sea level elevation, temperature, salinity, and two horizontal transport velocities. Only the variables at the surface are analyzed, since the radar data only represents the very shallow surface layer, and the vertical correlations between these variables are poor, that was discussed in the last chapter. Besides, all the variables of HAMSOM are calculated from the surface to the bottom. Hence, after the surface variables are updated, the vertical projection of the update can be done by the propagation of model itself.
The details of these experiments are described as follows,

- Freerun : In this experiment, no assimilation is used, so the model develops like a classical forward model (hereafter referred as the reference run).
- EnKFrun : In this experiment, the assimilation method used is the traditional EnKF method with an ensemble of 50-member coinstantaneous fields. The model time interval is 2 minutes.
- QEnKFrun: The QEnKF method is used in this experiment, and the model time interval is the same as in EnKFrun, that means the number of ensemble is equal to 10, since the observational interval is 20 minutes.

All these model simulations are initialized on January 1, 2000, and the assimilation procedure starts from February 8 till March 31, 2000. The analysis time interval is general 20 minutes. The reason we used the word "general" is because sometimes the observations do not exist, but that situation occurs not very often.

6.1.1 Preparation for the EnKFrun

As known, with the traditional EnKF assimilation method, an ensemble of model initial fields should be generated at the beginning of the assimilation procedure. However, due to the requirement that this ensemble members should represent all the possibilities of model results and the lack of knowledge about the background error of the model at the beginning of the assimilation procedure, the generation of this ensemble is arduous.
The first way we tried to generate the ensemble members is by perturbing one prior, assumed error covariance of the model variables at the beginning of the assimilation procedure, the perturbations have a normal distribution and are added to the simulated model variables in Freerun. This method is almost the same as we used for the generation of model initial states for the linear model in chapter 4. Hence, this proceeding guarantees sure that the mean of the ensemble members at the beginning of the assimilation procedure is the same as for reference run.
Fig.6.1 shows the distribution of the surface velocity field of the ensemble mean at the end of the assimilation run, which is treated as the truth in the traditional EnKF theory. By comparing it with the result of the reference run at the same moment, which is shown in Fig.6.2, it becomes clear that the meanders and eddies simulated by the reference run do not exist in this EnKFrun. The results of the assimilation with EnKF method are also much smoother than the results of the

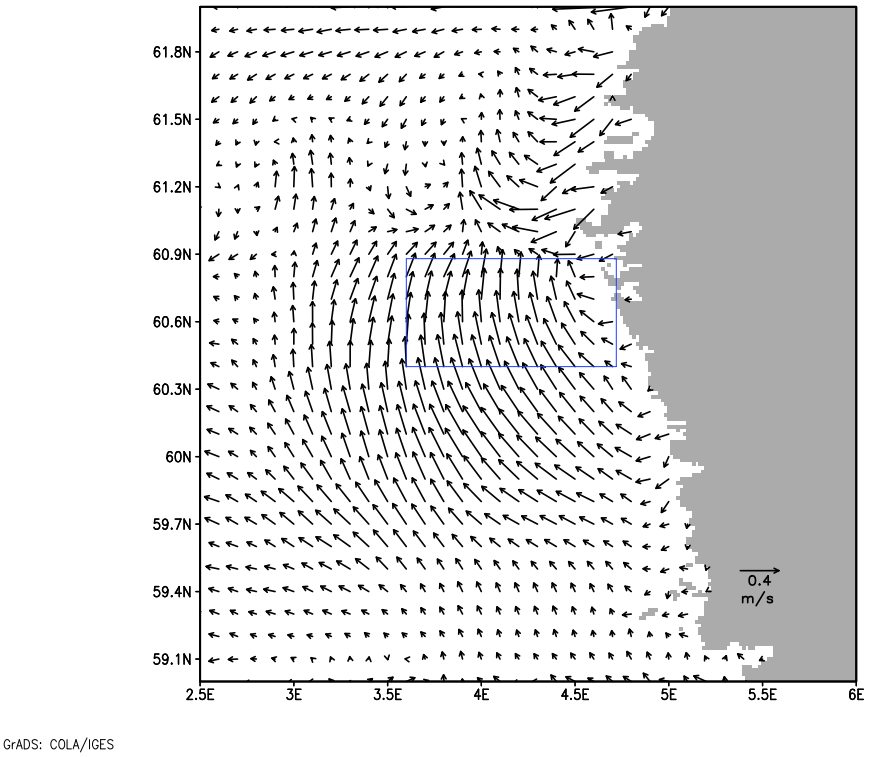

FIGURE 6.1: Surface velocity field of the first EnKFrun at 23 : 40 UTC on March 31, 2000.

reference run.

In order to compare the model results with the HF radar data, the surface current fields of the observation, reference run and EnKFrun, with zooming into the area covered by the radar (Blue rectangular area) are shown in Fig.6.3. Obviously, with these ensemble members, the result after assimilation with the EnKF method is worse than the result of the reference run, which has no similar structure as the observations nor the reference run. Hence, the generation of ensemble members is not successful. The reason for these differences is probably due to the underestimated background error covariance.

Another method we performed is by perturbing the initial fields of model run at January 1st, 2000, which is more than a month before the assimilation start. This allows to assess the propagation of ensemble errors by comparing the different ensemble members under the same model conditions. Nine points in the model domain are selected to calculate the standard deviations of the ensemble members. The coordinates of these points are (30,100,1), (30,100,10), (30,100,20), (90,100,1), (90,100,10), (90,100,20), (150,100,1), (150,100,10), (150,100,20), and the location of surface points are shown in Fig.6.4.

Fig.6.5 shows the standard deviations of the ensemble members for the u-velocity

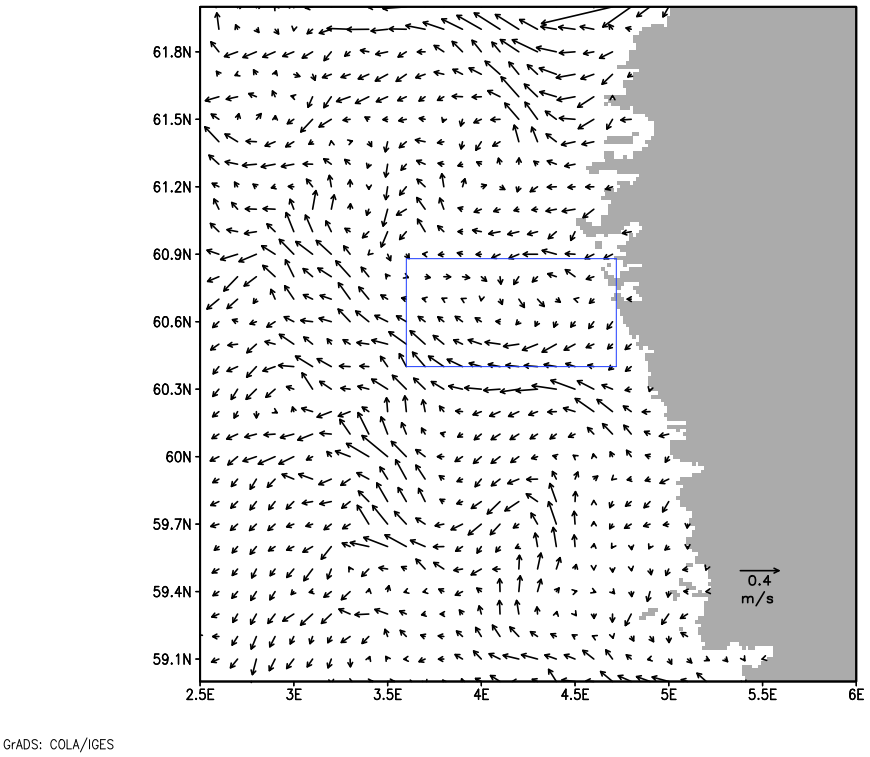

FIGURE 6.2: Surface velocity field of the reference run at 23 : 40 UTC on March 31, 2000.

(upper panel), v-velocity (middle panel) and elevation (lower panel), respectively. The pictures show that the standard deviations increase with time, and after reaching the maximum value, start to decrease. The reason of the progress is because the only difference between the ensemble members is the difference of initial temperature fields, all the other model conditions, like surface forces and boundary conditions are the same. In terms of the scale of standard deviations of the three variables, we can assume that after $22 - 23$ days, the ensemble members have the biggest standard deviations, which then can represent the model errors optimally. Hence, the second EnKFrun starts from Jan 23ird, 2000, when the initial ensemble members are generated. The standard deviations of the ensemble members are calculated again before the assimilation procedure begins to dialog the quality of the ensemble members, which are shown in Fig.6.6.

The picture shows that the standard deviations arrive at the maximum value just before the start of assimilation, that means our ensemble sampling is reasonable and successful. This method makes sure that the estimation of the error covariance represented by such an ensemble of model states is correct.

With these ensemble members, assimilation with the traditional EnKF method is implemented again, and Fig.6.7 shows the surface velocity field of ensemble mean

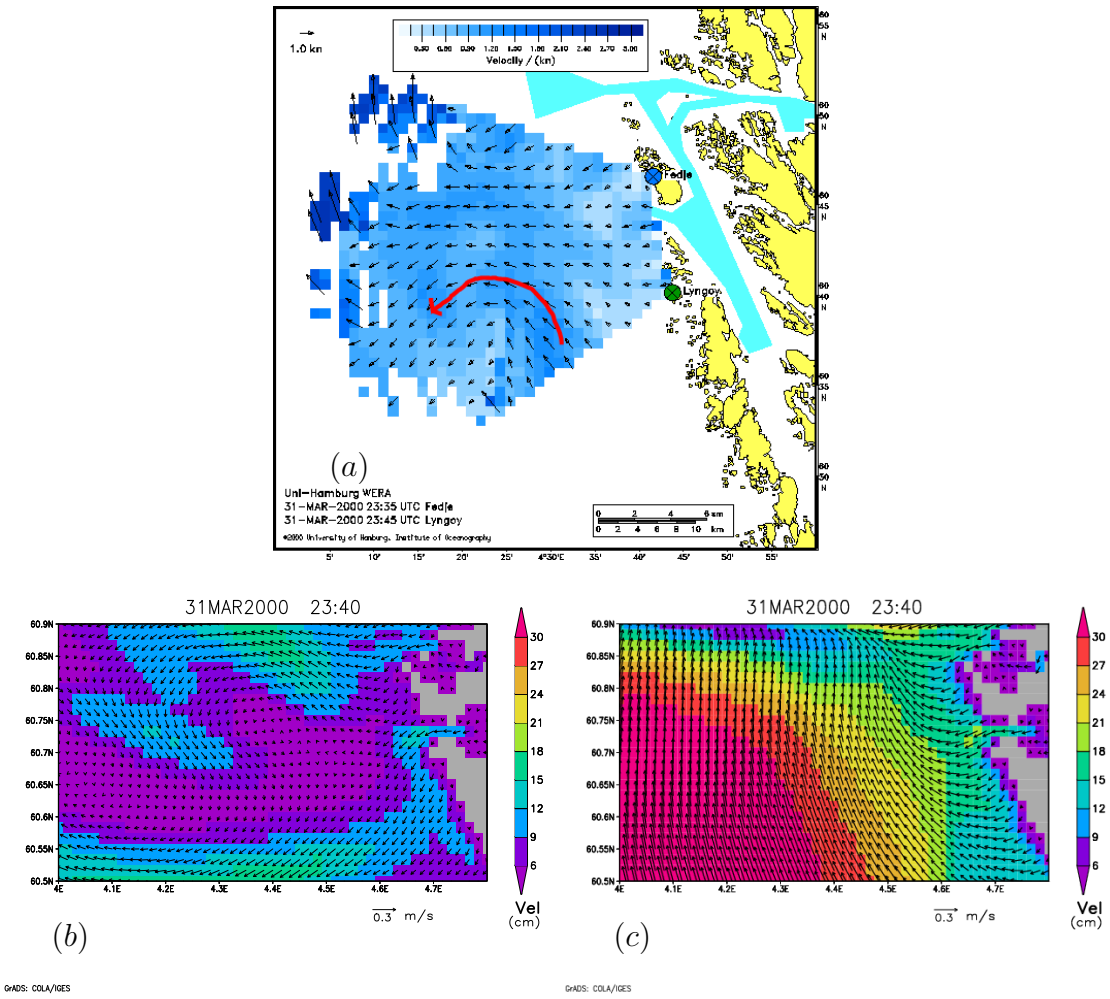

FIGURE 6.3: Surface current fields zoomed into the area covered by the HF radar. Radar data(a), Freerun(b), EnKFrun(c), respectively, at 23 : 40 UTC on March 31, 2000

at the end of this assimilation run, and the counterpart of the first EnKFrun is shown in Fig.6.1. By comparing them with the result of the reference run, we find that some meanders and eddies appear again in the second EnKFrun, but the result is still smoother than in the reference run, and the magnitude of the velocity is a little bit smaller. The analysis with the traditional EnKF method is based on the assumption that the correct error covariances are used. However, the choice of the covariances is always a hypothesis. If the error covariances are wrong, it is hard to get expected assimilation results.

Hence, in order to assess the quality of assimilations with the traditional EnKF method, the root-mean-square (RMS) errors of both the $u-$ and $v-$ components in these two assimilation runs and the reference run relative to the HF radar data are computed in the observational area, which is shown in Fig.6.8. The picture indicate that the RMS errors of both components in the second EnKFrun are much

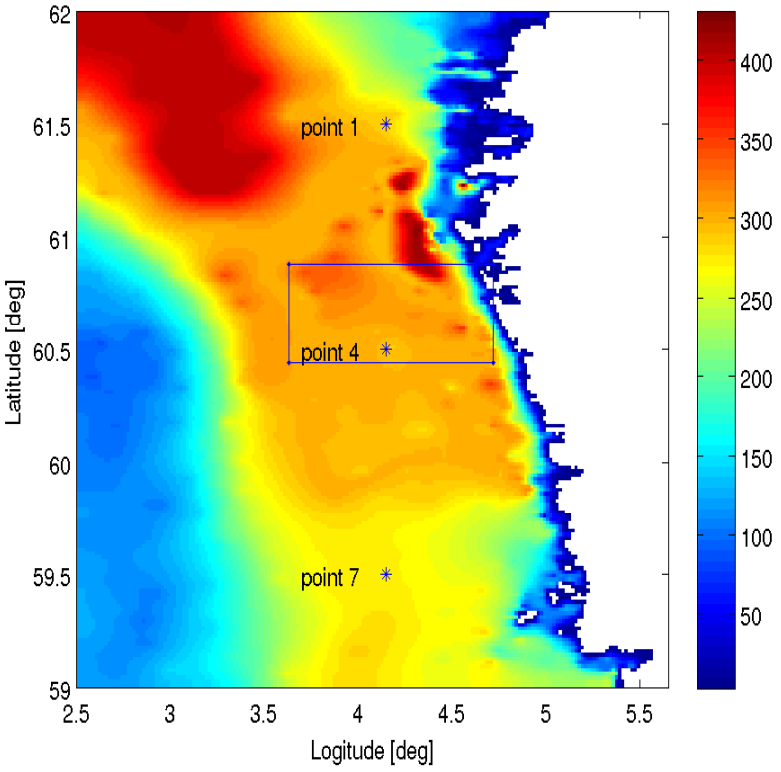

FIGURE 6.4: The locations of selected points at surface.

smaller than in the first EnKFrun. Besides, in most of the cases, the RMS errors of both components in the second EnKFrun are a little bit smaller than in the reference run, and the tendency is to decrease with time, that means our second EnKFrun is acceptable. The comparison of RMS errors of the u-velocity and v-velocity indicates that the correction of the former variable is bigger than that of the latter variable. Since in the radar data, the accuracy of the u-component is much smaller than that of the v-component, which is related to the error covariance of the observations.

6.1.2 Comparison of Surface Currents

However, the prior or assumed error covariance of the model run needs not be prepared with our QEnKF method, since the model errors are substituted by the forecast tendencies. Hence, the preparation for the QEnKFrun is avoided. The distribution of surface velocity field of this assimilation run at the end is shown in Fig.6.9. By comparing it with the reference run and the second EnKFrun, the eddies in the reference run are mostly kept.

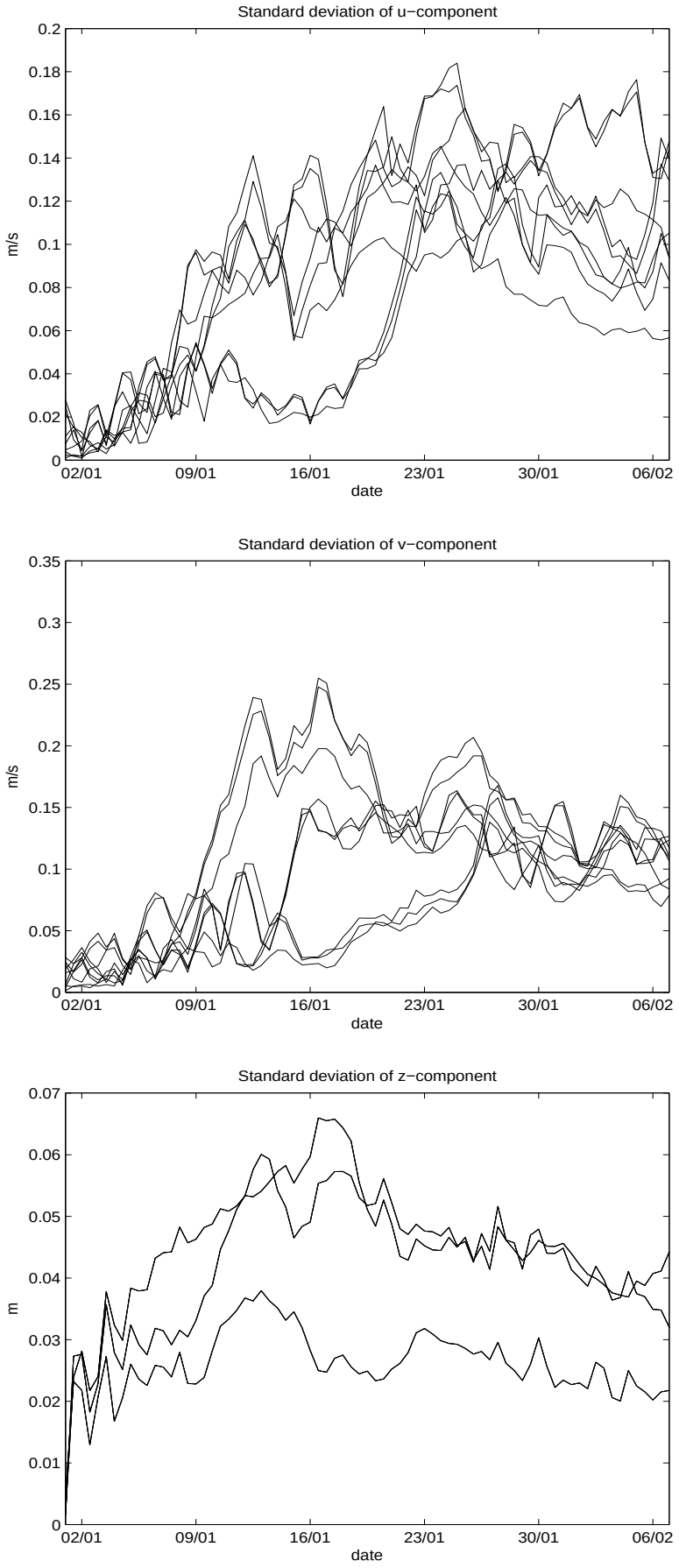

FIGURE 6.5: The standard deviations of ensemble members for u-velocity (upper panel), v-velocity (middle panel) and zeta (lower panel), respectively.

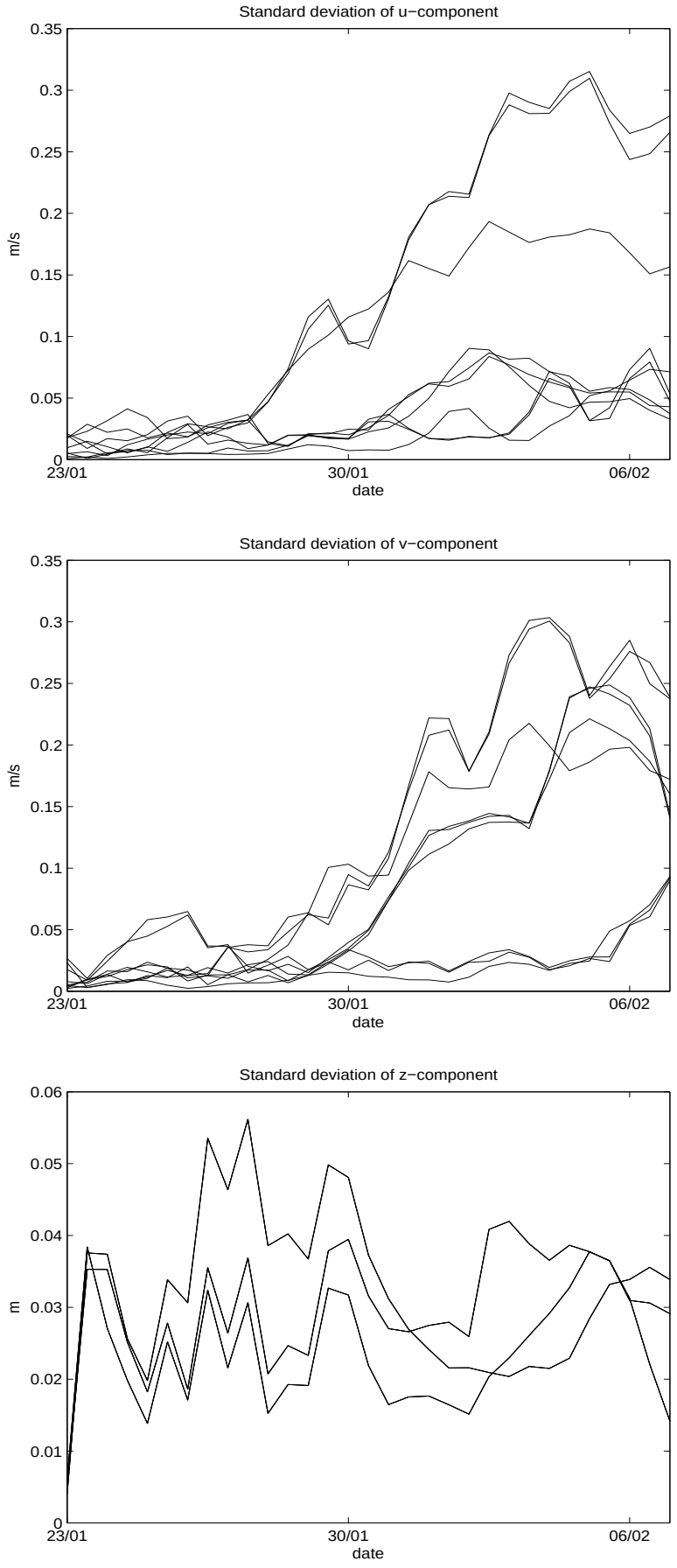

FIGURE 6.6: The standard deviations of ensemble members for u-velocity (upper panel), v-velocity (middle panel) and zeta (lower panel), respectively.

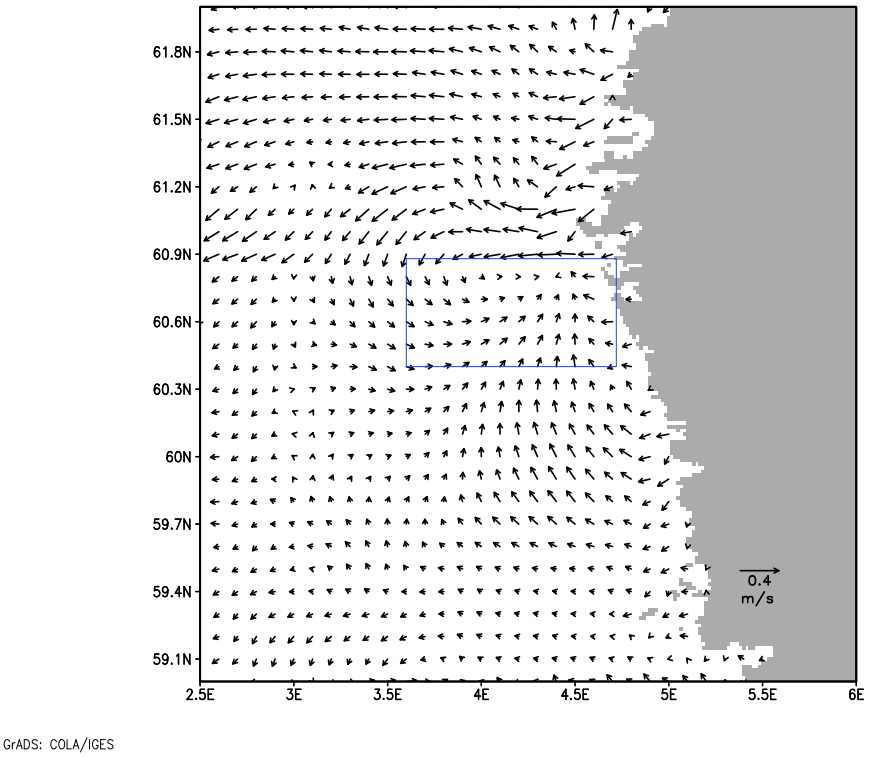

FIGURE 6.7: Surface velocity field of the second EnKFrun at 23 : 40 UTC on March 31, 2000.

First of all, the velocity corrections by the HF radar assimilation with the traditional EnKF method and the QEnKF method are presented in Fig.6.10, which gives the velocity differences between the reference run and assimilated run averaged over the whole assimilation procedure. The differences (increments) of both assimilated runs are most obvious in the HF radar coverage (rectangular area). Besides, the comparisons of the two panels of this figure indicate that the improvement of these two assimilation methods is similar, and a little bit larger with the QEnKF method.

To compare our QEnKF method with the traditional EnKF method, the surface current fields at the last moment of these two assimilation runs with zooming into the HF radar area are shown in Fig.6.11 (c, d). In panels (a) and (b) of this figure the surface current fields of radar data and the reference run are shown. First of all, comparing panel (a) (radar data) and panel (b) (reference run) of this figure, we find that our model results already agree considerably with the radar data. But, obviously there is big difference in the center of the radar area, which is marked with a big arrow in panel (a). Comparing the result of $EnKFrun$ (panel (c)) with

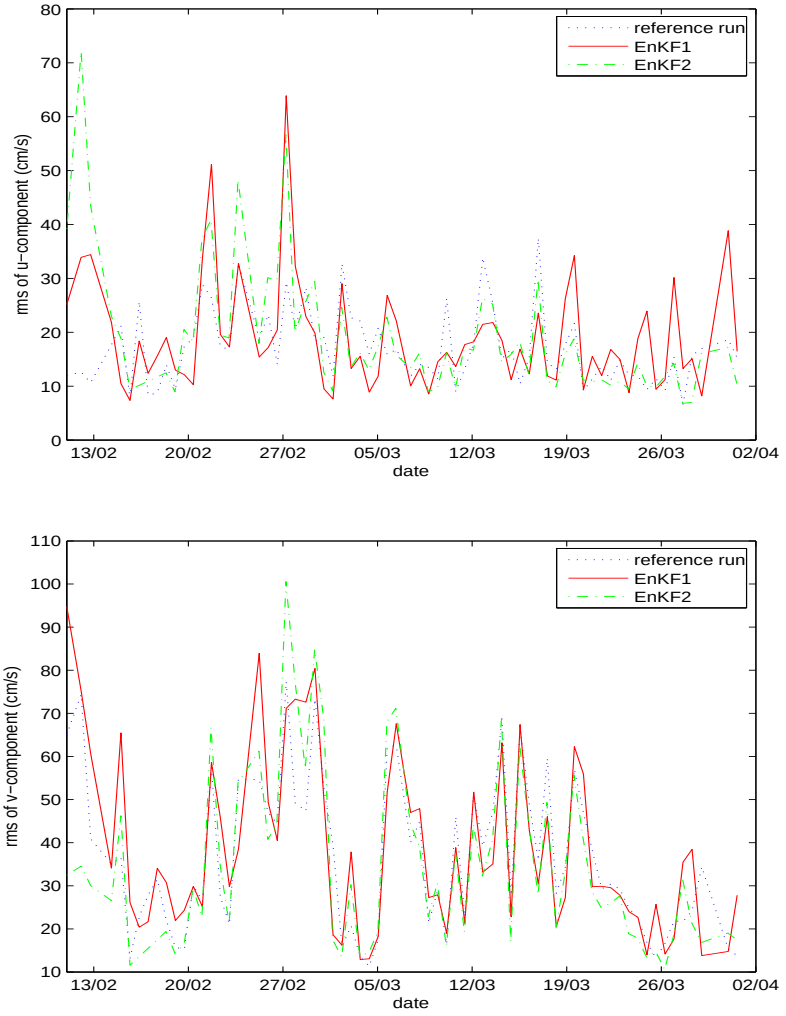

FIGURE 6.8: Root-mean-square errors of u-component (upper panel) and v-component (lower panel) relative to HF-radar data, in the reference run (dotted line), the first EnKFrun (solid line) and the second EnKFrun (dash-dotted line).

radar data (panel (a)), no obvious improvement can be found in the EnKFrun. Besides, compared to $Freerun$ in panel (b), we find that the results of $EnKFrun$ are relatively smooth. Since these results are the mean of an ensemble of 50 model runs, it is reasonable. However, it is far from what we expected. The result of experiment $QEnKF$ is shown in panel (d), comparing it with panel (a) and (b), we can conclude that our new assimilation method gives an obvious improvement and forces the surface velocity structure to agree better with the radar data, since the structure marked with the big arrow appears again in panel (d).

At another arbitrary time (the same issue as in Fig.6.11 is shown in Fig.6.12), the same conclusions can also be reached.

In order to find the reason that the traditional EnKF does not show a reasonable

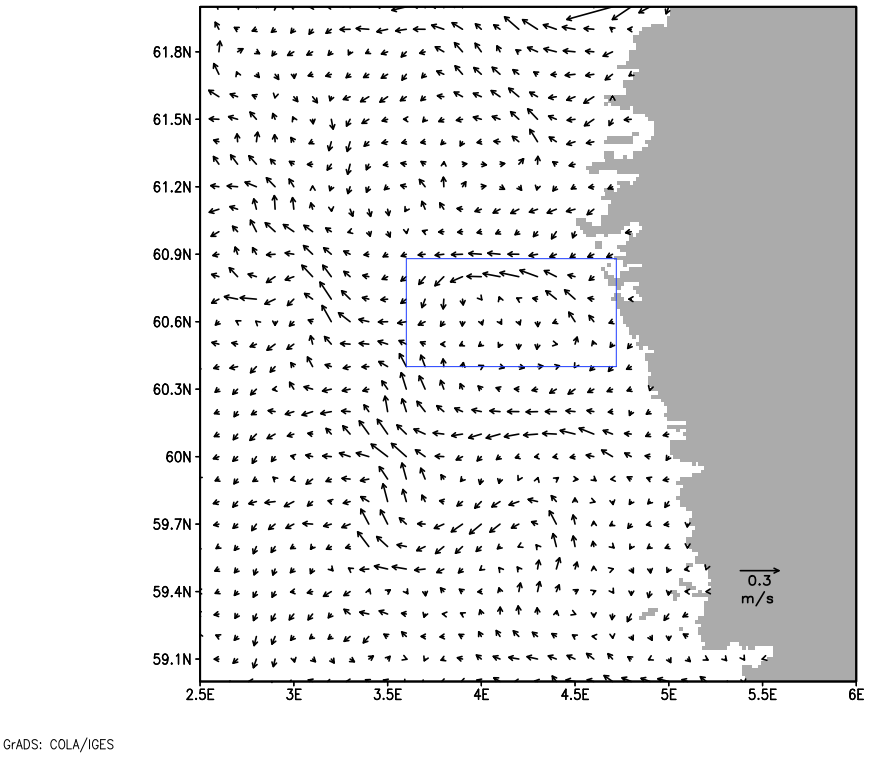

FIGURE 6.9: Surface velocity field of the QEnKFrun at 23 : 40 UTC on March 31, 2000

result at the end of the assimilation procedure, we go back to the beginning of the procedure. Fig.6.13 shows the surface current fields of the radar data (panel (a)), the QEnKFrun (panel (b)) and EnKFrun (panel (c)) at 23 : 40 on Feb 18, which is 10 days after the assimilation starts. From this figure, we observe that the traditional EnKF method gives the similar current structures as the observations, and even a little better than ones of the QEnKF method. Besides, the result of EnKFrun at this moment is not as smooth as at the end of the assimilation. Hence, we conclude that a divergence happens after a long-term assimilation in the EnKFrun. That can be explained, since the ensemble is determined by the background error estimated at the beginning. In another word, the state space described by such ensemble is decided at the very beginning. However, the EnKF seeks an analysis to minimize the posterior variance (see equation 2.7). Hence, after a long-term high-frequency assimilation, the posterior variance keeps decreasing, a divergence will happen that means the analysis will ignore the observations and the mean of the ensemble members reach more and more smooth pattern.

It is interesting to note, that both systems (EnKF and QEnKF) use the same equations and algorithms, only different ensembles were chosen. That demonstrates that, except the divergence, on the other hand, the estimates of the model

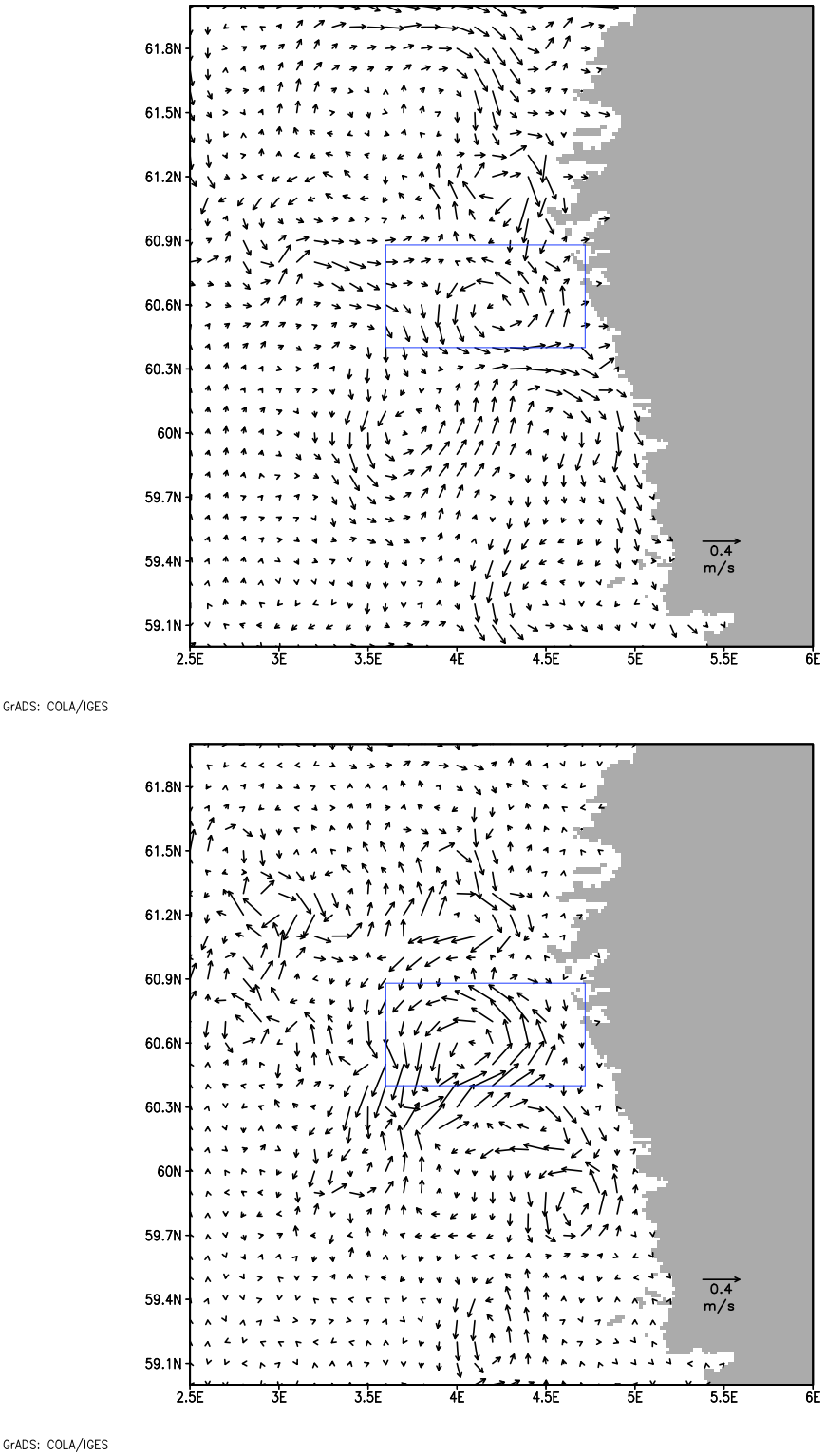

FIGURE 6.10: Averaged velocity corrections of EnKFrun (upper panel) and QEnKFrun (lower panel)

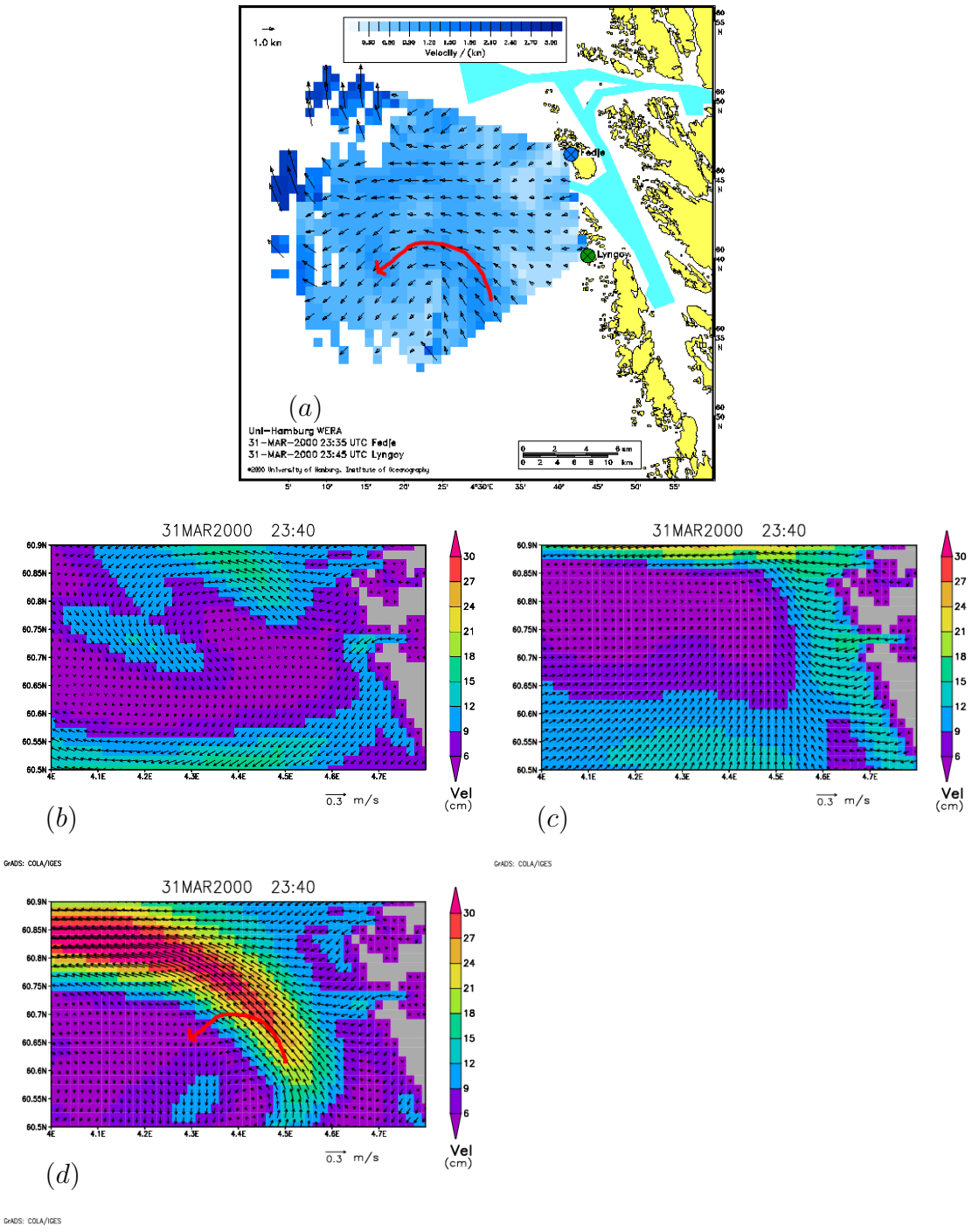

FIGURE 6.11: Surface current fields zoomed into the area covered by the HF radar. Radar data(a), Freerun(b), EnKFrun(c), QEnKFrun(d), respectively, at 23 : 40 UTC on March 31, 2000

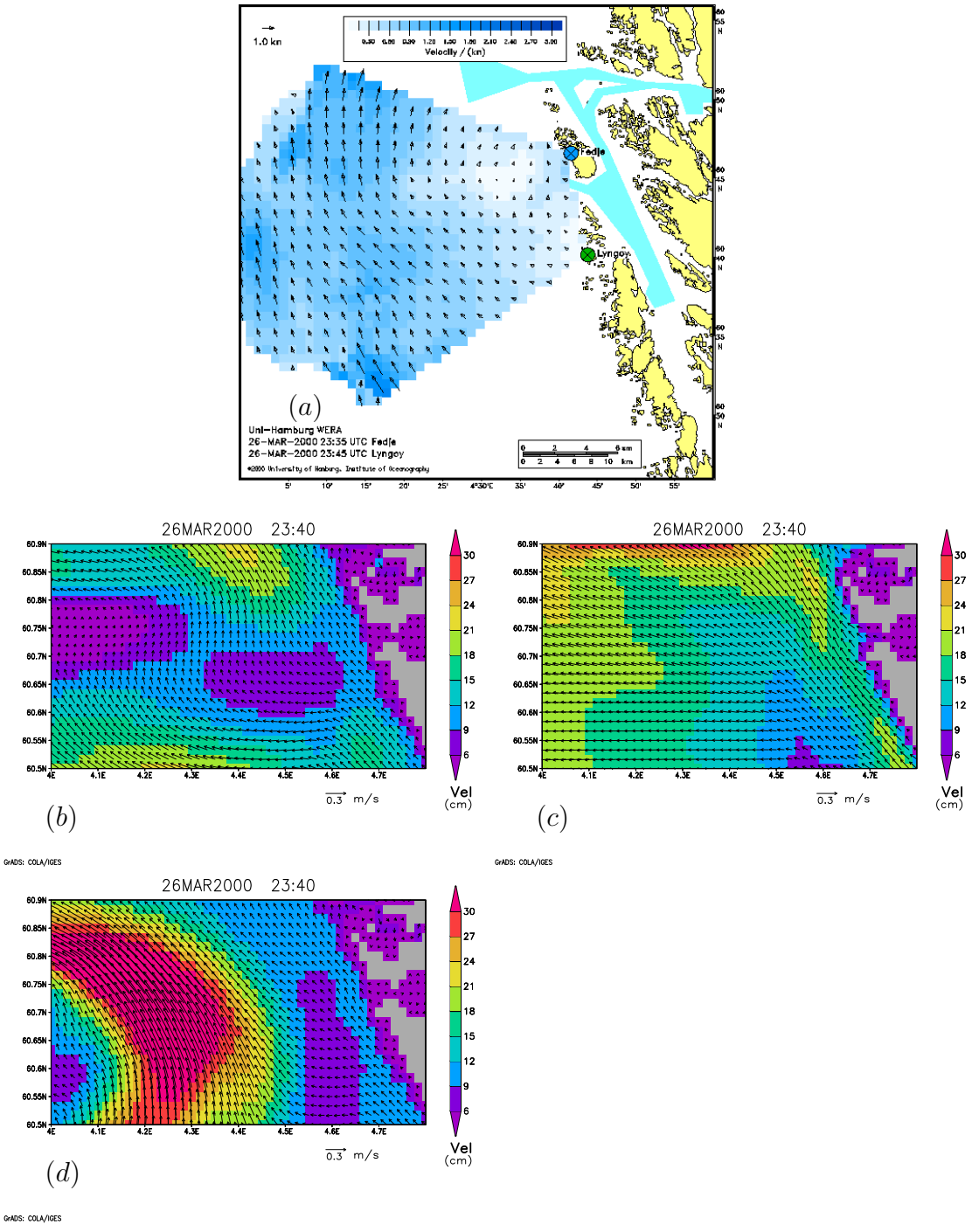

FIGURE 6.12: Surface current fields zoomed into the area covered by the HF-radar. Radar data(a), Freerun(b), EnKFrun(c), QEnKFrun(d), respectively, at 23 : 40 UTC on March 26, 2000

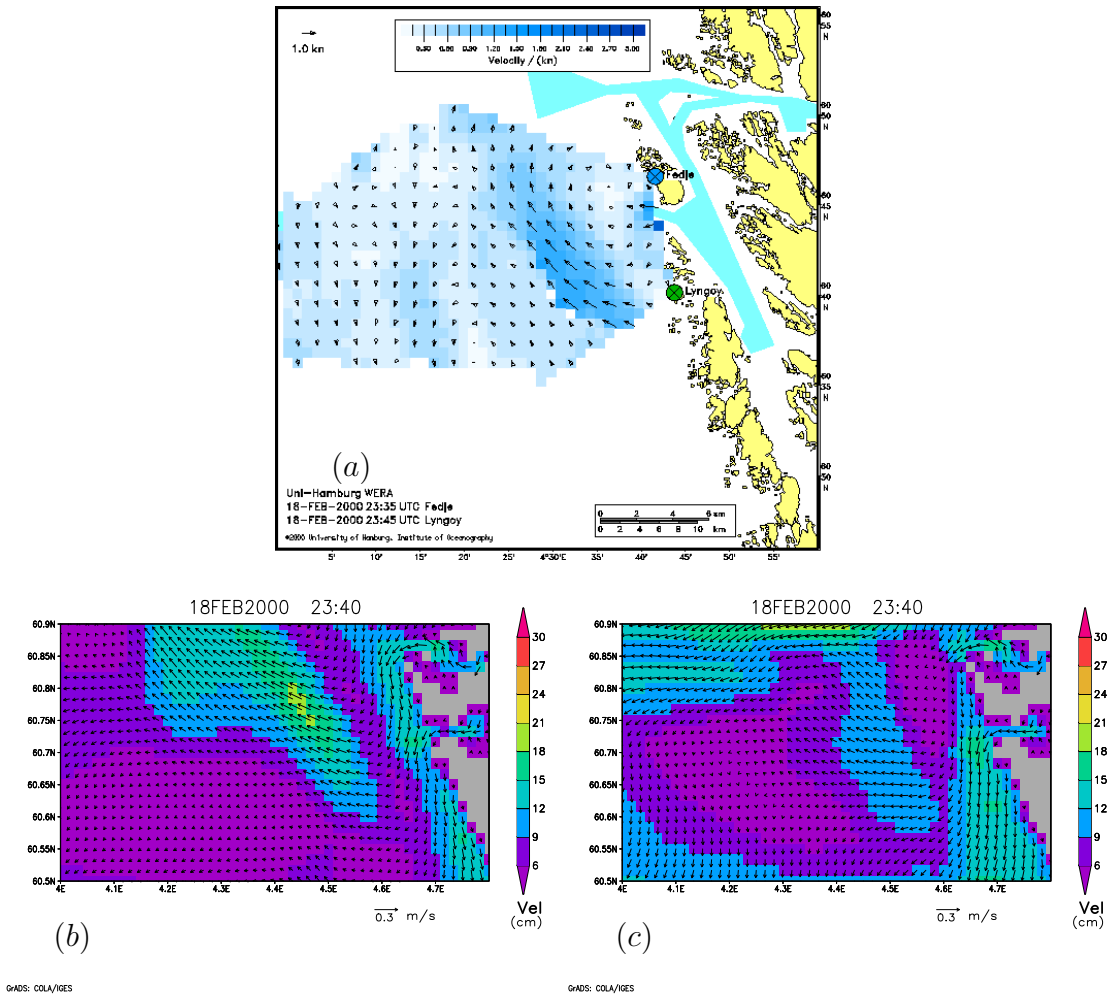

FIGURE 6.13: Surface current fields zoomed into the area covered by the HF radar. Radar data(a), QEnKFrun(b), EnKFrun(c), respectively, at 23 : 40 UTC on February 18, 2000

error are essentially crucial in assimilation systems. Most of the model errors are systematic, hence not well represented by random noise, even the random noise have already been propagated for enough time by the model. However, in the QEnKF system, the forecast tendencies are collected to represent the model forecast errors, which by this way are flow-dependent, systematic and more realistic. Hence, the results with this method are significantly improved.

The root-mean-square (RMS) error of the three experiments relative to the HF-radar data is computed in the observational space, meaning that the model currents are interpolated to the location of the observations. Fig.6.14 gives respective RMS time series of the u-component (left panel) and v-component (right panel). The pictures also show the RMS errors of QEnKFrun are slightly smaller than of Freerun, especially when they are relatively large in the latter run in most of the cases. In another word, when the model results of Freerun have a big difference

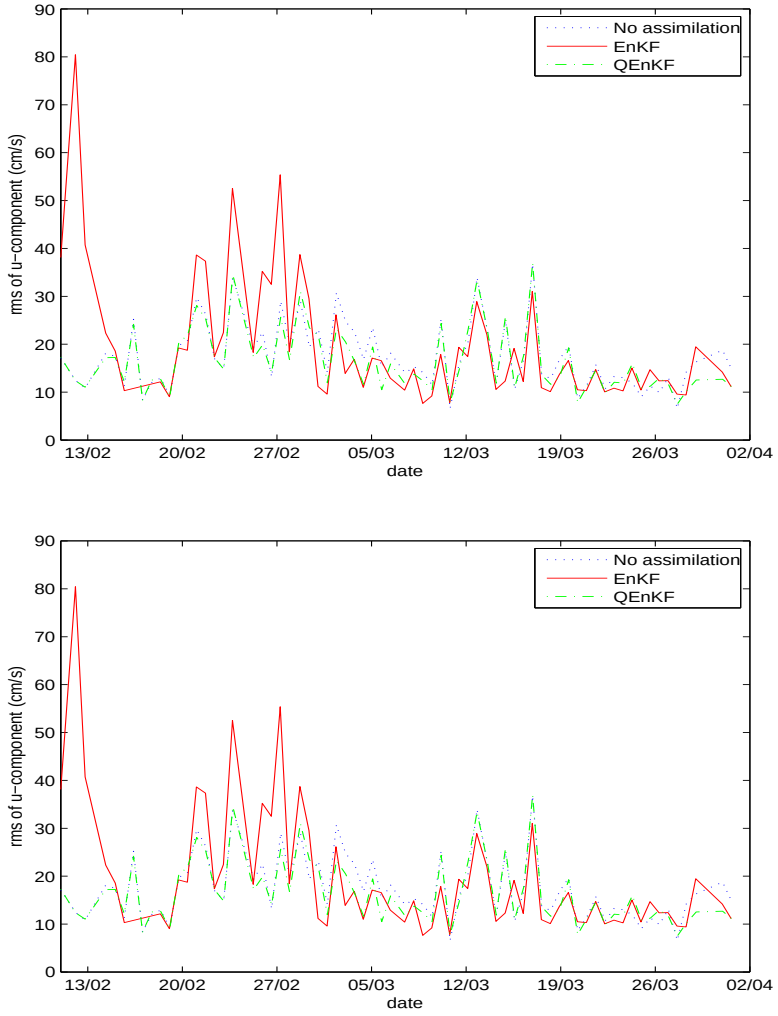

FIGURE 6.14: Root-mean-square errors of u-component (upper panel) and v-component (lower panel) relative to HF-radar data, in the reference run (dotted line), EnKFrun (solid line) and QEnKFrun (dash-dotted line).

from the radar data, the correction by the assimilation is much more larger. Moreover, both panels also demonstrate the RMS errors of EnKFrun are much larger than that of QEnKFrun.

6.1.3 Comparison of Temperature

In the assimilation analysis, temperature and salinity are also included since they are expected to be closely related to the currents in a baroclinic model.

Fig.6.15 gives the surface temperature distribution of the reference run, Freerun and QEnKFrun at the same day, respectively. These pictures indicate that the

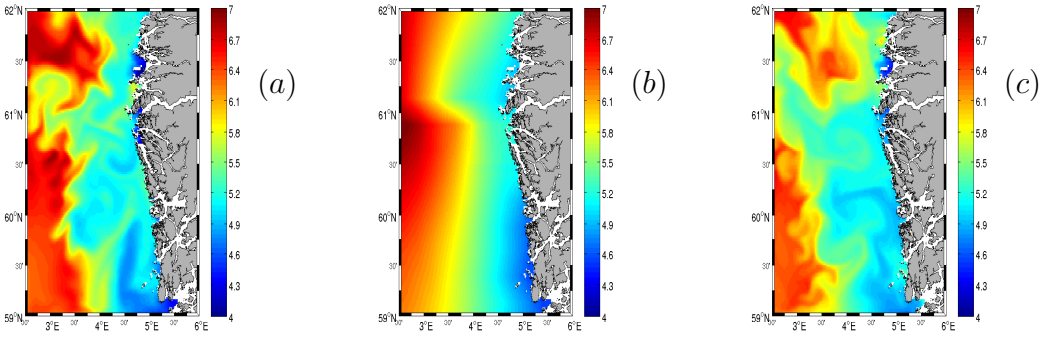

FIGURE 6.15: Surface temperature fields of Freerun (a), EnKFrun (b) and QEnKFrun (c), respectively on March 31, 2000.

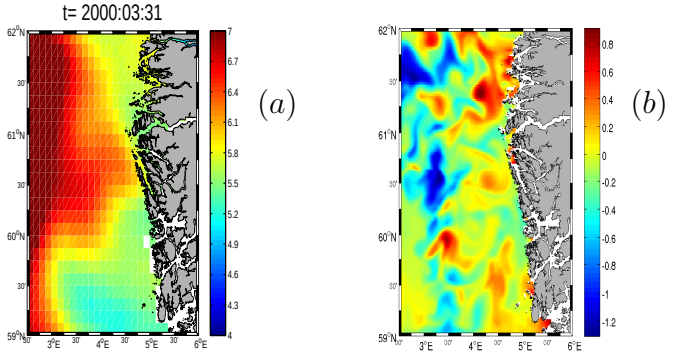

FIGURE 6.16: Surface temperature field of MODAS (a), and the updated temperature field of QEnKFrun (b) on March 31, 2000.

temperature field in the EnKFrun (panel (b)) is much smoother than in the reference run (panel (a)). However, most of the temperature structures are kept in the QEnKFrun (panel (c)). In order to validate the update of temperature by assimilation, the Modular Ocean Data Assimilation System (MODAS) (Kara and Barron, 2007) data is adopted, which is independent of the model results. Fig.6.16 gives the surface temperature field of the MODAS data (panel (a)) and the update of temperature fields (difference between assimilation and reference run) of QEnKFrun (panel (b)). The comparison of temperature fields of MODAS data and the reference run (panel (a) in Fig.6.15) shows that the distributions of them do not agree well with each other, in particular in areas with fronts, the temperatures in the latter are lower than in the former along the coast. However, the update of temperature field indicates that the temperature increases due to the assimilation. Despite the fact that the radar data only cover the center of our model domain, the temperature is modified in the entire model area. That means the correlationship of temperature at different locations is higher than those of the currents.

6.1.4 Conclusions of Comparisons

To give a general impression of the our assimilation method compared to the traditional EnKF, two experiments with both methods are presented. The results indicate that the newly developed method is superior to the latter method. One of the reasons is that most of the model errors are systematic, hence are not well represented by random noise, as assumed in the EnKF method. In contrast, in the QEnKF system, the forecast tendencies are flow-dependent and describe the conditions of the actual situation when the HF-data are obtained, which can be expected to give more realistic results, since the described model forecast errors are more realistic.
The experiments demonstrate that our real-time assimilation method also modifies the distribution of temperature and salinity. Despite the fact that the radar data only cover the center of our model domain, the temperature is modified in the entire model area.

6.2 Detection of Observation Density

As mentioned before, the spatial resolution of the radar data is $1km$, which is comparable to our model spatial resolution. However, by randomly neglecting observations, how will the assimilation perform? With this variation of the observational density, three sibling experiments are conducted, and compared to the reference run.

- Freerun : is the reference run, which is already described before.
- S100: QEnKF method is used in this experiment, which is as the same as QEnKFrun, hereafter referred as the standard assimilated run. In this experiment, all of the available observational data are used.
- S80 : The same method and setup as in $S100$ run but with only 80% observations.
- S50 : The same method and setup as in $S100$ run but with only 50% observations.

Table 6.1: RMS Errors (cm/s)

Experiment	u (Mar26)	v (Mar26)	u (Mar31)	v (Mar31)
S100	12.45	15.43	26.14	23.69
S80	13.73	16.13	28.31	24.33
S50	11.80	18.66	30.34	26.55
Reference run	13.02	25.24	34.13	26.62

6.2.1 Variation of Updated Surface Currents

First and foremost, the comparison of velocity fields with the variation of the observational density is presented. Fig.6.17 and Fig.6.18 show surface current fields zoomed into the radar area of those four experiments at two arbitrary times, which are 23 : 40 on Mar 26, and Mar 31, respectively. From the first picture, it is easily to see that the velocity corrections by the assimilation decrease with the number of observations decreasing. In the second picture, obviously an eddy exists in the reference run and the observation (shown in Fig.6.3(a)). However, the location, magnitude and structure of this eddy are different between the reference run and the radar data. The corrections due to the assimilation in these experiments are not easy to determine. Considering the part marked by the big, red arrow in Fig.6.18 (b), it is still obvious to observe that the effect by assimilation decreases with less amount of observations. When only 50% of observations are used, the effect of assimilation has decreased significantly, and the background field (result of reference run) plays an increasing role in the assimilation. That can explain the big difference in velocity at the bottom left of panel (d), since where the directions of velocity are opposite in the reference run and in the radar data, then, with the amount of observations decreasing, the corrections by asimilation are largely reduced.

To assess the changes caused by the assimilation over time, we calculate the RMS errors of these three experiments relative to the HF radar data, which are shown in Fig.6.19. It seems that there are no big differences between assimilation runs, that is because the corrections by assimilation do not only include the magnitude of velocity, but also the direction. Besides, the observations are randomly discarded, that means some data with high accuracy may be dumped too. Hence, the effects of assimilation do not linearly decrease, instead, sometimes, the results with less observations may be better. Nevertheless, the RMS errors are listed in the Table 6.1 at the two dates, when the surface velocity fields are shown.

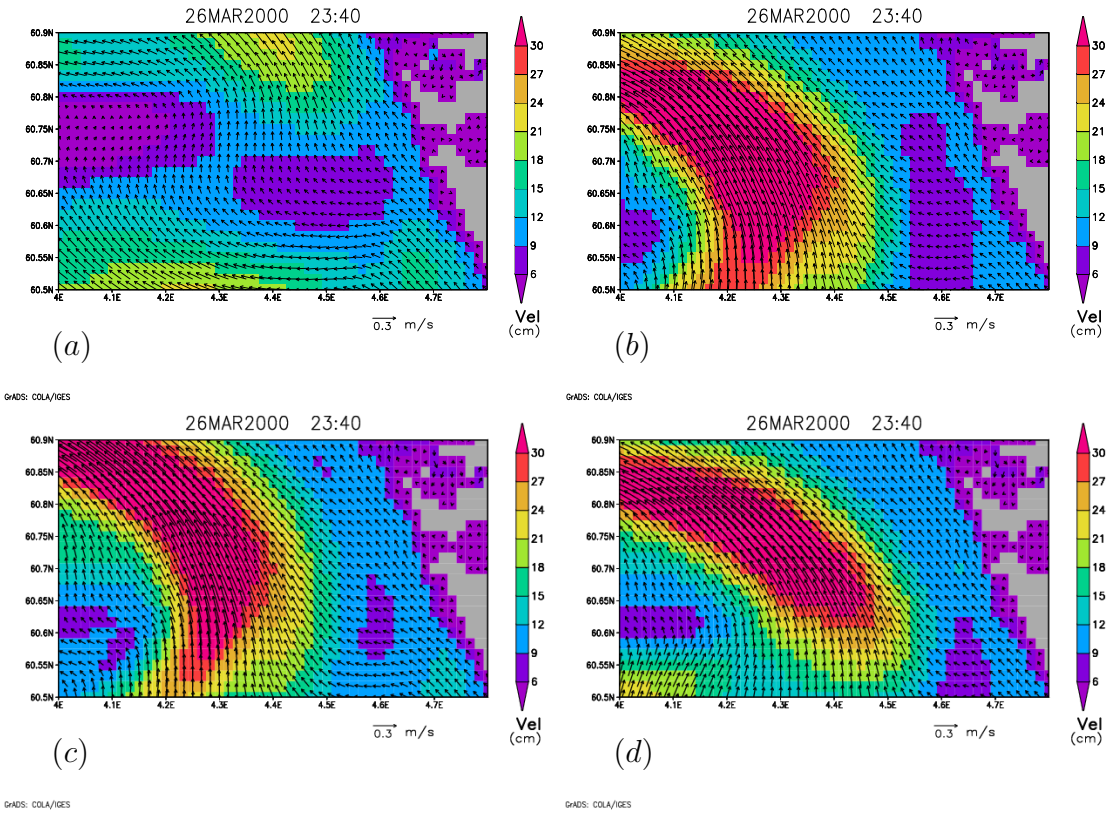

FIGURE 6.17: Surface current fields zoomed into the area covered by the HF radar for Freerun(a), $S100$(b), $S80$(c), $S50$(d), respectively, at $23:40$ UTC on March 26, 2000

The spatial structure of the RMS errors in the HF-radar area are calculated by averaging them over time, they are shown in Fig.6.20. The upper four panels of this figure represent the RMS errors for u-component, and the lower four panels for the v-component. The pictures clearly show that as the amount of observations decreases, the RMS errors increase. These changes are more obvious in the center of the radar area, and especially obvious for the u-component. As mentioned, the spatial resolution of the radar data is 1km. When half of the data are discarded, the resolution of the radar data almost changes to 2 km. Hence, comparing it with our model spatial resolution, 1 minute, it is slightly coarser.

6.2.2 Variation of Updated Temperature

As we mentioned before, the correlation between temperature and velocity is weak, even so, we are still interested in the fact, how the update of temperature will

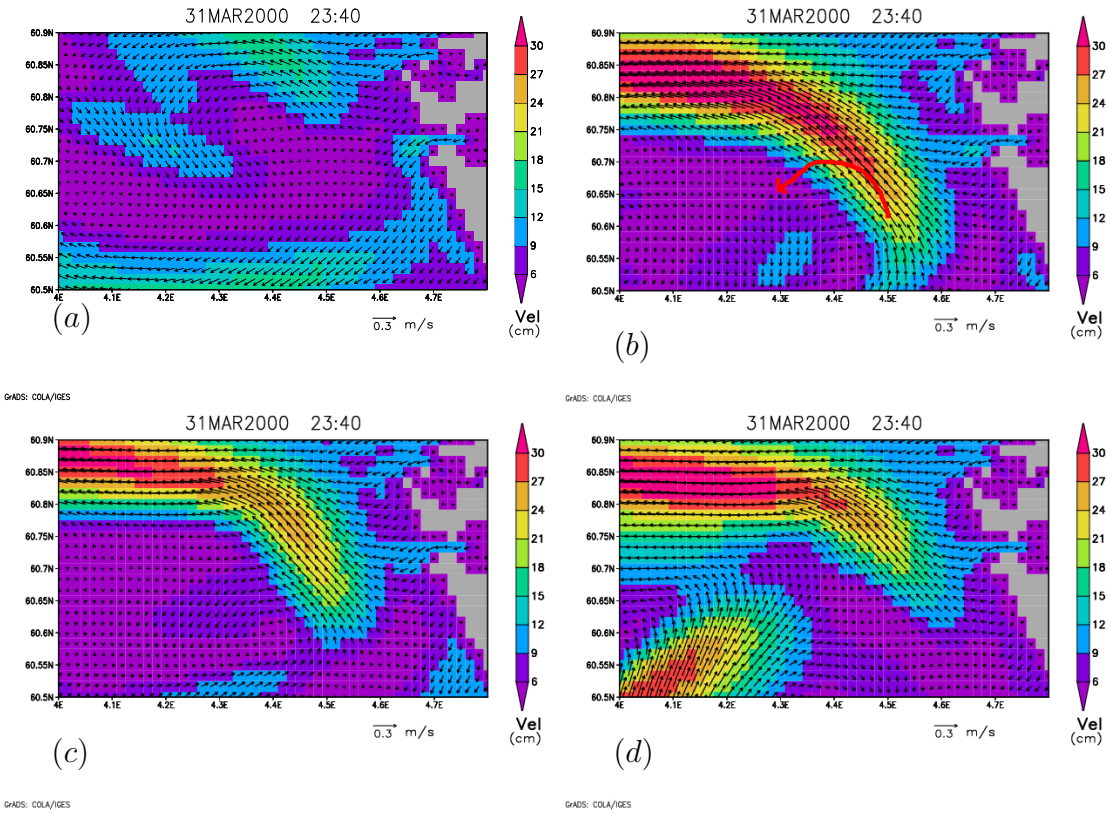

FIGURE 6.18: Surface current fields zoomed into the area covered by the HF radar for Freerun(a), $S100$(b), $S80$(c), $S50$(d), respectively, at 23 : 40 UTC on March 31, 2000

behave, when the density of velocity observations changes. Fig.6.21 gives the surface distributions of temperature for experiment *Freerun* (a), $S100$ (b), $S80$(c), $S50$(d), respectively, on March 31, 2000. The same issue at another arbitrary time, March 15, is shown in Fig.6.22. However, there are no big differences between experiment $S100$ (a), $S80$ (b) and $S50$ (c) in both figures, except for a little differences in the HF-radar area. But there are obvious differences between assimilation runs and reference run. By treating the result of the reference run as the background, 9 points located at the same positions as we described in section 6.1.1 are selected to detect the update of temperature in the assimilation runs. Fig.6.23 shows the temperature differences (assimilation value minus background) of each point in these three assimilation runs, with the red line, black line, and green line, represent experiment $S100$, $S80$ and $S50$, respectively. The first row of panels show the results of the northern points, the second row shows the central points, and the last row shows the southern points. Besides, from the left to the right panels, the order of points changes from the surface to bottom. All panels show there are only slightly small differences between the different assimilation

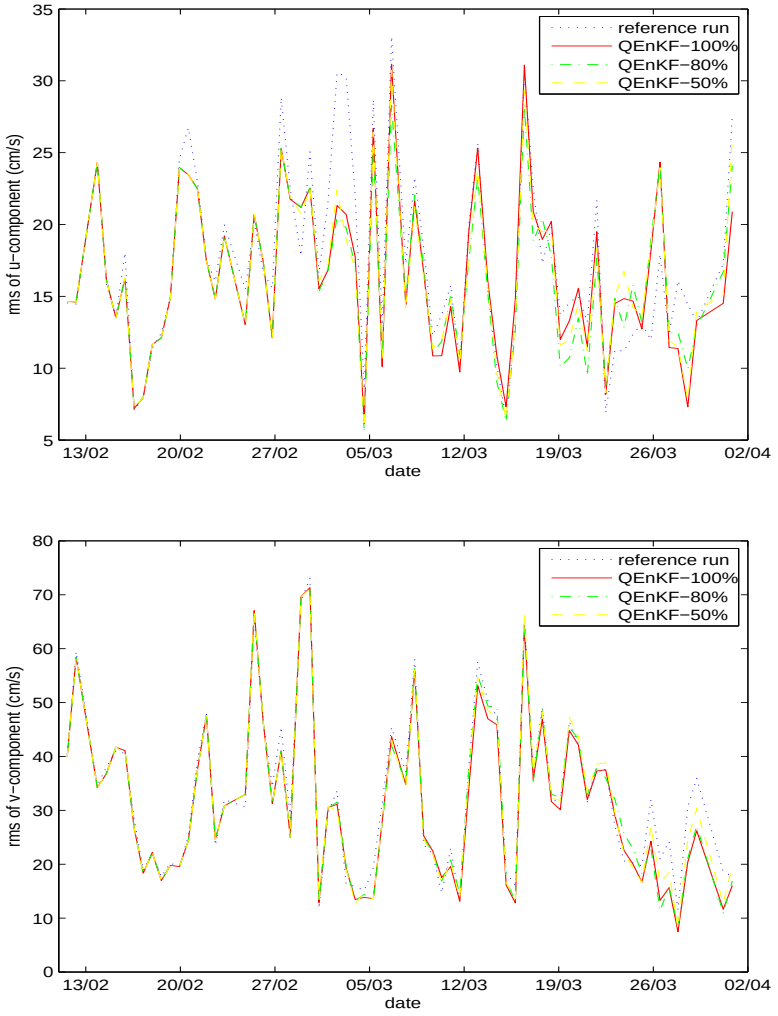

FIGURE 6.19: Root-mean-square errors of u-component (upper panel) and v-component (lower panel) relative to HF radar data in the reference run (dotted line), $S100$ (solid line), $S80$ (dash-dotted line), and $S50$ (dash line), respectively.

runs. Even the point which is located in the radar area, shows the same features. Hence, the changes of the observational density does not affect the update of temperature too strongly. That demonstrates that the update of temperature caused by the velocity assimilation has only a weak correlation with the density of the velocity data. Since the radar velocity data are only concentrated in a very small area, when the density of them changes, the assimilation effect produces only small changes. However, the results for temperature with assimilation and without assimilation are quite different. The maximum values of corrections of the temperature are around 0.6 to 0.8 degrees for the northern points, 0.8 to 1.5 degrees for the central points, and 0.2 to 0.5 degrees for the southern points.

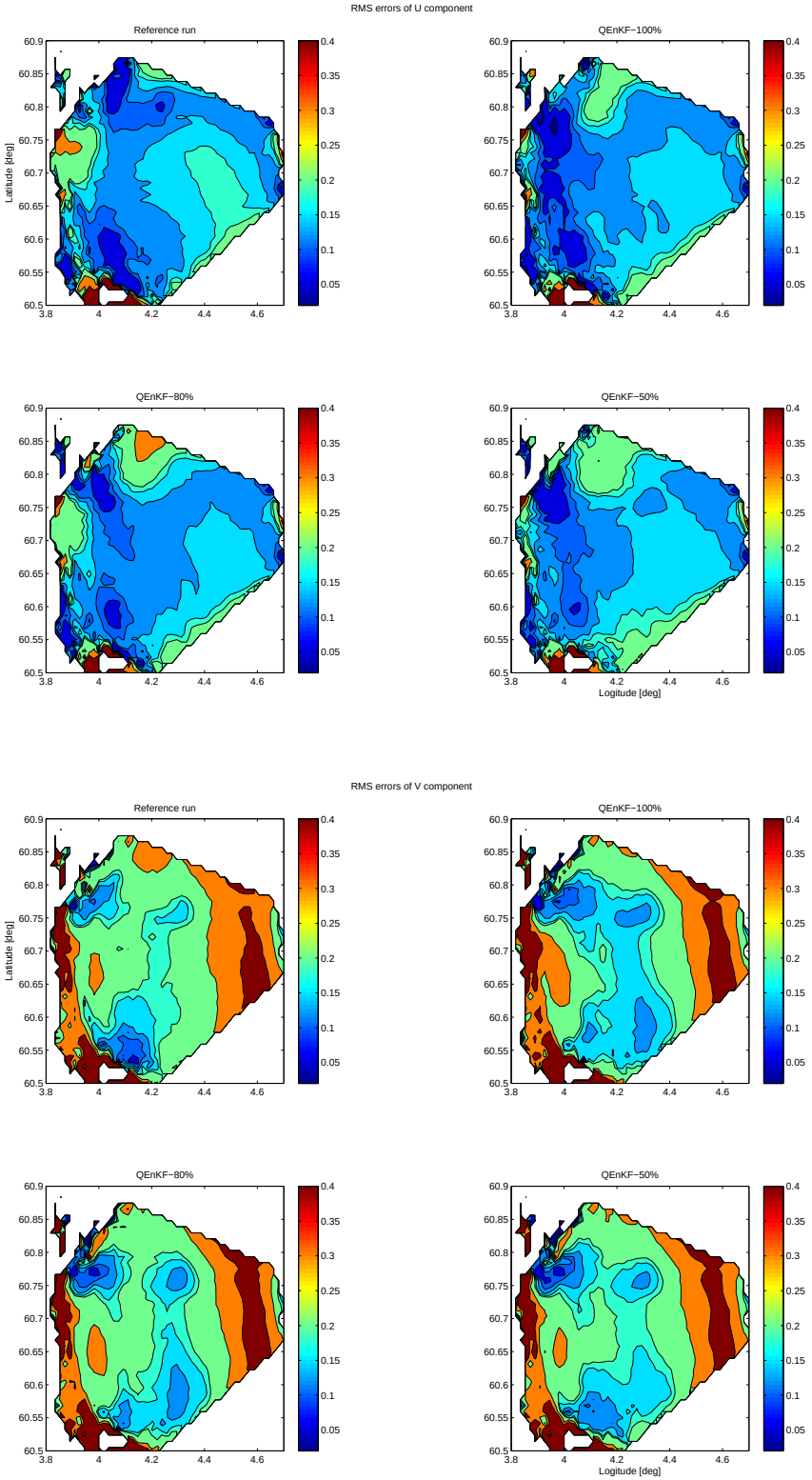

FIGURE 6.20: Temporally averaged root-mean-square errors (m/s) of u-component (upper four panels) and v-component (lower four panels) relative to HF radar data, in the reference run, $S100$, $S80$, and $S50$, respectively.

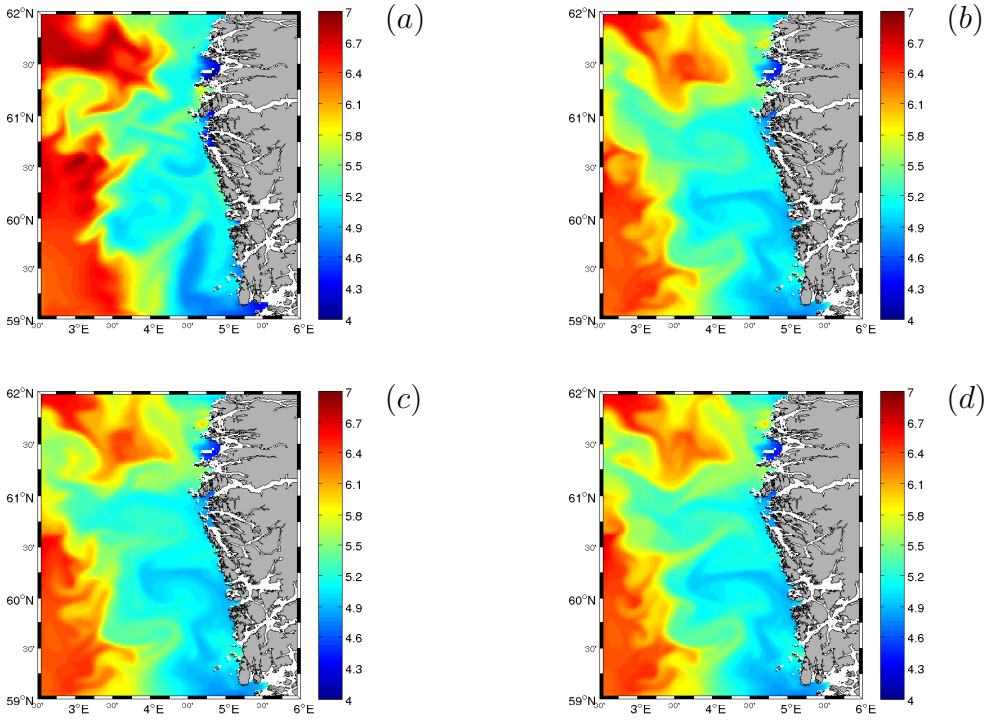

FIGURE 6.21: Surface temperature fields of the reference run (a), $S100$ (b), $S80$ (c), and $S50$ (d), respectively on March 31, 2000.

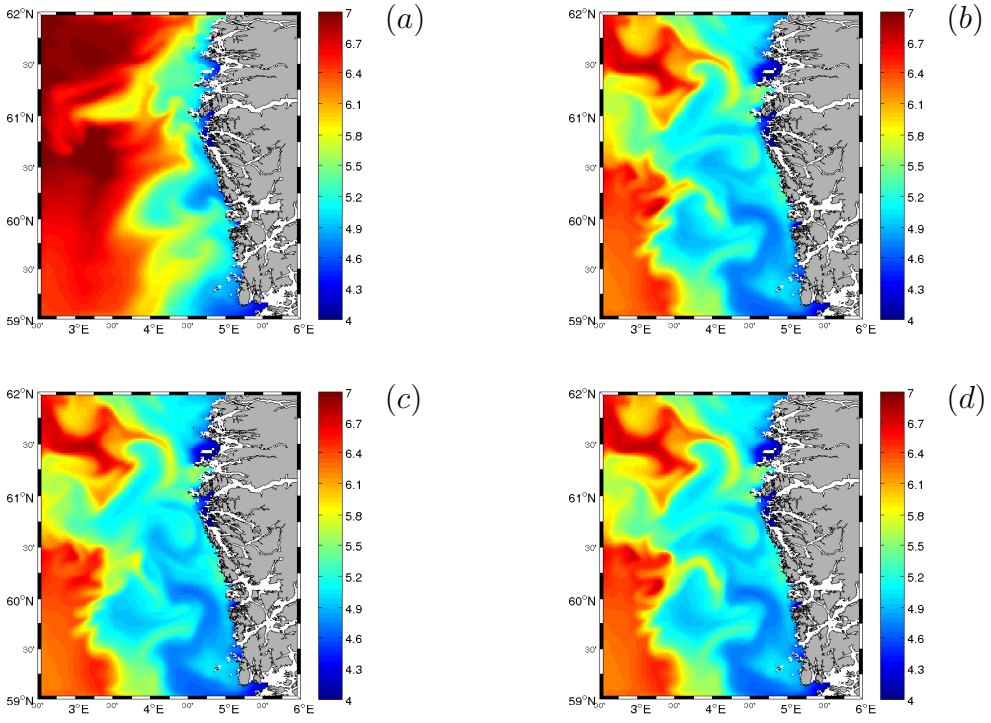

FIGURE 6.22: Surface temperature fields of the reference run (a), $S100$ (b), $S80$ (c), and $S50$ (d), respectively on March 15, 2000.

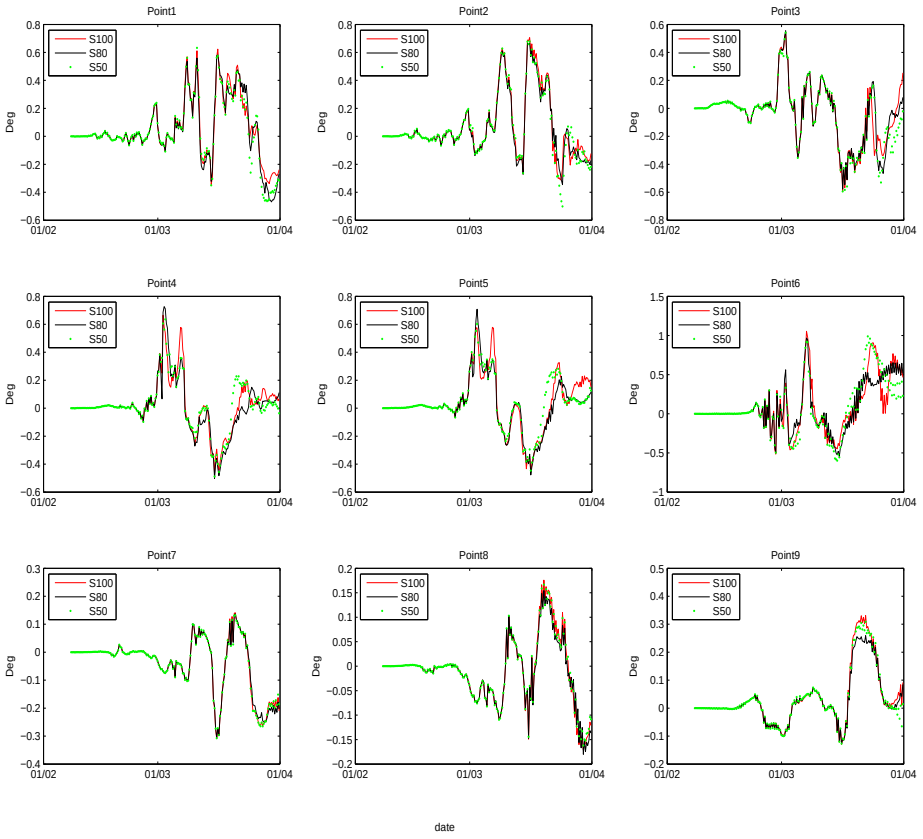

FIGURE 6.23: The differences of temperature located at 9 points between in assimilation runs and in the reference run, with the red line, black line and the green dotted line represent the $S100$, $S80$, and $S50$, respectively.

6.2.3 Conclusion of Variation of Observation Density

The comparisons of the three assimilation runs with different observational densities indicate that, first of all, our QEnKF assimilation method is successful, since with the observational number decreasing, the effect of assimilation decreases too, that can be easily deduced from the changes of spatial RMS errors. Secondly, when the observations get sparse, the correlation between them becomes lower, then the update of the analysis decreases, and the changes are more obvious in u-direction than in v-direction. In the end, due to the weak correlation between temperature and velocity and the fact that the radar data are only concentrated in a relatively small area, the update of temperature is not affected too strongly by the variation of the observational density. Besides, the corrections of temperature in the north of the model domain are larger than in the south, since the main direction of the current in this area is directed northward.

6.3 Avoiding Filter Divergence

As we mentioned in chapter 2, the divergence is one of the most serious disadvantages of the EnKF technique. That happens when the prior covariances are too small, caused by sampling error or other approximations. The small prior covariances result in the fact that less weight is given to the new observations when they are used for the next analysis, which further reduces the prior covariance for the next estimate. Eventually, the observations may no longer impact the prior estimate, and the assimilation will depart from the observations. That is usually called assimilation "divergence".

One method for dealing with this problem is multiplying the prior covariance matrix by a constant factor (Anderson, 2001; Hamill et al., 2001). The expectation of this treatment of covariance matrix is to maintain the balances in phase space, as well as to increase uncertainty of the state estimate.

Another method was used by Hamill and Snyder (2000), which is named the hybrid EnKF method, whereby covariances are modeled as a combination of covariances from the ensemble and from a stationary model like 3DVAR. By adjusting the ratio of both, the filter divergence is avoided.

Houtekamer and Mitchell (1998) used a "double" EnKF technique, whereby ensemble members are kept in two separate batches, and the covariances from one batch are updated using the gain matrix calculated from the other batch. However, van Leeuwen (1999) pointed out that the DEnKF has a similar, but smaller, "inbreeding" problem which is caused by using the gain calculated from the ensemble to update the same ensemble.

However, in the QEnKF method, the prior covariances are calculated from the forecast tendencies. Thus, the prior covariances change with the changes of the forecast tendencies, do not keep decreasing as in the EnKF method. However, we tried the first method in the QEnKF method, i.e, is magnifying the forecast error covariances by a constant factor. According to the analysis equation (2.21), when the magnitude of the forecast error increases, the correction by assimilation will decrease, and vice versa. Since the standard assimilation run ($QEnKFrun$) already behaves quite well, which means the magnitude of forecast errors is big enough. Hence, in order to investigate the effects of magnifying the forecast error, a test is performed with a reduced forecast error. Altogether the following three experiments have been conducted.

- Freerun: the reference run we always used as before.
- QEnKFrun: the standard assimilation run using the QEnKF method, in which the forecast error covairances are directly calculated from the forecast tendencies.
- QRun2: the run is almost the same as QEnKFrun, but with reducing the magnitude of forecast error covariances by a factor of 2.

6.3.1 Comparison of Updated Surface Currents

As usually, the surface velocity fields of these experiments at two arbitrary dates, which are 23 : 40 on March 26, and 23 : 40 on March 31, are compared and shown in Fig.6.17 and Fig.6.18, respectively. In these two figures, the panel (a), (b), (c) and (d) represent the velocity fields of radar data, the reference run, the standard assimilation run, and the assimilation run with decreasing forecast errors, respectively. In the first figure (6.17), we observe that, when the magnitude of forecast error covariance decreases (panel (d)), the correction by the assimilation decreases too. On the contrary, we can expect that when the forecast errors be magnified, the effects of observations will increase. This phenomenon is also what we can expect according to the analysis equation in assimilation system.
The same comparisons of panels is given in Fig.6.18 for the second date. At this date, an eddy exists in the observation and the reference run, but the structure of it is different in this two fields. By investigating the existence of the eddy, the same conclusions as in the last figure can be drawn. The comparison of panel (b) and (d), where only the magnitude of forecast error is different in the two experiments, clearly indicates how much the data assimilation is degraded if the prior error covariances are underestimate or too small.
However, even if the target of this method is to avoid filter divergence in the traditional EnKF method, it is also suitable for the QEnKF method. Since the QEnKF method uses the same analysis equation as the EnKF method. In fact, with the usage of specifying the prior error covariances P^f in terms of the model variables, the structure of it can be written as equation (6.3.1),

$$P^f = \langle A', A' \rangle = \left\{ \begin{matrix} \sigma^2\rho & \bullet & \bullet \\ \bullet & \bullet & \bullet \\ \bullet & \bullet & \bullet \end{matrix} \right\} = \text{variances (magnitude)} \times \text{correlation.} \qquad (6.1)$$

Table 6.2: RMS Errors (cm/s)

Experiment	u (Mar26)	v (Mar26)	u (Mar31)	v (Mar31)
QEnKFrun	12.45	15.43	26.14	23.69
QRun2	11.73	18.80	28.68	28.80
Reference run	13.02	25.24	34.13	26.62

Since in the QEnKF system, the background errors or forecast errors are represented by the forecast tendencies, if only the magnitude of them changes, like in experiment $QRun2$, the patterns of the error covariances do not change, and the postiror error covariances will not be propagated by the model integration. Hence, the effect of this method is not too strong. However, the newly developed method (QEnKF) is sensible to the model time step, since it not only decides the magnitude of forecast errors, but also the patterns of the error covariance. Hence, sensitivity tests with this parameter are inevitable. However, once the model configuration and validation is finished, the appropriate model time step can be diterminted very easily.

At the end, the RMS errors of these experiments relative to the HF-radar data are also computed in the observational space. Fig.6.26 gives the time series of the RMS errors for the u-component (left panel) and v-component (right panel). From the picture, we can see that at most times, the RMS errors of experiment $QRun2$, in which only the magnitude of the forecast error is reduced, are almost the same as of the standard assimilated run $QEnKFrun$, but a little bit larger than of the latter. Besides, the differences between the $QEnKFrun$ and $QRun2$ in the u-direction are relatively larger than in the v-direction. Here, we only consider the RMS errors at those two moments (Table 6.2), which clearly shows the effect of the magnification of the magnitude of forecast error.

6.3.2 Comparison of Updated Temperature

Fig.6.27 shows the resulting surface temperature fields of these experiments and of MODAS (panel (a)) on March 31, which is the last day of the assimilation procedure. Fig.6.28 shows the comparisons of the same variable on another arbitrary day, which is March 15. The comparisons of the different experiments given in these two figures (panel $(a-c)$) indicate that the change of the magnitude of the forecast errors does not impact the update of temperature too strongly. However,

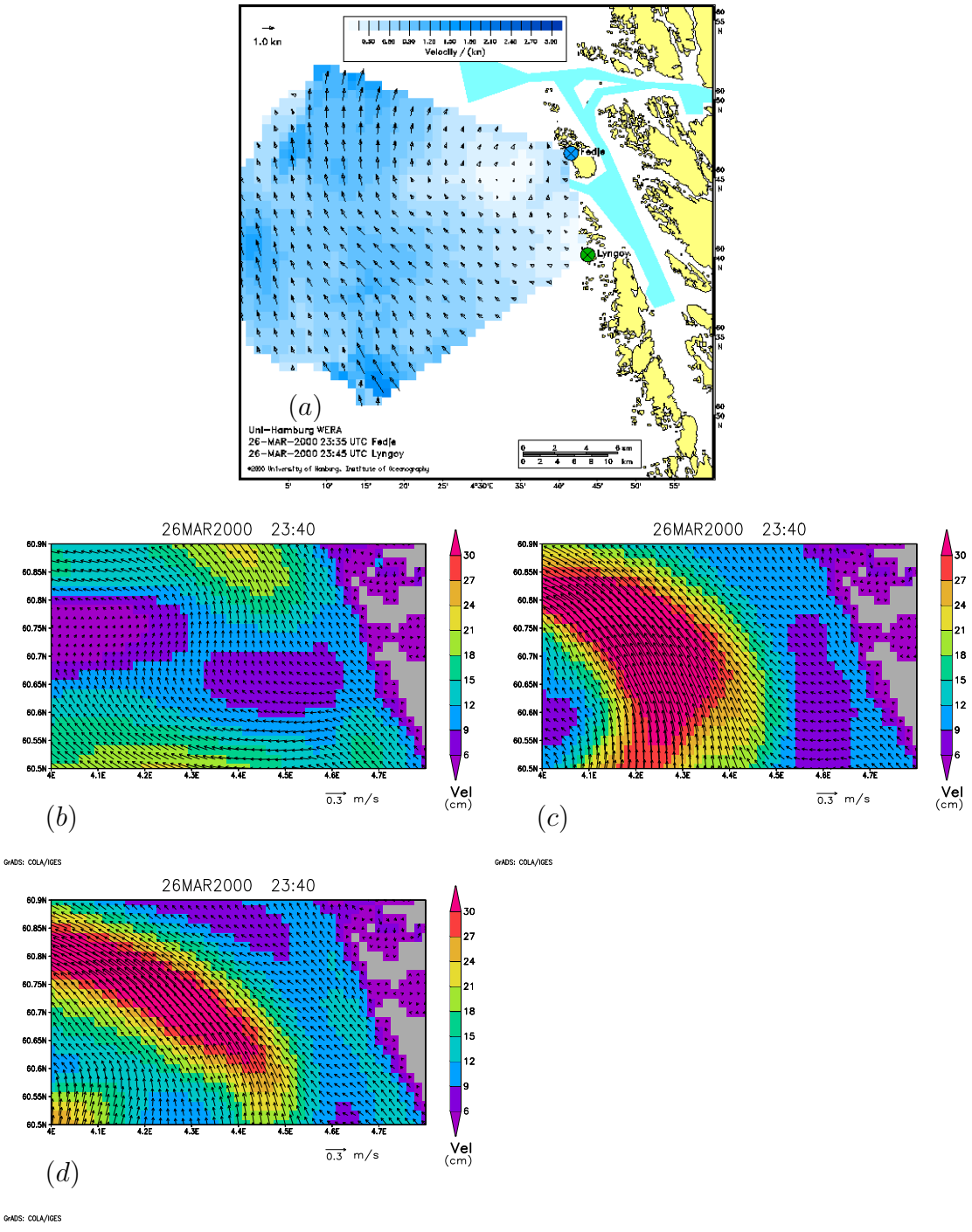

FIGURE 6.24: Surface current fields zoomed into the area covered by the HF-radar. Radar data(a), Freerun(b), QEnKFrun(c), QRun2(d), respectively, at 23 : 40 UTC on March 26, 2000

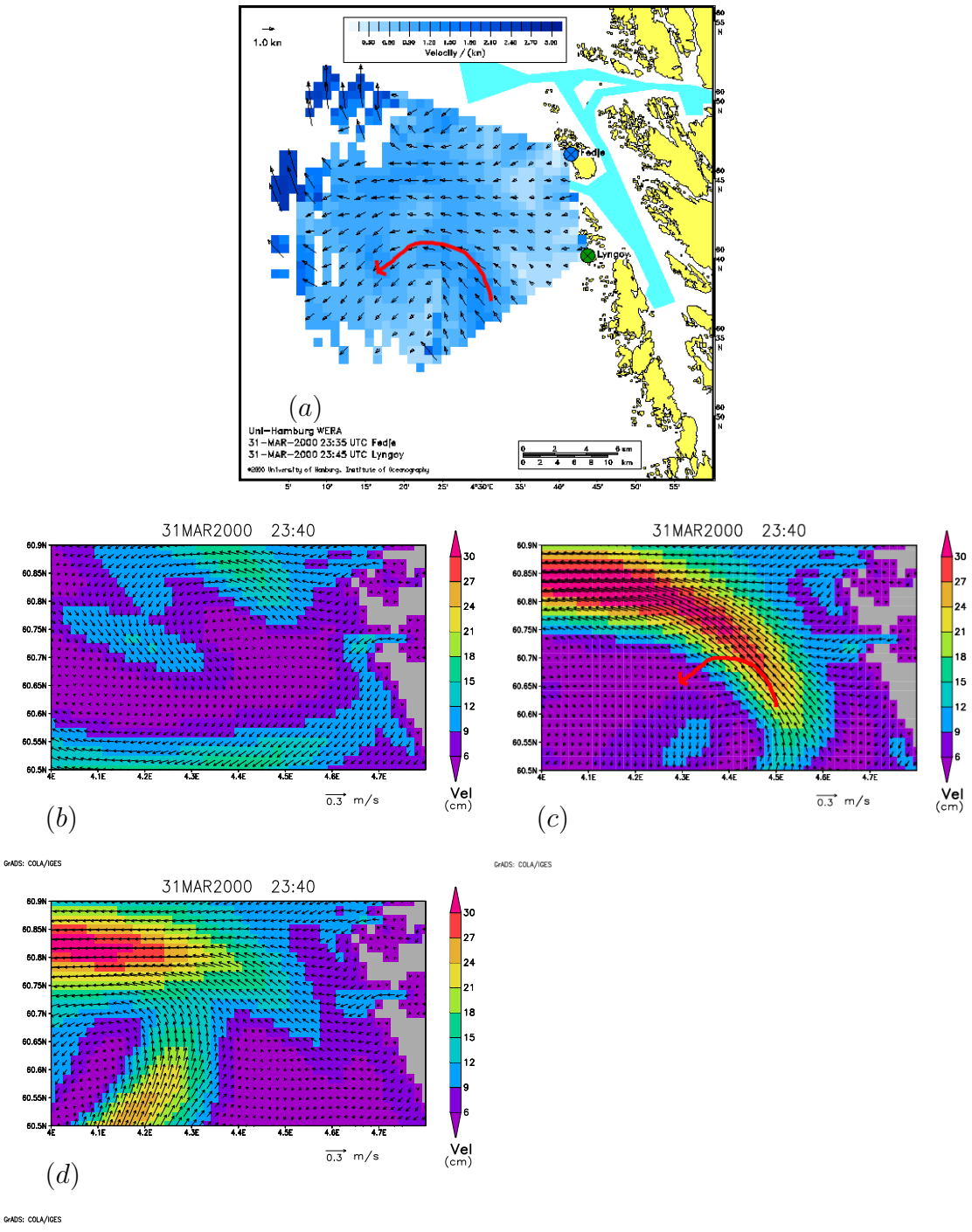

FIGURE 6.25: Surface current fields zoomed into the area covered by the HF radar. Radar data(a), Freerun(b), QEnKFrun(c), QRun2(d), respectively, at 23 : 40 UTC on March 31, 2000

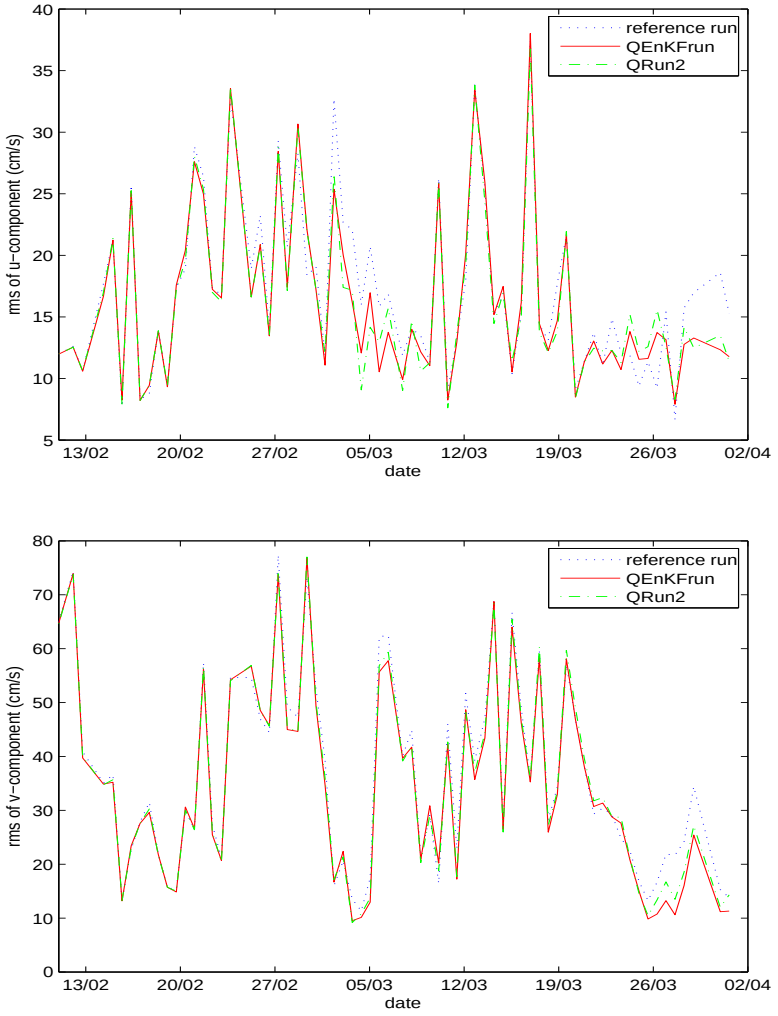

FIGURE 6.26: Root-mean-square errors of u-component (upper panel) and v-component (lower panel) relative to HF radar data, in the reference run (dotted line), experiment $QEnKFrun$ (solid line), $QRun2$ (dash-dotted line), respectively.

there are obvious differences between the assimilation runs and the reference run, that means the update of temperature caused by assimilation decreases less than for velocities with this method. Meanwhile, since the MODAS data is independent on our model simulation results, by comparing the temperature fields between them, we find that the assimilated temperature distributions are more similar to the realistic situation (MODAS data).

Besides, the same 9 points as introduced in section 6.2.2 are used again. The differences of temperature (also referred to as update of temperature) between the different assimilation runs and the reference run at these points are shown in Fig.6.29.

Since the temperature is a scalar variable, by diagnosing the update of it, the

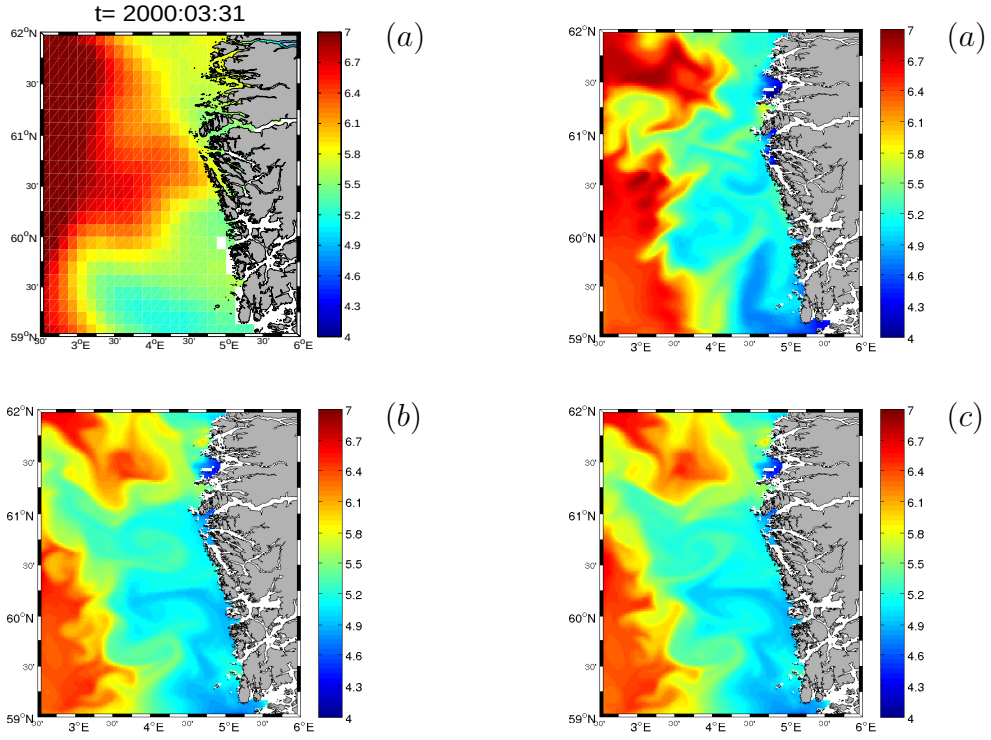

FIGURE 6.27: Surface temperature fields of MODAS (a), *Freerun* (b) and $QEnKFrun$ (c), and $QRun2$ (d), respectively on March 31, 2000.

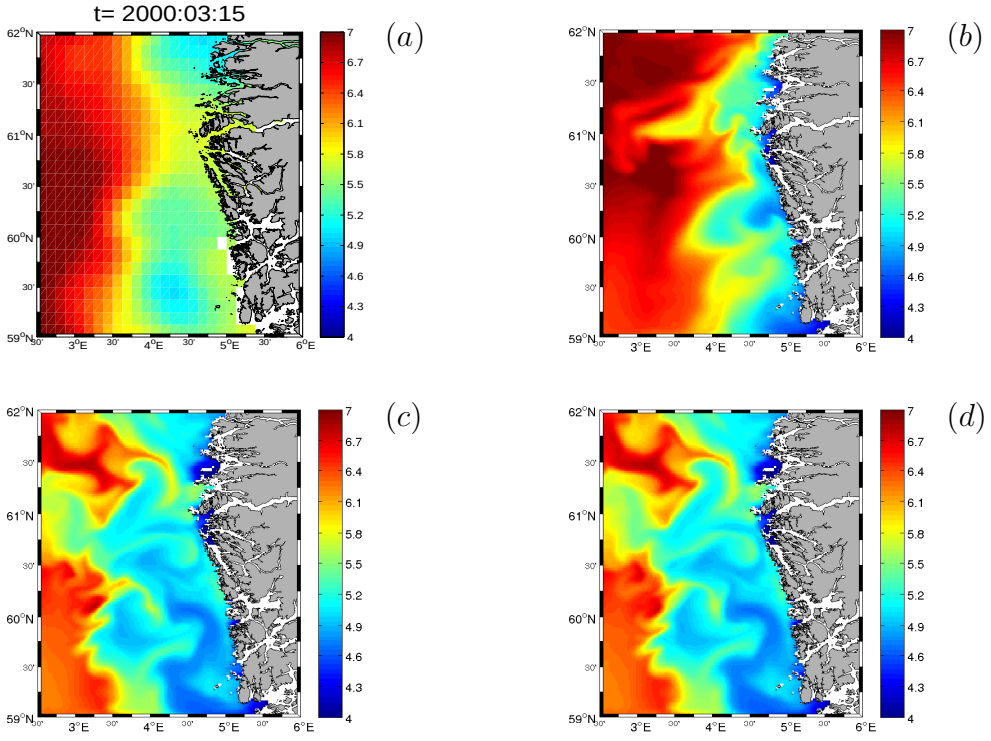

FIGURE 6.28: Surface temperature fields of MODAS (a), *Freerun* (b) and $QEnKFrun$ (c), and $QRun2$ (d), respectively on March 15, 2000.

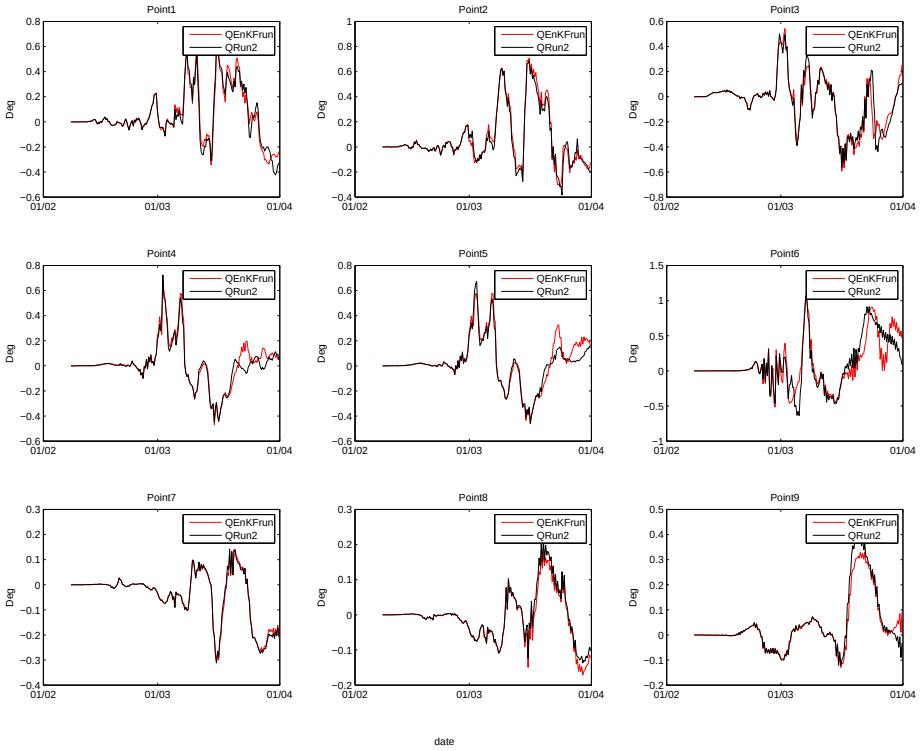

FIGURE 6.29: The update of temperature by assimilation of 9 specified points, with the red line and black line representing the $QEnKFrun$ and $QRun2$, respectively.

detection of the assimilation effect is more easy to conclude compared to a vector variable. In the Fig.6.29, the red line and black line represent the update of temperature of experiment $QEnKFrun$ and $QRun2$, respectively. Obviously, the corrections in $QRun2$ are almost as the same as in $QEnKFrun$, which indicates taht the results of the assimilation run by magnifying the forecast error ($QRun2$) agree with the results of $QEnKFrun$ very well.

6.3.3 Conclusion of Avoiding Filter Divergence

One popular way to avoiding filter divergence is by magnifying the error covariance. The test of this possibility in the QEnKF method indicates that it does carry weight with avoiding filter divergence, but this ability is not very large, since the patterns of prior error covariances do not change and will not be propagated by the model intergation. Hence, the update of temperature and velocity field using this method changes quite slowly.

However, in our QEnKF method, the forecast tendencies are used to represent the forecast errors, which will change with the variantion of the model time step. Thus, the newly developed method (QEnKF) is sensible to the model time step. However, once the model configuration and validation is finished, the appropriate model time step can be diterminted very easily. Besides, the sensitivity tests with this parameter are much easier to perform compared to the choice of the ensemble size in the traditional EnKF method. Anyway, the experiment of magnification of the forecast error inspire us that when the model time step is fixed, one way to enlarge the state sapce is to magnify the magnitude of the forecast error.

6.4 Maintaining Prior Covariance

In the original EnKF method, the state members in the ensemble are updated independently from all others. If two members that are closely related in the prior distribution are impacted by very different subsets of observations, they may end up being too weakly related. One solution is used by letting every state member be impacted by all subsets of observations. However, since some of these observations will be highly correlated with the state variable by chance, an erroneous impact will be generated on the updated ensemble (Hamill et al., 2001). Hence, Houtekamer and Mitchell (2001) and Hamill et al. (2001) have filtered the covariance estimates by using a "Schur product", whereby the ensemble-based covariances are multiplied with a distance-dependent correlation function that decreases monotonically from 1.0 at the observation location to 0.0 at some prespecified radial distance. Each individual observation is assimilated sequentially to reduce the rank of the gain matrix.

Evensen and van Leeuwen (1995) used an eigenvalue decomposition to solve the system and only the significant eigenvalues are used, which can resolve the problem with poor conditioning caused by correlated measurements, as well as with a singular matrix introduced when the number of measurements is larger than ensemble member size. Evensen (2004) developed therefore a square root analysis schemes for the EnKF. The details of it are given in appendix A. We used the same code as the one Evensen provided via internet (http://enkf.nersc.no/).

However, in our case, the observations are only located in a specified area. In order to avoid the illusive high correlation between observations and model states, which are located far from observation locations, a distance-dependent filter is also

used in all the assimilation experiments. That means in the projection function H, the correlation of points beyond the radar area is set to 0. Besides, the solution of analyzing every model member by all the observations is also used. Moreover, due to the usage of the square root analysis schemes (Appendix A), the mean of the ensemble members is impacted by the mean of observations, which is equal to the real observations without perturbations. Hence, the problem of an erroneous impact of measurements generated by unrealistically high correlations which is discussed by Hamill et al. (2001), is solved.
In order to further reduce the rank of the gain matrix, another assimilation is performed by assimilating the u-velocity and v-velocity sequentially, referred to as $SplitRun$. This operation results in the fact that the dimension of matrix D is reduced, and then of matrix R in the following, eventually of the gain matrix. All the other model setups are the same as standard assimilated run ($QEnKFrun$).

6.4.1 Analysis of Surface Current

Fig.6.30 shows the surface current fields of the radar data (panel (a)), the reference run (panel (b)), the standard assimilated run (panel (c)), and the run employing a sequential assimilation of the u- and v- components (panel (d)) at the end of the assimilation procedure. At this date, there is an obvious eddy marked by the big-red arrow in the radar data, which can not be observed at the same location in the reference run. After the assimilation with the QEnKF method, this eddy appears again at the same location as observed in the radar data. But the magnitude of the eddy in the $QEnKFrun$ is a little smaller than in the observation. When the u- and v- components are assimilated independently and sequentially into the shelf model, the eddy simulated in this run is not only at the same location as in the observation, but also has the realistic magnitude.
Besides, at another arbitrary date, the surface current fields of the two assimilation runs compared to the reference run and the radar data are shown in Fig.6.31. At this date, there is no complex structure of current in the radar area, the comparisons of velocity magnitudes of different assimilation runs illustrate that, after assimilation of the u- and v- variables sequentially, the rank of the gain matrix is reduced, and the results of the assimilation get better.

The time series of RMS errors of this assimilation run related to the radar data are also calculated, and shown by the dash-dotted line in Fig.6.32. The dotted

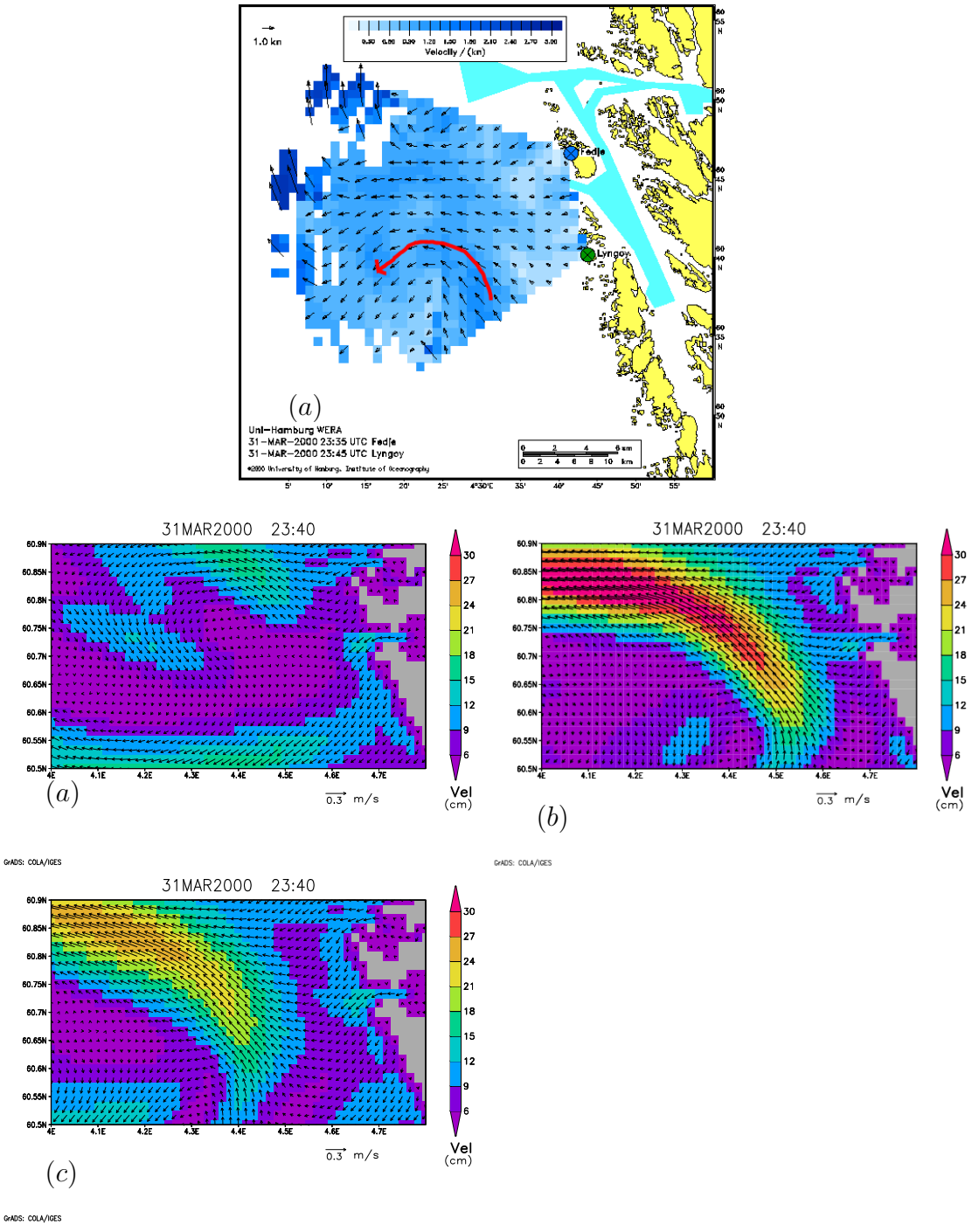

FIGURE 6.30: Surface current fields zoomed into the area covered by the HF radar. Radar data(a), the reference run(b), *QEnKFrun*(c), *SplitRun*(d), respectively, at 23 : 40 UTC on March 31, 2000

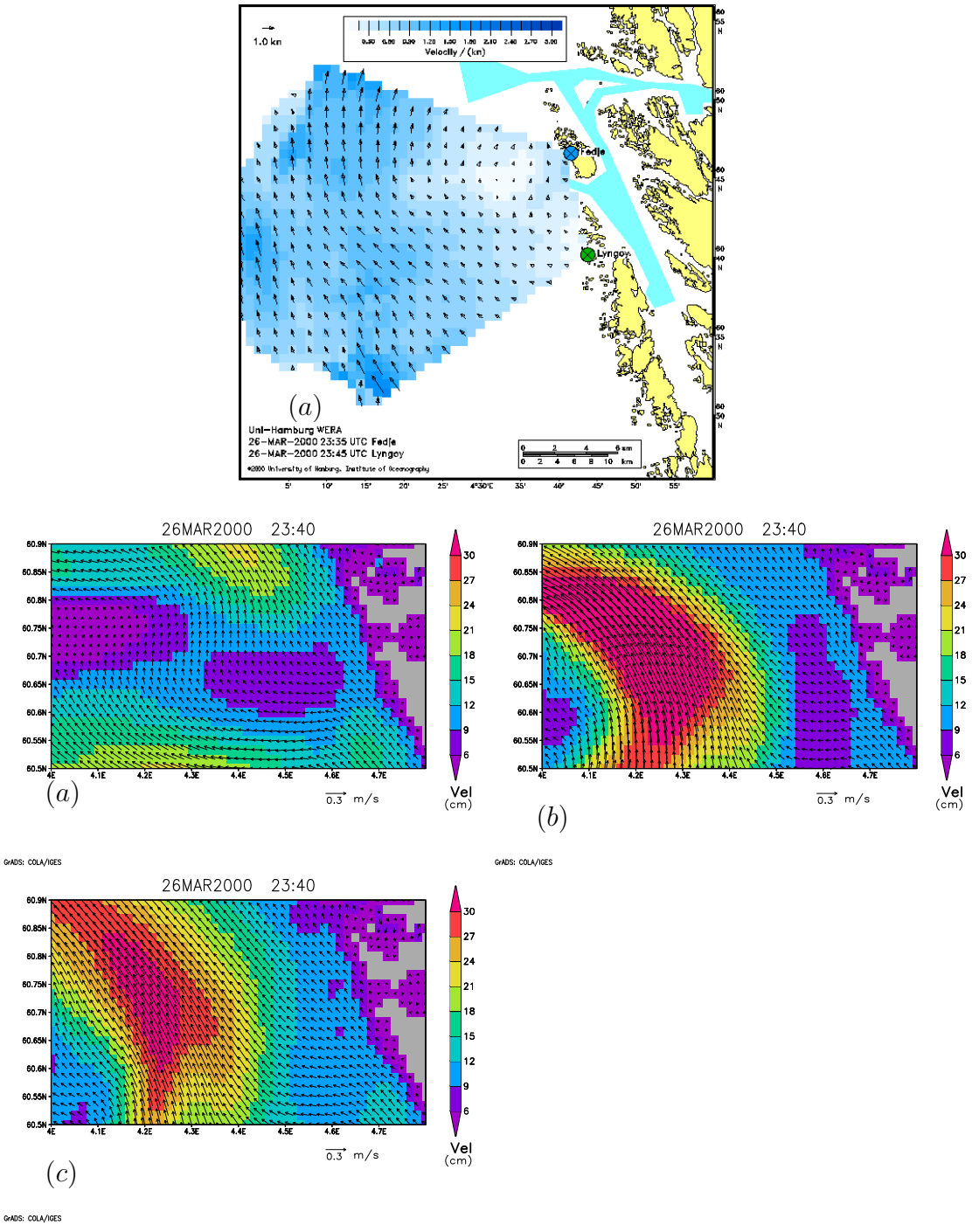

FIGURE 6.31: Surface current fields zoomed into the area covered by the HF radar. Radar data(a), the reference run(b), $QEnKFrun$(c), $SplitRun$(d), respectively, at 23 : 40 UTC on March 26, 2000

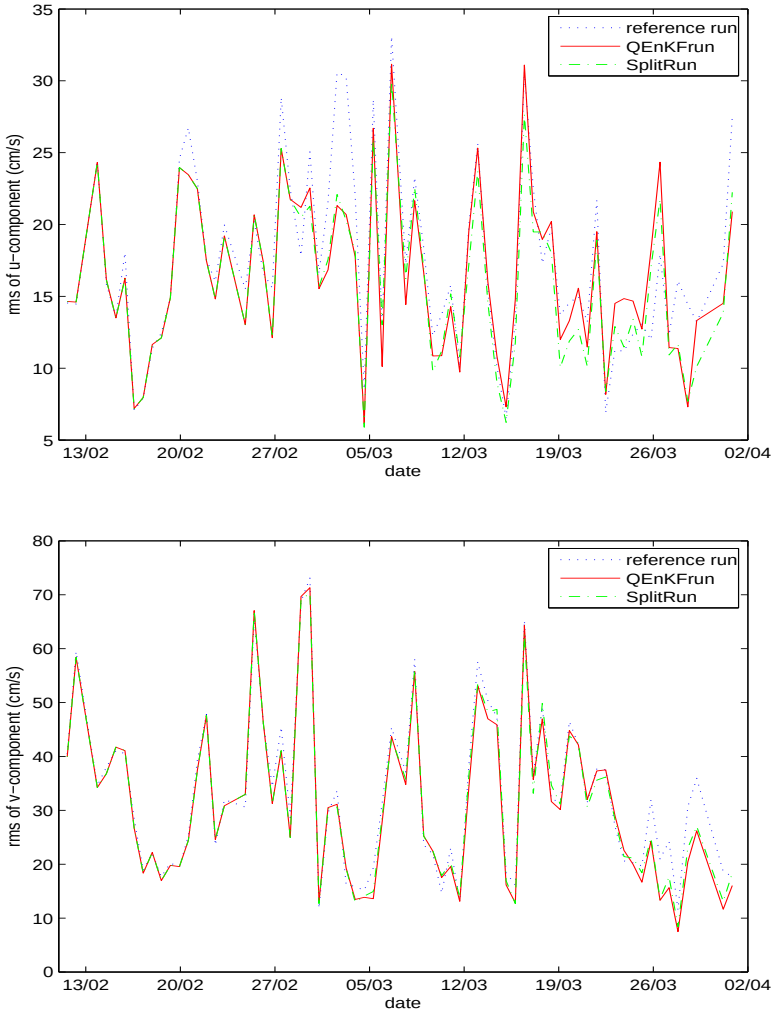

FIGURE 6.32: Root-mean-square errors of u-component (upper panel) and v-component (lower panel) relative to HF radar data, in the reference run (dotted line), $QEnKFrun$ (solid line), and the run with assimilating u and v sequentially (dash-dotted line), respectively.

line and solid line still represent the RMS errors of the reference run and the standard assimilation run. The figure shows that at most times, the RMS errors of the second assimilation run agree well with the first assimilation run, but with time, errors are getting smaller than for the first assimilation run, especially in the u-direction.

6.4.2 Analysis of Updated Temperature

With sequential assimilation of the observational velocities, the rank of the gain matrix in the analysis equation is further reduced, which makes the velocity fields

after assimilation to be more in agreement with the observations. Then we are interested in the changes of updated temperature after such operation. However, based on the conclusion of former experiments, it's clear that the update of temperature is not as sensitive as the update of velocities, not to mention when the update of velocities is small. Hence, we expect that the temperature fields of sequentially assimilated u- and v- components behave similar in this experiment. To prove this, the updates of temperature of the standard nine points are presented in Fig.6.33.

As we described before, the first row of panels show the results of the northern points, the second row shows the central points, and the last row shows the southern points. Besides, from the left to the right panels, the points move from the surface to the bottom. The panels indicate that there are a few disparities between the two assimilation runs at the northern and southern points, since they are located relatively far from the observational domain. Even in the central points, the differences are quite small. That means, the update of temperature is not sensitive to the reduction of the rank of the gain matrix, or to the update of the velocity fields.

6.4.3 Conclusion of Maintaining Prior Covariance

The way to assimilate each individual observation sequentially is a popular method to reduce the rank of gain matrix. Since our HF-radar observational data are not sparsely located, but concentrate in a small area and have relatively high correlation with each other. In our experiment we reduced the rank of the gain matrix not by assimilating the observational data one by one, but separated them into two batches, i.e., u-component and v-component, as well as using the significant eigenvalues through an eigenvalue decomposition.

By assimilating the u- and v-variables sequentially, the assimilation results are better improved in the twin assimilation. However, the benefit of this method is more obvious in the update of velocity fields than in temperature fields. That means the corrections of the latter are not as sensitive as the former.

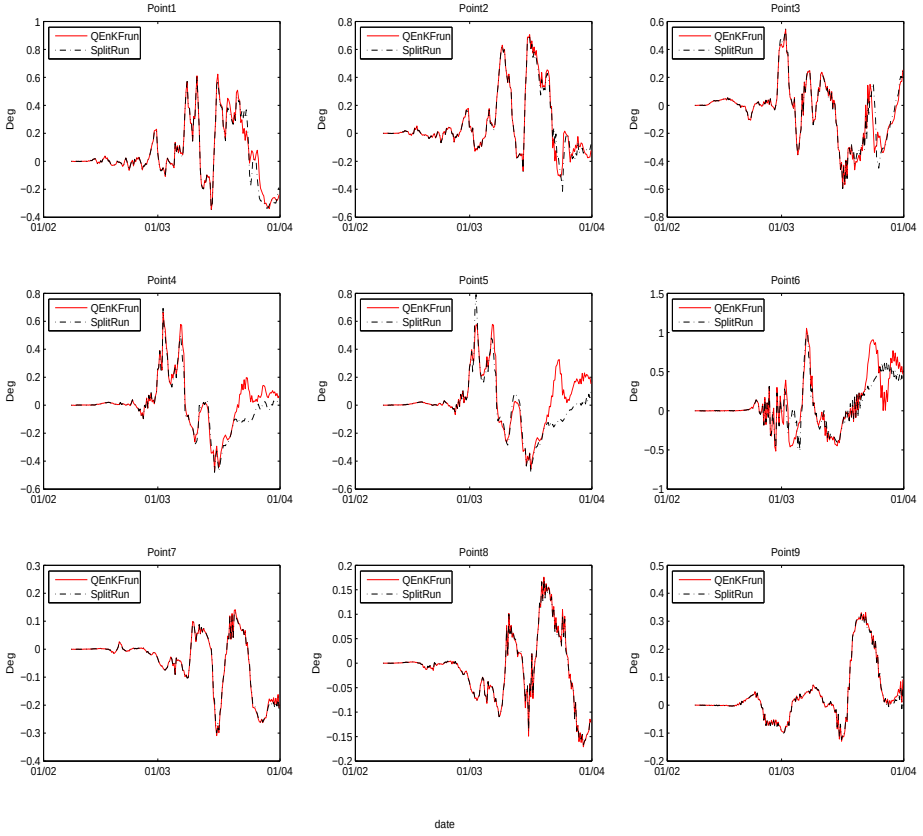

FIGURE 6.33: The update of temperature by assimilation of 9 specified points, with the red line and black line representing the QEnKFrun and SplitRun, respectively.

6.5 Assimilation Parameters

In the traditional EnKF method, the rank of gain matrix and the ensemble size are two primary parameters. Moreover, the rank of the model error covariance matrix is essential to the performance of an assimilation scheme. For the traditional EnKF this is equal to the ensemble size, however, with the usage of the square root analysis schemes, the rank is reduced, while for the Reduced Rank Square Root (RRSQRT) Kalman filter (Bertino et al., 2002), the number of leading eigenvalues are preserved to determine the covariance reduction. In our QEnKF method, the same equations and square root analysis schemes are used as in the EnKF method. Hence, the rank of the gain matrix is already reduced. By assimilating the u- and v- variables of the observation sequentially, the rank is further reduced, the consequence of the rank-reduction operation is described in detail in section 6.4. Furthermore, the experiments illustrate that the rank problem is not a burden

Table 6.3: RMS Errors (cm/s)

Experiment	u (Mar26)	v (Mar26)	u (Mar31)	v (Mar31)
QEnKFrun	12.45	15.43	26.14	23.69
Doublerun	12.22	15.04	26.80	25.06
Reference run	13.02	25.24	34.13	26.62

anymore in our new developed system.

Among the other parameters, the ensemble size is a very important factor, which is already discussed in the methodology chapter. It has been shown that sufficient ensemble members are the prerequisite for the assimilation with the traditional EnKF method. That is also the reason that high-frequency assimilation with the traditional EnKF is difficult to implement. However, in our newly developed QEnKF method, the ensemble size no longer decides the forecast error covariance, which means that the importance of the matrix is largely reduced. On the contrary, the model time step becomes the crucial parameter, since the forecast errors are represented by the forecast tendencies, which makes the model time step influence the magnitude of the forecast error covariance. However, by using the method of magnifying the magnitude with a constan factor, which was discussed in section 6.3, the variation of model time step is much easier than the variation of ensemble size in the traditional EnKF method.

The ensemble size, in QEnKF system, is decided by the model time step and the representative time-length. For example, in our experiments, the observations are available every 20 minutes, and the forecast tendencies in these 20 minutes can represent the real-time forecast errors, which means with a model time interval equal to 2 minutes, 10 ensemble members of forecast tendencies are sampled. If the ensemble size increases, that means the representative time-length increases, and vice versa. In order to test the effect of ensemble size, another assimilation run with an ensemble number equal to 20 is implemented, and referred as *Doublerun*. The time series of the RMS errors related to the HF-radar data of this assimilation run are also calculated, and shown by the dash-dotted line in Fig.6.34. The dotted line and solid line still represent the RMS errors of the reference run and the standard assimilation run. The figure shows that nearly always, the RMS errors of the second assimilation run agree well with the first assimilation run, but are a little larger than of the first assimilation run, especially for the v-direction. As usual, we only show the RMS errors at two dates, which are 23 : 40 UTC on March 26 and 31, 2000. The values are given in Table 6.3.

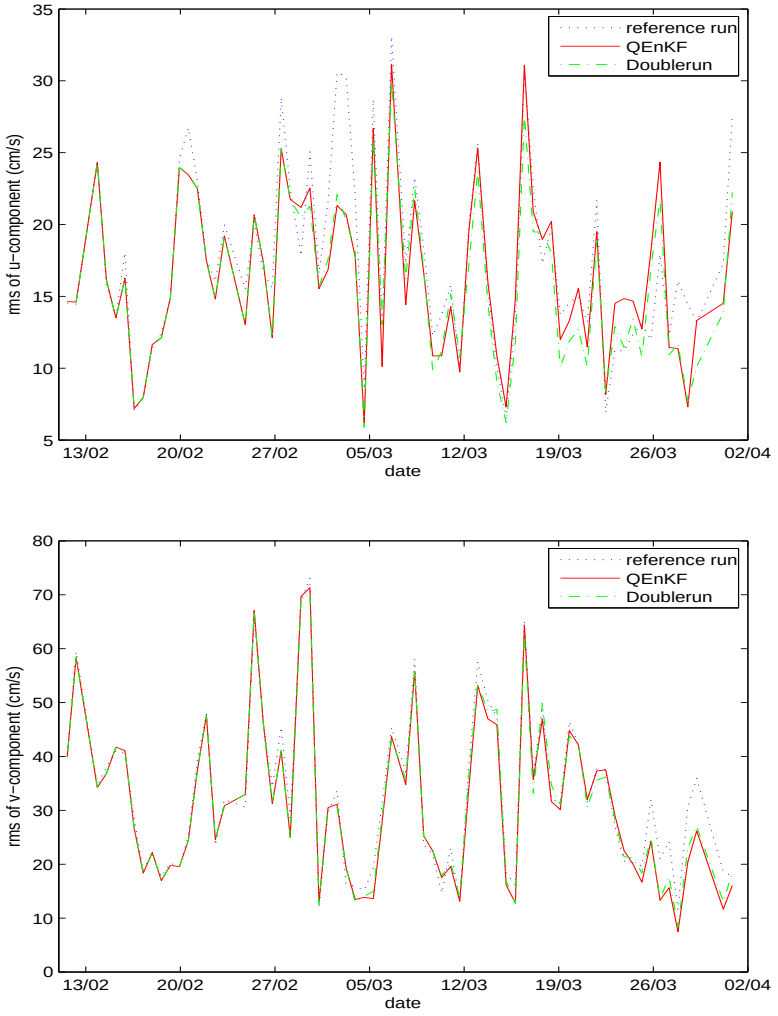

FIGURE 6.34: Root-mean-square errors of u-component (upper panel) and v-component (lower panel) relative to HF radar data, in the reference run (dotted line), $QEnKFrun$ (solid line), and the run with double ensemble size (dash-dotted line), respectively.

6.6 Vertical Impact of the Surface Corrections

As explained before, the correlations of the surface velocity and in preticular with other vertical variables are not high, only the surface variables (including temperature, salinity, elevation and velocity) are analyzed in the assimilation system. However, the surface update are broadcasted by model propagation to the model interior. In fact, we also implement a real three dimensions assimilation, which means all the variables from the surface to bottom are included in the analysis equation. We call it $3Drun$ in the following.

First of all, we would like to see the velocity fields of two assimilation runs from

the surface to bottom at the end of the assimilation procedure, which are shown in Fig.6.35. The first row, second row and last row of this figure represent the velocity fields at surface, central and bottom layer, and the left column corresponds to the standard assimilated run, and the right column to the real $3Drun$. The comparisons of the column panels demonstrate that there are a few differences between the two assimilation runs. In other word, since the correlation between surface variables with vertical variables is low, the differences of assimilated velocity fields from surface to bottom between the run with only analyzing surface variable and the run with analyzing all three dimensional variables, are quite small. Hence, the strategy that the state vectors only includes the surface variables is acceptable.
In order to evaluate the magnitude of the differences (assimilated values minus reference run results) along the depth, the velocity differences at this date are calculated and shown in Fig.6.6. The figure indicates that the modification introduced by the assimilation can be projected into the interior of model, but decreases with depth. The major changes caused by the assimilation are found in the central part of the water column, where the HF-radar data are available and have the best quality. Moreover, the structure of the changes are consistent from the surface to the bottom.

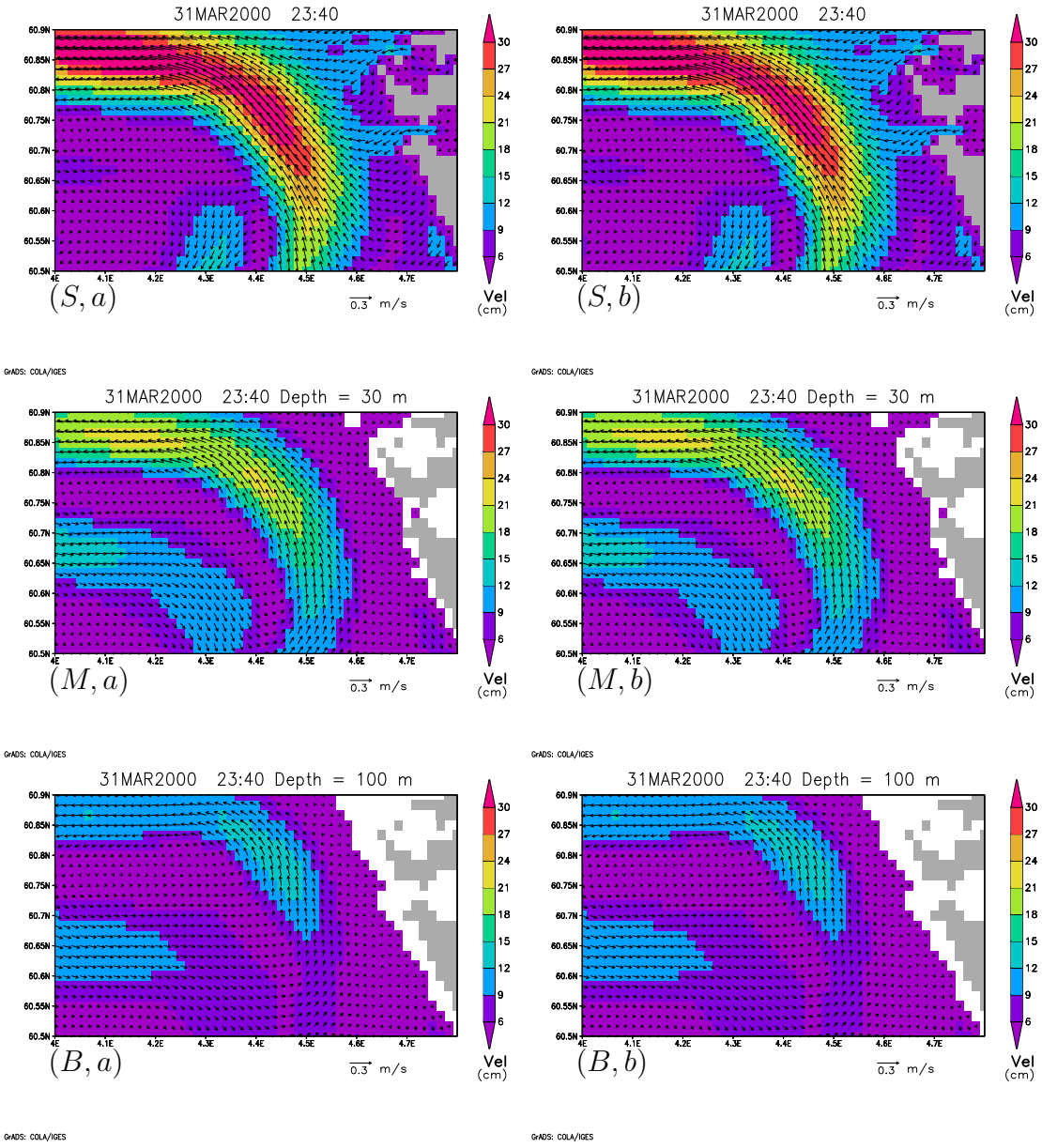

FIGURE 6.35: Velocity fields at surface (upper panels, marked by S), central layer (marked by M), and bottom layer (marked by B) for the standard assimilation run (a-panel) and the real $3D$ run (b-panel), respectively.

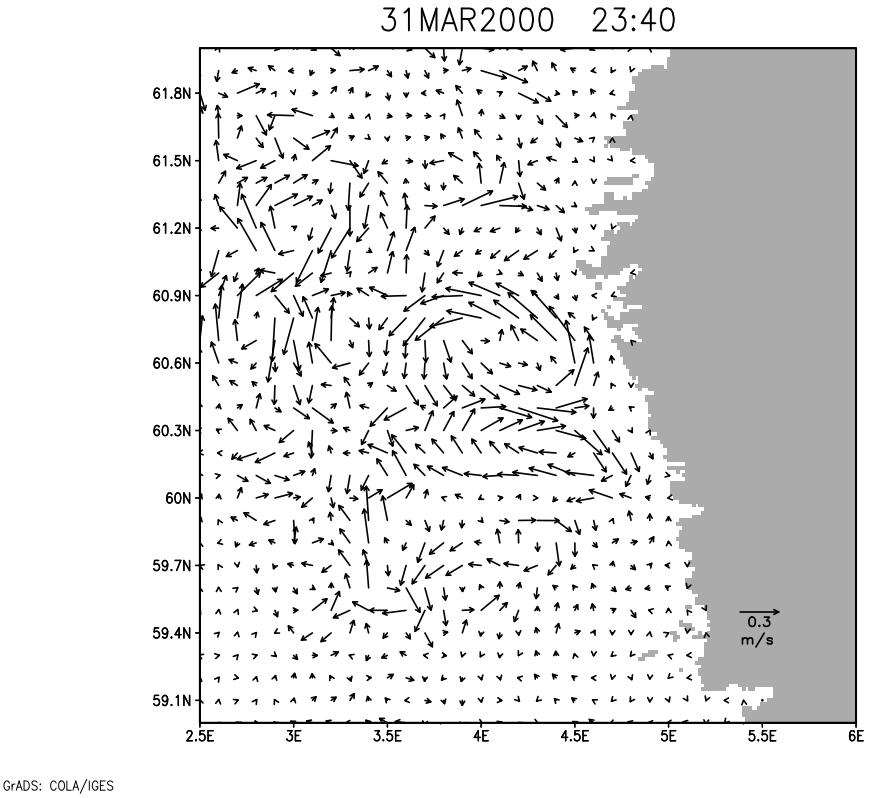

(a) Surface Layer

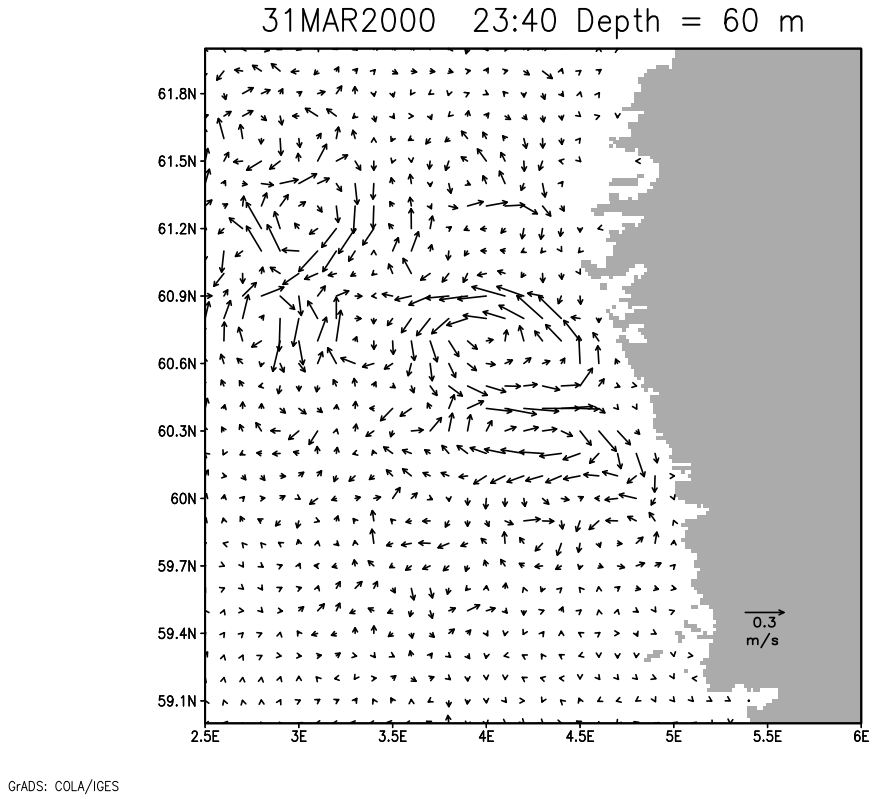

(b) Middle Layer

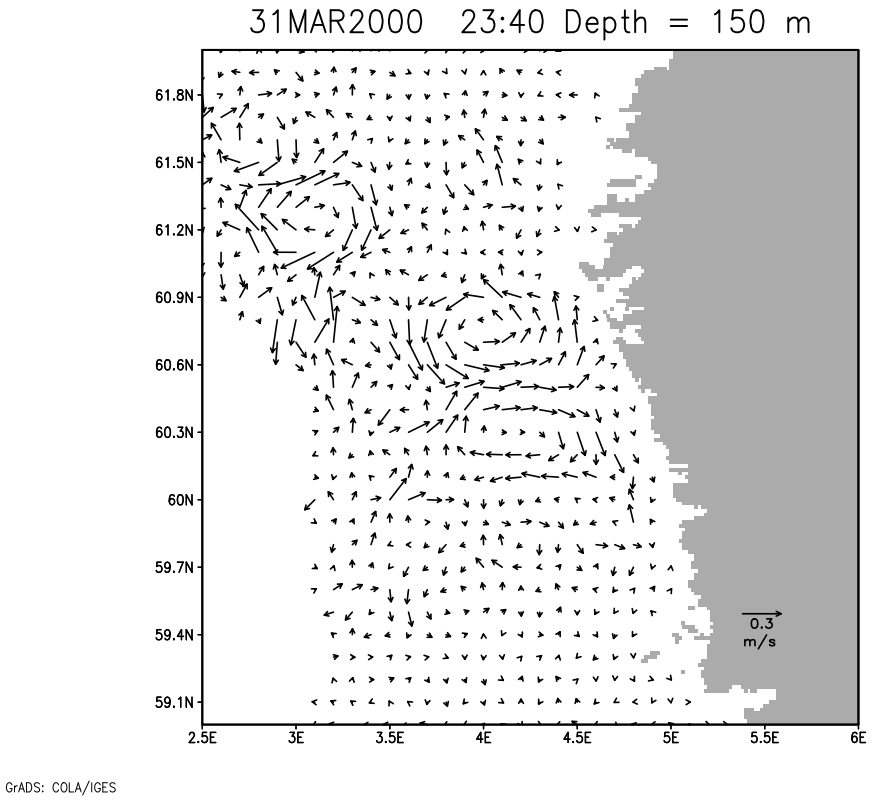

(c) Bottom Layer

FIGURE 6.36: Velocity differences at surface (a), central layer (b), and bottom layer (c) of the standard assimilation run at 23 : 40 UTC on March 31, 2000.

Chapter 7

Discussion and Conclusion

In the present study, a high-frequency real-time assimilation method named QEnKF has been developed based on a tide-resolving coastal baroclinic model. In one word, the QEnKF is a hybrid of the EnKF system and the CQC method. The benefit of our method is, on the one hand, that it inherits the advantages of the traditional Ensemble Kalman filter, like the usage of model states to describe the model errors, which makes the method easy to be implemented. On the other hand, it overcomes the limitation caused by the employment of a large number of ensemble members required in the traditional EnKF method. Since in the QEnKF method, we assume that forecast errors can be resembled forecast tendencies. Only this makes the high-frequency assimilation feasible.

In order to evaluate the performance and sensitivity to assimilation parameters of the QEnKF method, a perfect, linear forecast model is used. The testes with the linear model show an inspiring phenomena, i.e., our newly developed QEnKF method gives better results than the traditional EnKF method. Besides, a large ensemble size is not a burden any more.

Before assimilation, from the comparisons of the reference run with the HF radar data, we find that our model simulation results do not agree very well with the radar observations. This big difference between both of them makes the assimilation more challenging, since it will introduce imbalance to the model. But on the other hand, we expect that the radar data contain more small-scale structures

than model simulations which can be incorporated into the latter by an assimilation method.

To give a general impression of the our assimilation method compared to the traditional EnKF, two experiments with both methods are presented. The results indicate that our method is much superior to the traditional method. One of the reasons is that most of the model errors are systematic, and hence can not be well represented by random noise, as normally is expected in the EnKF method. Another reason is that a divergence will happen when the traditional EnKF method is implemented in a high-frequency forecasting system, since the ensemble is inherited from the estimation of background errors at the beginning. In other words, the state-vector space described by such ensemble is determined at the very beginning. However, the EnKF method seeks an analysis to minimize the posterior variance. Besides, a high-frequency assimilation results in the fact that there remains only a short time interval to propogate a certain model error. Hence, after a long time assimilation, the posterior variance keeps decreasing, a divergence will happen that means the analysis will ignore the observations. In contrast, in the QEnKF system, the forecast tendencies are flow-dependent and determined at times when HF data are available and used for assimilation. The latter can be expected to give more realistic results, since as explained, the way to describe the model forecast errors is more sophisticated.

The comparisons of three assimilation runs with different observation densities indicate that, first of all, our QEnKF assimilation method is correct, since with the observation number decreases, the effect of assimilation decreases too, that can be easily deduced from the changes of the spatial RMS errors. Secondly, when the observations get sparse, the correlation between them becomes lower, and the update of the analysis decreases. Additionally, the changes are more obvious in the u-direction than in the v-direction. Moreover, due to the weak correlation between temperature and velocity and the fact that the radar data only concentrates in relatively small area, the update of temperature is not affected too strongly by the variation of observation density. Besides, the corrections of temperature in the northern part of the model domain are larger than in the southern part, since the main current in this area is directed northward.

As known, one popular way to avoiding filter divergence in the traditional EnKF is by magnifying the forecast error covariance. The test of this method indicates that it does help to avoid filter divergence, but this ability is quite weak, since the patterns of the prior error covariances do not change. Hence, the update of temperature and velocity field using this method changes quite slowly. However, in our QEnKF method, the forecast tendencies are used to represent the forecast errors, which will change with the variantion of the model time step. Thus, the newly developed method (QEnKF) is sensible to the model time step. However, once the model configuration and validation is finished, the appropriate model time step can be diterminted very easily. Besides, the sensitivity tests with this parameter are much easier to perform compared to the choice of the ensemble size in the traditional EnKF method. Nevertheless, the experiment of magnification of the forecast error inspire us that when the model time step is fixed, one way to enlarge the state sapce is to magnify the magnitude of the forecast error.

The rank problem is another kind of obstacle in the practical implementation of the traditional EnKF method, hence, plenty of studies have been performed to solve it. One way is to assimilate each individual observation sequentially, which is a popular method to reduce the rank of the gain matrix. However, our observational data are not sparsely distributed and independent to each other, but concentrate in a small area and have relatively high correlation with each other. Thus, an appropriate way to reduce the rank of gain matrix is not to assimilate observation data one by one, but to separate them into two batches, i.e., the u-component and v-component, as well as using the significant eigenvalues through an eigenvalue decomposition. By assimilating the u- and v- variables sequentially, the assimilation results are better than the twin assimilation without such an operation. As expected the benefit of this method is more obvious in the update of velocity fields than of temperature fields. That means the corrections of the latter are not sensitive to variations of the velocity field.

In the traditional EnKF method, enough ensemble members are the prerequisite to get an optimal result. That is also the reason that high-frequency assimilation with the traditional EnKF is not feasible. However, in our newly developed QEnKF method, the ensemble size is no longer the main factor to decide the forecast error covariance, thus its importance is largely reduced. Another test with

doubling the current ensemble size shows no improvement. On the contrary, since the forecast errors are represented by the forecast tendencies, when the ensemble size increases, more historical information of background errors is included, that makes the real-time assimilation a little bit worse.

Finally, the realistic three-dimensional assimilation with the QEnKF method is performed, which means the state vectors are composed not only of the surface variables, but also of the interior variables. But the results of this assimilation run are almost the same as of the run only analyzing surface variables. Nevertheless, all the experiments with the QEnKF method demonstrate that our real-time assimilation method is suitable for a coastal ocean model, and can introduce the information of HF radar currents data to a circulation model, not only improving the velocity fields but also the temperature and salinity distributions.

Appendix A

Square Root Analysis Schemes for EnKF

This square root analysis schemes for the traditional Ensemble Kalman filter is provided by Evensen (2004), the purpose of it is to reduce the sampling errors and improve the quality of the analysis by means of a usage of a low-rank representation of the measurement error covariance matrix. The detailed description of the algorithm was given by the author, here, we only give a brief introduction.
According Evensen (2004), a few matrixes are defined, which contain all the variables in the EnKF equations (see Chapter 2), like,

$$A = (\varphi_1, \varphi_2, ..., \varphi_N), \tag{A.1}$$

$$P_e = \frac{A'(A')^T}{N-1}, \tag{A.2}$$

$$D = (d_1, d_2, ..., d_N). \tag{A.3}$$

Where A, P_e and D represent the ensemble memebers of the model states, the ensemble covariances and the ensemble members of the observations. N is the number of ensemble members. After the definition, the analysis equation can be rewritten as,

$$A^a = A + A'A'^T H^T (HA'A'^T H^T + EE^T)^{-1}(D - HA). \tag{A.4}$$

By defining the innovation vectors as

$$D' = D - HA, \tag{A.5}$$

the analysis finally can be expressed as

$$A^a = A + A'A'^T H^T (HA'A'^T H^T + EE^T)^{-1} D'. \tag{A.6}$$

By introducing a new matrix $S = HA'$, the matrix C can be defined as

$$\begin{aligned} C &= SS^T + (N-1)R & \text{(A.7)} \\ &= SS^T + EE^T. & \text{(A.8)} \end{aligned}$$

The main idea of this square root algorithm is to treat A^a as a sum of two parts, one is the mean $\overline{\varphi^a}$, the other is the perturbations $A^{a\prime}$. The mean of the analyzed ensemble is easy to obtain in terms of averaging the analysis euqation as follows:

$$\overline{\varphi^a} = \overline{\varphi^f} + A'S^T C^{-1}(d - H\overline{\varphi^f}). \tag{A.9}$$

The perturbations are calculated from the analyzed error covariance matrix equation, since

$$P^a = P^f - P^f H^T (HP^f H^T + R)^{-1} HP^f, \tag{A.10}$$

which is as the same as

$$A^{a\prime}A^{a\prime T} = A'(I - S^T C^{-1} S)A'^T. \tag{A.11}$$

With the assumption that C^{-1} exists, the eigenvalue decomposition of C is $Z\Lambda Z^T$, and then

$$C^{-1} = Z\Lambda^{-1} Z^T. \tag{A.12}$$

The equation A.11 can be rewritten as follows:

$$\begin{aligned} A^{a\prime}A^{a\prime T} &= A'(I - S^T Z\Lambda^{-1} Z^T S)A'^T & \text{(A.13)} \\ &= A'[I - (\Lambda^{-\frac{1}{2}} Z^T S)^T (\Lambda^{-\frac{1}{2}} Z^T S)]A'^T. & \text{(A.14)} \end{aligned}$$

By computing the singular value decomposition of $(\Lambda^{-\frac{1}{2}} Z^T S)$, this equation is

$$\begin{aligned} A^{a\prime}A^{a\prime T} &= A'(I - [U\Sigma V^T]^T [U\Sigma V^T])A'^T & \text{(A.15)} \\ &= (A'V\sqrt{I - \Sigma^T\Sigma})(A'V\sqrt{I - \Sigma^T\Sigma})^T, & \text{(A.16)} \end{aligned}$$

where Σ and V are the singular values and singular vectors of $(\Lambda^{-\frac{1}{2}} Z^T S)$. Hence, the equations above show the germ of the name of "square root algorithm".

References

Anderson, J., 2001. An ensemble adjustment Kalman filter for data assimilation. Monthly Weather Review 129 (12), 2884–2903.

Anderson, J., Anderson, S., 1999. A Monte Carlo implementation of the nonlinear filtering problem to produce ensemble assimilations and forecasts. Monthly Weather Review 127 (12), 2741–2758.

Andersson, E., Pailleux, J., Thépaut, J., Eyre, J., McNally, A., Kelly, G., Courtier, P., 1994. Use of cloud-cleared radiances in three/four-dimensional variational data assimilation. Quarterly Journal of the Royal Meteorological Society 120 (517), 627–654.

Backhaus, J., 1985. A three-dimensional model for the simulation of shelf sea dynamics. Ocean Dynamics 38 (4), 165–187.

Backhaus, J., Bartsch, J., Damm, P., Pohlmann, T., Schrum, C., 1991. The marine weather bulletin North Sea. Lnt Counc Explor Sea CM.

Backhaus, J., Hainbucher, D., 1987. A finite difference general circulation model for shelf seas and its application to low frequency variability on the North European Shelf. Elsevier oceanography series 45, 221–244.

Barrick, D., 1978. HF radio oceanography:A review. Boundary-Layer Meteorology 13 (1), 23–43.

Barrick, D., Evans, M., Weber, B., 1977. Ocean Surface Currents Mapped by Radar. Science 198 (4313), 138–144.

Barth, A., Alvera-Azcarate, A., Weisberg, R., Petersen, O., Hearn, C., Hearn, C., Petersen, O., Zhang, Z., Beletsky, D., Schwab, D., et al., 2007. Assimilation of High-Frequency Radar Currents in a Nested Model of the West Florida Shelf. In: American Geophysical Union, Fall Meeting 2007, abstract OS52A-02.

Becker, G., Giese, H., Isert, K., Köonig, P., Langenberg, H., Pohlmann, T., Schrum, C., 1999. Mesoscale variability in the German Bight. Dtsch Hydrogr 51, 2.

Bertino, L., Evensen, G., Wackernagel, H., 2002. Combining geostatistics and Kalman filtering for data assimilation in an estuarine system. Inverse problems 18, 1–23.

Breivik, Ř., Saetra, Ř., 2001. Real time assimilation of HF radar currents into a coastal ocean model. Journal of Marine Systems 28 (3-4), 161–182.

Burgers, G., Jan van Leeuwen, P., Evensen, G., 1998. Analysis scheme in the ensemble Kalman filter. Monthly Weather Review 126 (6), 1719–1724.

Carbajal, N., 1993. Modelling of the circulation in the Gulf of California. Inst. für Meereskunde.

Courtier, P., Thepaut, J., Hollingsworth, A., 1994. A strategy for operational implementation of 4D-Var, using an incremental approach. Quarterly Journal of the Royal Meteorological Society 120 (519), 1367–1388.

Cressman, G., 1959. An operational objective analysis system. Monthly Weather Review 87 (10), 367–374.

Daley, R., 1993. Atmospheric data analysis. Cambridge Univ Pr.

Dee, D., 2005. Bias and data assimilation. Quarterly Journal of the Royal Meteorological Society 131 (613), 3323–3344.

D.R.Jackson, M.Keil, B., 2008. Use of Canadian Quick covariances in the Met Office data assimilation system. Q.J.R.Meteorol 134, 1567–1582.

Eide, L., 1979. Evidence of a topographically trapped vortex on the Norwegian continental shelf. Deep Sea Research Part I: Oceanographic Research 26, 601–621.

Eliassen, A., 1954. Provisional report on calculation of spatial covariance and autocorrelation of the pressure field. Inst. Weather and Clim. Res., Acad. Sci., Oslo, Tech. Rep 5.

Evensen, G., 1992. Using the extended Kalman filter with a multilayer quasi-geostrophic ocean model. Journal of Geophysical Research 97 (C11), 17905–17924.

Evensen, G., 1994. Sequential data assimilation with a nonlinear quasi-geostrophic model using Monte Carlo methods to forecast error statistics. JOURNAL OF GEOPHYSICAL RESEARCH-ALL SERIES- 99, 10–10.

Evensen, G., 1997a. Advanced data assimilation for strongly nonlinear dynamics. Monthly Weather Review 125 (6), 1342–1354.

Evensen, G., 1997b. Application of ensemble integrations for predictability studies and data assimilation. In: Monte Carlo Simulations in Oceanography Proceedings Aha Hulikoa Hawaiian Winter Workshop, University of Hawaii at Manoa. pp. 14–17.

Evensen, G., 2003. The Ensemble Kalman Filter: theoretical formulation and practical implementation. Ocean Dynamics 53 (4), 343–367.

Evensen, G., 2004. Sampling strategies and square root analysis schemes for the EnKF. Ocean Dynamics 54 (6), 539–560.

Evensen, G., van Leeuwen, P., 1995. Assimilation of Geosat altimeter data for the Agulhas current using the ensemble Kalman filter with a quasi-geostrophic model. To appear in Monthly Weather Review.

Fisher, M., Courtier, P., 1995. Estimating the covariance matrices of analysis and forecast error in variational data assimilation. ECMWF Research Department Tech. Memo 220, 28.

Fox, D., Teague, W., Barron, C., Carnes, M., Lee, C., 2002. The modular ocean data assimilation system (MODAS). Journal of Atmospheric and Oceanic Technology 19 (2), 240–252.

Gandin, L., Hardin, R., 1965. Objective analysis of meteorological fields. Israel Program for Scientific Translations.

Gurgel, K., Antonischki, G., 1997. Measurement of surface current fields with high spatial resolutionby the HF radar WERA. Geoscience and Remote Sensing, 1997. IGARSS'97.'Remote Sensing-A Scientific Vision for Sustainable Development'., 1997 IEEE International 4.

Gurgel, K., Antonischki, G., Essen, H., Schlick, T., 1999. Wellen Radar (WERA): a new ground-wave HF radar for ocean remote sensing. Coastal Engineering 37 (3-4), 219–234.

Hainbucher, D., Backhaus, J., 1999. Circulation of the eastern north Atlantic and north-west European continental shelf-a hydrodynamic modelling study. Fisheries Oceanography 8 (s 1), 1–12.

Hamill, T., Snyder, C., 2000. A hybrid ensemble Kalman filter–3D variational analysis scheme. Monthly Weather Review 128 (8), 2905–2919.

Hamill, T., Whitaker, J., Snyder, C., 2001. Distance-dependent filtering of background error covariance estimates in an ensemble Kalman filter. Monthly Weather Review 129 (11), 2776–2790.

Hansen, J., Smith, L., 2001. Probabilistic noise reduction. Tellus A 53 (5), 585–598.

Harms, I., 1992. A numerical study of the barotropic circulation in the Barents and Kara Seas. Continental Shelf Research 12, 1043–1058.

Haugan, P., Evensen, G., Johannessen, J., Johannessen, O., Pettersson, L., 1991. Modeled and observed mesoscale circulation and wave-current refraction during the 1988 Norwegian Continental Shelf Experiment. Journal of Geophysical Research-Oceans 96 (C6).

Heemink, A., Verlaan, M., Segers, A., 2001. Variance reduced ensemble Kalman filtering. Monthly Weather Review 129 (7), 1718–1728.

Helland-Hansen, B., Nansen, F., 1909. The Norwegian Sea. FiskDir. Skr. Ser. HavUnders 2, 1–360.

Houtekamer, P., Mitchell, H., 1998. Data assimilation using an ensemble Kalman filter technique. Monthly Weather Review 126 (3), 796–811.

Houtekamer, P., Mitchell, H., 2001. A sequential ensemble Kalman filter for atmospheric data assimilation. Monthly Weather Review 129 (1), 123–137.

Ikeda, M., Johannessen, J., Lygre, K., Sandven, S., 1989. A process study of mesoscale meanders and eddies in the Norwegian Coastal Current. Journal of Physical Oceanography 19 (1), 20–35.

James, I., 1987. A general three-dimensional eddy-resolving model for stratified seas. Elsevier oceanography series 45, 591–608.

Johannessen, J., Sandven, S., Lygre, K., Svendsen, E., Johannessen, O., 1989. Three-dimensional structure of mesoscale eddies in the Norwegian Coastal Current. Journal of Physical Oceanography 19 (1), 3–19.

Kalman, R., 1960. A new approach to linear filtering and prediction problems. Journal of basic Engineering 82 (1), 35–45.

Kalman, R., Bucy, R., 1961. New results in linear filtering and prediction. Journal of Basic Engineering (ASME), 83D 95108.

Kalnay, E., 2003. Atmospheric modeling, data assimilation, and predictability. Cambridge Univ Pr.

Kalnay, E., Kanamitsu, M., Kistler, R., Collins, W., Deaven, D., Gandin, L., Iredell, M., Saha, S., White, G., Woollen, J., et al., 1996. The NCEP/NCAR 40-Year Reanalysis Project. Bulletin of the American Meteorological Society 77 (3), 437–471.

Kara, A., Barron, C., 2007. Fine-resolution satellite-based daily sea surface temperatures over the global ocean. Journal of Geophysical Research 112 (C5).

Kauker, F., Langenberg, H., 2000. Two models for the climate change related development of sea levels in the North Sea-a comparison. Climate Research 15 (1), 61–67.

Keppenne, C., 2000. Data assimilation into a primitive-equation model with a parallel ensemble Kalman filter. Monthly Weather Review 128 (6), 1971–1981.

Kochergin, V., 1987. Three-dimensional prognostic models. Three-dimensional coastal ocean models, 201–208.

Köhl, A., Stammer, D., 2004. Optimal observations for variational data assimilation. Journal of Physical Oceanography 34 (3), 529–542.

KOHL, A., WILLEBRAND, J., 2002. An adjoint method for the assimilation of statistical characteristics into eddy-resolving ocean models. Tellus A 54 (4), 406–425.

Kurapov, A., Egbert, G., Miller, R., Allen, J., 2002. Data Assimilation in a Baroclinic Coastal Ocean Model: Ensemble Statistics and Comparison of Methods. Monthly Weather Review 130 (4), 1009–1025.

Lax, P., Wendroff, B., 1960. Systems of conservation laws. Comm. Pure Appl. Math 13 (2), 217–237.

Leith, C., 1974. Theoretical skill of Monte Carlo forecasts. Monthly Weather Review 102 (6), 409–418.

Lermusiaux, P., 1999. Data Assimilation via Error Subspace Statistical Estimation. Monthly Weather Review 127 (7), 1408–1432.

Levitus, S., Boyer, T., Antonov, J., 1994. World Ocean Atlas 1994. Volume 5. Interannual variability of upper ocean thermal structure. Tech. rep., PB–95-270120/XAB, National Environmental Satellite, Data, and Information Service, Washington, DC (United States).

Lewis, J., Shulman, I., Blumberg, A., 1998. Assimilation of CODAR observations into ocean models. Continental Shelf Research 18, 541–559.

Lorenc, A., 1981. A global three-dimensional multivariate statistical interpolation scheme. Monthly Weather Review 109 (4), 701–721.

Lorenc, A., 1986. Analysis methods for numerical weather prediction. Quart. J. Roy. Meteor. Soc 112 (11), 77–1194.

Miller, R., Carter, E., Blue, S., 1999. Data assimilation into nonlinear stochastic models. Tellus A 51 (2), 167–194.

Miller, R., Ghil, M., Gauthiez, F., 1994. Advanced data assimilation in strongly nonlinear dynamical systems. Journal of the Atmospheric Sciences 51 (8), 1037–1056.

Mitchell, H., Houtekamer, P., 2000. An adaptive ensemble Kalman filter. Monthly Weather Review 128 (2), 416–433.

Mitchell, H., Houtekamer, P., Pellerin, G., 2002. Ensemble size, balance, and model-error representation in an ensemble Kalman filter. Monthly weather review 130 (11), 2791–2808.

Molteni, F., Buizza, R., Palmer, T., Petroliagis, T., 1996. The ECMWF ensemble prediction system: Methodology and validation. Quarterly Journal of the Royal Meteorological Society 122 (529), 73–120.

Mork, M., 1981. Circulation phenomena and frontal dynamics of the Norwegian coastal current. Philosophical Transactions of the Royal Society of London. Series A, Mathematical and Physical Sciences 302 (1472), 635–647.

Mysak, L., Schott, F., 1977. Evidence for baroclinic instability of the Norwegian Current. Journal of Geophysical Research 82, 2087–2095.

Oey, L., Chen, P., 1992a. A model simulation of circulation in the northeast Atlantic shelves and seas. Journal of Geophysical Research-Oceans 97 (C12).

Oey, L., Chen, P., 1992b. A nested-grid ocean model: with application to the simulation of meanders and eddies in the Norwegian Coastal Current. Journal of Geophysical Research-Oceans 97 (C12).

Oke, P., Allen, J., Miller, R., Egbert, G., Kosro, P., 2002. Assimilation of surface velocity data into a primitive equation coastal ocean model. J. Geophys. Res 107, 3122.

Paduan, J., Shulman, I., 2004. HF radar data assimilation in the Monterey Bay area. J. Geophys. Res 109.

Panofsky, R., 1949. Objective weather-map analysis. Journal of the Atmospheric Sciences 6 (6), 386–392.

Parrish, D., Derber, J., 1992. The National Meteorological Center's spectral statistical-interpolation analysis system. Monthly Weather Review 120 (8), 1747–1763.

Paulsen, V., Power, S., Smith, R., 1989. Schur products and matrix completions. Journal of Functional Analysis 85 (1), 151–178.

Pohlmann, T., 1991. Evaluations of hydro-and thermodynamic processes in the North Sea with a 3-dimensional numerical model. Berichte aus dem Zentrum fuer Meeres-und Klimaforschung 23, 1–116.

Pohlmann, T., 1996a. Calculating the development of the thermal vertical stratification in the North Sea with a three-dimensional baroclinic circulation model. Continental Shelf Research 16 (2), 163–194.

Pohlmann, T., 1996b. Predicting the thermocline in a circulation model of the North seapart I: model description, calibration and verification. Continental Shelf Research 16 (2), 131–146.

Pohlmann, T., 2006. A meso-scale model of the central and southern North Sea: Consequences of an improved resolution. Continental Shelf Research 26 (19), 2367–2385.

Polavarapu, S., Ren, S., Rochon, Y., Sankey, D., Ek, N., Koshyk, J., Tarasick, D., 2005. Data assimilation with the Canadian middle atmosphere model. Atmosphere-Ocean 43 (1), 77–100.

Saetre, R., Mork, M., 1971. The Norwegian coastal current. In: Proceedings of the first international conference on port and ocean engineering under Arctic conditions. Vol. 2.

Schlatter, T., 1975. Some experiments with a multivariate statistical objective analysis scheme. Monthly Weather Review 103 (3), 246–257.

Schröter, J., Seiler, U., Wenzel, M., 1993. Variational assimilation of GEOSAT data into an eddy-resolving model of the Gulf Stream extension area. Journal of Physical Oceanography 23 (5), 925–953.

Scott, R., Allen, J., Egbert, G., Miller, R., 2000. Assimilation of Surface Current Measurements in a Coastal Ocean Model. Journal of Physical Oceanography 30 (9), 2359–2378.

Smagorinsky, J., 1963. General Circulation Experiments with the Primitive Equations. I. The Basic Experiment. Mon. Weather Rev, 99–164.

Stammer, D., Ueyoshi, K., Köhl, A., Large, W., Josey, S., Wunsch, C., 2004. Estimating air-sea fluxes of heat, freshwater, and momentum through global ocean data assimilation. J. Geophys. Res 109, C05023.

Stammer, D., Wunsch, C., Giering, R., Eckert, C., Heimbach, P., Marotzke, J., Adcroft, A., Hill, C., Marshall, J., 2002. Global ocean circulation during 1992–1997, estimated from ocean observations and a general circulation model. Journal of Geophysical Research-Oceans 107 (C9), 3118.

Talagrand, O., 1997. Assimilation of observations, an introduction. In: Data assimilation in meteorology and oceanography: theory and practice: a collection of papers presented at the WMO Second International Symposium on Assimilation of Observations in Meteorology and Oceanography, 13-17 March 1995, Tokyo, Japan. Meteorological Society of Japan, p. 81.

Talagrand, O., Courtier, P., 1987. Variational assimilation of meteorological observations with the adjoint vorticity equation. I: Theory. Quarterly Journal of the Royal Meteorological Society 113 (478).

Thépaut, J., Hoffman, R., Courtier, P., 1993. Interactions of dynamics and observations in a four-dimensional variational assimilation. Monthly Weather Review 121 (12), 3393–3414.

Thompson, P., 1969. Reduction of analysis error through constraints of dynamical consistency. Journal of Applied Meteorology 8 (5), 738–742.

Toth, Z., Kalnay, E., 1993. Ensemble forecasting at NMC: The generation of perturbations. Bulletin of the American Meteorological Society 74 (12), 2317–2330.

Toth, Z., Kalnay, E., 1997. Ensemble forecasting at NCEP and the breeding method. Monthly Weather Review 125 (12), 3297–3319.

van Leeuwen, P., 1999. Comment on "Data assimilation using an ensemble Kalman filter technique". Monthly Weather Review 127 (6), 1374–1377.

Vinger, A., McClimans, T., Tryggestad, S., 1981. Laboratory observations of instabilities in a straight coastal current. The Norwegian Coastal Current 2, 553–582.

Welch, G., Bishop, G., 1995. An introduction to the Kalman filter. University of North Carolina at Chapel Hill, Chapel Hill, NC.